




University of
Stavanger

Faculty of Science and Technology

MASTER'S THESIS

Study program/Specialization: Master thesis Mechanical and Structural Engineering and Material Science (Mechanical Systems)	Spring semester, 2021 Open
Author: Ghulam Dastgir	 (Signature of Author)
Programme coordinator: Knut Erik Teigen Giljarhus Supervisor(s): Knut Erik Teigen Giljarhus	
Thesis title: Computational fluid dynamics simulation of flying discs	
Credits (ECTS): 30	
Key words: CFD, Angle of attack, OpenFoam, Aerodynamics, Drag Force, Disc flight, Lift force.	Pages: 82+11=93 Stavanger, 15 th of June 2021



**Faculty of Science and Technology
Department of Mechanical and Structural Engineering and Materials
Science**

**Specialization
Mechanical Systems**

Computational fluid dynamics simulation of flying discs

Ghulam Dastgir

Supervisor

Associate professor Knut Erik Giljarhus, University of Stavanger

This page intentionally left blank

PREFACE

The research work covered in this study is carried out as a part of the Master's thesis work. The idea to understand and improve the flight dynamics of the flying disc design stemmed from my motivation to study and observe the aerodynamic behavior of the flying discs because of their applications in many major industrial and engineering sectors.

The work presented here comprises not only theoretical but also, practical aspects which increase its scope towards a better understanding of the specified model which will help future researchers in this field.

In reality, my success in this work is dedicated to my strong support group because without their unwavering support I would not have been able to achieve this. First of all, I would like to pay my respects to my Supervisor Knut Erik Teigen Giljarhus whose guidance, support, valuable tips, suggestions, patience, and valued time has not only encouraged me but also, made me able to complete this thesis. Secondly, I am grateful to my University (University of Stavanger) for providing the strong academic knowledge, state-of-the-art research facilities, and innovative environment to complete my research work. The research and work-oriented environment enabled me to not only fulfill my master's degree requirements but also, prepared me well to expose myself to the coming challenges ahead in my career.

Additionally, I would like to thank my parents for always believing in me, supporting me, and standing beside me at all times. Lastly, I would like to extend my heartiest regards to my brother Shabbir Adil and Muhammad Naseer whose motivation and hard-working nature have always been an inspiration for me and empowered me to face the challenges that came my way.

ABSTRACT

This manuscript is divided in two parts. First, a comprehensive review of flight dynamics and disc-wing aerodynamics literature is presented. It discusses the aerodynamic characteristics of circular planform wings and the flight dynamic characteristics. Second, a numerical study is conducted in order to study the flow fields around the wing discs and to validate the effectiveness of the computational fluid dynamics (CFD) techniques on the multiple disc designs. The characteristics which were under consideration are the aerodynamic forces (mainly lift and drag forces), pressure & velocity distribution on the surface of the disc and in the surrounding field, moment coefficients, and the flow field variations. The numerical results were compared with the experimental results to verify the accuracy and the validity of the simulations. This comparison showed clear similarity of numerical estimations with the experimental data proving the capacity of the model to simulate disc aerodynamics with accuracy. The computational analysis was carried out also on three types of discs including Putter, Midrange, and Aviar discs models. The results were compared to experimental work as before showing also a good accuracy between numerical and experimental data.

Different turbulence models (RANS, LES and DDES) were tested and compared. The outcomes obtained from the comparison of RANS and LES models of turbulence show both turbulence models may present different flow topologies. By its characteristics RANS model may generate steadier flow than the LES model but the latest demands higher computational effort. Furthermore, a comparison of RANS and DDES turbulence models was also made to observe the behavior of the aerodynamic coefficients. The results obtained showed some deviation from the experimental data. However, despite these differences model has shown to well compute aerodynamics of the disc over different geometries. Finally, the standard RANS KOmegaSST model may present good accuracy comparing to experimental data but the study of the flow structures over the surface of the discs might be examined and improved with DDES KOmegaSSTDDES model instead.

Contents

List of Figures :	VIII
List of Tables :	VIII
NOMENCLATURE:	X
1. Introduction:	1
2. Literature review:	2
2.1 Aerodynamics of Different Geometries:	2
2.1.1 Balls:	2
2.1.2 Discs	4
2.1.3 Javelin:	5
2.1.4 Shot Put	6
2.2 Aerodynamics of Circular Planform Wings:	6
2.2.1 Frisbee:	6
2.2.1.1 Aerodynamic Forces:	10
2.2.1.2 Stability of Flying Frisbee:	11
2.2.2 Discs:	12
2.2.3 Coin-like Cylinders:	13
2.2.4 Analysis on Span Effectiveness factor:	13
2.3 Flight Dynamics of Spin-stabilized Disc-wings:	15
2.3.1 Frisbee:	15
2.3.2 Discs:	20
3. Theoretical background:	22
3.1 Numerical analysis of Disc-wings:	21
3.1.1 Aerodynamic coefficients:	24
3.1.2 Aerodynamic Parameters of Low Aspect Ratio Wings:	25
3.1.3 Trim & Stability of Tailless Flight Vehicles:	27
3.1.4 Flight Dynamics of a Spin-stabilized Disc-wing:	31
3.1.5 Non-dimensional Roll Time:	33
4. Computational Fluid Dynamics (CFD):	34
4.1 Computational Setup:	34
4.1.1 Geometry Cleaning:	35
4.1.2 Meshing:	35

4.1.3	Solution Setup:	36
4.1.4	Boundary Conditions:	36
4.1.5	RANS model:	36
4.1.6	LES model:	37
4.1.7	DDES model:	39
4.2	Modeling Approaches:	41
4.2.1	DDES and RANS:	41
4.2.2	LES:	44
5.	Numerical Results:	76
5.1	Mesh Sensitivity:	47
5.2	Model Validation:	49
5.3	Flow Topology:	51
5.4	RANS/LES Comparison:.....	55
5.5	Other Disc Geometries:	58
5.5.1	Putter Disc:	59
5.5.2	Midrange Disc:.....	65
5.5.3	Comparison of putter, midrange and driver discs:.....	71
5.5.4	RANS/DDES Comparison:	59
6.	Conclusion	76
7.	References	77

List of Figures :

Figure 1: Air Flow around a ball during the flight, (Nagami, Tomoyuki & Higuchi, Takatoshi & Kanosue, Kazuyuki, 2013).....	3
Figure 2: Aerodynamic forces and angles during the disc flight (Andreas V. Maheras, 2016)..	4
Figure 3: The Javelin In Flight (javelin World)	5
Figure 4: Aerodynamic Forces on Javelin (javelin World)	6
Figure 5: Aerodynamic Forces on the Frisbee (UPREPANDYPHAM15, 2015)	11
Figure 6: Torque generated due to center of pressure and center of mass (V. R. Morrison, 2005).....	12
Figure 7. Comparison of aerodynamic load data for circular planform wings, derived from various sources found in the literature, with chordwise cross-sections as seen to the right of the figure (Potts et Crowther 2002).....	14
Figure 8:Boundary conditions for aerodynamic calculations (JS Carlton, 2007)	23
Figure 9. Definition of reference locations for longitudinal forces and moments acting as a tailless flight vehicle (Potts et Crowther 2002).....	28
Figure 10. Illustration of longitudinal stability and trim characteristics of a tailless flight vehicle for permutations of camber and static margin (Potts et Crowther 2002).....	30
Figure 11. (a) Flight dynamics of the proposed Disc-wing. (b) Body fixed axis schematic diagram. The nose would be in positive x-direction in a conventional aircraft (Potts et Crowther 2002).	32
Figure 12: Aviar Disc Front View	36
Figure 13: ROC Disc Front View	36
Figure 14: Wraith Disc Front View	36
Figure 15: Schematic representation of the numerical domain – Boundary conditions.....	37
Figure 16: Geometry meshes resulting from the different mesh densities.....	46
Figure 17: Velocity contour for the different mesh densities.....	47
Figure 18: Disc Geometry – Wraith	48
Figure 19. Experimental validation – Numerical vs Experimental values.....	49
Figure 20. Velocity contour for different AoA.....	50
Figure 21. Velocity streamline plots for different AoA.	52

Figure 22. Streamlines – Counter-rotating vortex.	53
Figure 23. Vorticity - Counter-rotating vortex.	54
Figure 24. RANS and LES comparison.....	55
Figure 25. Velocity contour - RANS and LES comparison.....	56
Figure 26: Different disc geometries.....	57
Figure 27. Disc geometry – Aviar.....	58
Figure 28. Experimental validation – Numerical vs Experimental values.....	58
Figure 29. Velocity contour for different AoA.....	59
Figure 30. Velocity streamline plots for different AoA.	61
Figure 31. Streamlines – Counter-rotating vortex.	62
Figure 32. Vorticity - Counter-rotating vortex.	63
Figure 33. Disc geometry – Roc.....	64
Figure 34. Experimental validation – Numerical vs Experimental values.....	64
Figure 35. Velocity contour for different AoA.....	65
Figure 36. Velocity stream-line plots for different AoA.	67
Figure 37. Streamlines – Counter-rotating vortex.	68
Figure 38. Vorticity - Counter-rotating vortex.	69
Figure 39. Experimental validation – Numerical vs Experimental values.....	70
Figure 40: RANS/DDES comparison – Different geometry discs.....	74
Figure 41: Velocity contour - RANS and DDES comparison – AoA = 0°.....	75

List of Tables :

Table 1: Results of y^+ , C_d , C_L and C_M for all mesh densities.	47
--	----

NOMENCLATURE:

Symbol	Description	Unit
A	Disc plan view area ($\pi d^2/4$)	m ²
AIAA	American Institute of Aeronautics and Astronautics	-
AoA	Angle of attack (°)	-
c	Chord length (diameter for a disc)	m
CAD	Computer-Aided Design	-
\bar{c}	Mean chord	m
AdvR	Advance Ratio	-
t _h	Disc Thickness	m
c _y	Length of chord	m
C _d	drag coefficient (drag force / QA)	-
c _f	skin friction	-
CFD	computational fluid dynamics	-
C _l	lift coefficient (lift force / QA)	-
C _p	pressure coefficient (static pressure)	-
d	disc diameter	m
k	turbulent kinetic energy	J/kg = m ² ·s ⁻²
L	length scale	m
LES	large eddy simulation	-
p	pressure	Pa
P	production of turbulent kinetic energy	-
Re	Reynolds number	-
S	Strain rate tensor	-
SGS	sub grid scale	-
T _s	time scale t/d disc thickness to diameter ratio	m
u	velocity	m/s
y	wall normal coordinate	m

y^+	nondimensional wall distance based on cell fluid velocity	m
ϵ	turbulent energy dissipation rate	m^2/s^3
k- ϵ	Turbulence model	-
μ	dynamic viscosity	Pa.s
ν	kinematic viscosity	m^2/s
ρ	fluid density	Kg/m^3
C_{Drag}	Drag Force	N
C_{Lift}	Lift Force	N
ω	specific turbulent dissipation ($\omega \propto \epsilon/k$)	-
$\sigma_k, \sigma_\omega,$ $\sigma_{\omega^2},$	closure coefficients	-
k- ω SST	closure coefficients (Turbulence model)	-
C_{side}	Side Force	N
q_∞	Dynamic Pressure	Pa
V_∞	Free-stream flow speed	m/s
ρ_∞	Air density	Kg/m^3
τ_{ij}^{mol}	Constant for the transport of molecular momentum	-
Δ	Filtered Width	m
C_m	Coefficient of Momentum	-
COP	Center of Pressure	-
COM	Center of Mass	-
AR	Aspect Ratio	-
τ_w	Shear stress at the Wall Boundary	N/m^2
MAC	Mean Aerodynamic Chord	m
\hat{p}	Non-dimensional Disc Roll Rate	-

1. Introduction:

Generally, both throwing accuracy and flight range may define the performance of flying discs. However, the influence of design on flight performance cannot be negligible and the manufacturer needs to make the design as efficient as possible. Geometrical effects of several flying discs on flight performance standpoint of aerodynamic may be great. For example, the drag, lift, and moment coefficients computed experimentally in a wind tunnel for four sets of the simpler parametric disc and three kinds of golf disc (Kamaruddin, Potts, & Crowther, 2018) and then coupled with numerical simulations provided well-known details on a selective path followed by the flying disc (S shaped path). Coefficient of pitching moment and C_L and C_D were found showing that some parameters (pitching moment) can influence the tendency of the disc to yaw and C_L and C_D impacted throwing distance of disc.

Computational fluid dynamics (CFD) being a very effective method provides various techniques to resolve complex engineering problems and has applications in almost every engineering field to great extent. That is the reason this method has also, been employed to study the aerodynamic behavior of the flying discs and observed their stability and behavior on varying loading conditions. As CFD can cover various aspects of the technical problem and can provide an effective solution, it has been adopted to observe complex problems such as the flow behaviors related to the separated bluff bodies. This technique also covers all the major aspects of the problems related to the cylindrical discs such as the discs with the values from 0.01 to 0.1 representing the ratio of their thickness to the chord diameter and further used to observe the characteristics of frisbee by adding a cavity to its analogous side. For a different value of the angle of attack (AOA), experimental values obtained were compared to simulations (Results showed that for greater AoA, CFD curves were very dispersed and divergent). Having greater AoA values is significant concerning the end of flight viewpoint from human throw (Potts & Masters, 2015). CFD researchers have investigated extensively complex bluff body flows which are experiencing high strength vortices and boundary layer separation in close proximity. CFD simulation was utilized effectively coupled with flight trajectory simulations to rectify the flight under discussion (Seo et al., 2012; 2014). Considering the discs with varying geometric features on which many authors in past applied several turbulence models having the low values of AoA ($0^\circ - 15^\circ$) which concluded that $k - \varepsilon$ is the most critical factor for low aspect external flows bluff bodies (Lukes et al., 2014).

In this study, the authenticity of the Computational fluid dynamics (CFD) technique will be evaluated for predicting the trends of flow fields around the discs interacting with these mediums. The computational fluid dynamics analysis is carried out by using the open-source code, OpenFOAM. The validity of the CFD predictions is shown by comparing the CFD results against experimental measures for three different disc geometries. Steady-state Reynolds Average Navier-Stokes (RANS) simulations on highly resolved grids are performed using the $k - \omega$ Shear Stress Transport (SST). Finally, a comparison between different turbulence models (RANS, LES, and DDES) is proposed to analyze their differences.

Therefore, this report covers in Chapter 1 a comprehensive review of flight dynamics and disc-wing aerodynamics literature. It is divided into two parts; the first part discusses the aerodynamic characteristics of circular planform wings and the second on the flight dynamic characteristics. Chapter 2 is focused on the theoretical background of the key aspects of disc wing geometry, aerodynamics, and flight dynamics. The varying trends in the flight dynamics along with their aerodynamic behavior observed through numerical modeling are discussed in chapter 3. It covers the description of specified model tool setup and mesh sensitivity analysis, an experimental validation, a comparison between RANS and LES turbulence models, a comparison between 3 different geometries, and finally a comparison between RANS and DDES turbulence models.

2. Literature review:

This chapter reviews the aeromechanics and flight dynamics literature of saucer wings. The review is split into 2 parts: the primary part is that the mechanical characteristics of the plane wing, and also the second part is the flight dynamic characteristics. The primary half includes mechanics information for spin-stabilized (axisymmetric) and non-spin-stabilized (axisymmetric) disc wings. The second half focuses on the dynamics of the spin-stabilized disk, focusing on the Frisbee and also the discus.

2.1 Aerodynamics of Different Geometries:

Different objects which have been studied before by researchers comprehensively in literature whose geometry is discussed below:

2.1.1 Balls:

This section highlights the importance of baseballs, golf balls, and footballs having the

emphasis on the parameters that have the ability to affect the maximum distances they can cover. The main aspects that can directly influence the total distance covered by the balls are their launch speed and the angle at which they are thrown (launch angle) (Everett & Linthorne, 2006; Hubbard 2000). The effect is direct for launch speed as the range is directly related to the speed. To find the optimized launch angles for extreme range, it was made indispensable for the researchers to investigate the launch angle. This happened due to the uncertainty in human nature to get the same velocity at every desired launch angle (Hubbard, 2007). There is a concept that is prevalent that launch angle does not depend on the launch speed. There are several assessments, however, which suggested the opposite by unraveling this misconception on the dependency of such parameters.

Generally, the ball aerodynamics are complicated as they are reliant on Reynolds number and rate of spinning. Additionally, surface roughness also adds value to this complexity. In another study, the range of the ball is studied in 2006 by Everett and Linthorne. In their study, they observed that the athlete's physical strength and shape have more impact on the range of the ball in contrast to the physical properties of the ball. They also, predicted that the lower dispatch angle (below 45 degrees) is simpler for the athletes but also, could result in a better range. The air flow around a ball is demonstrated in the below figure,

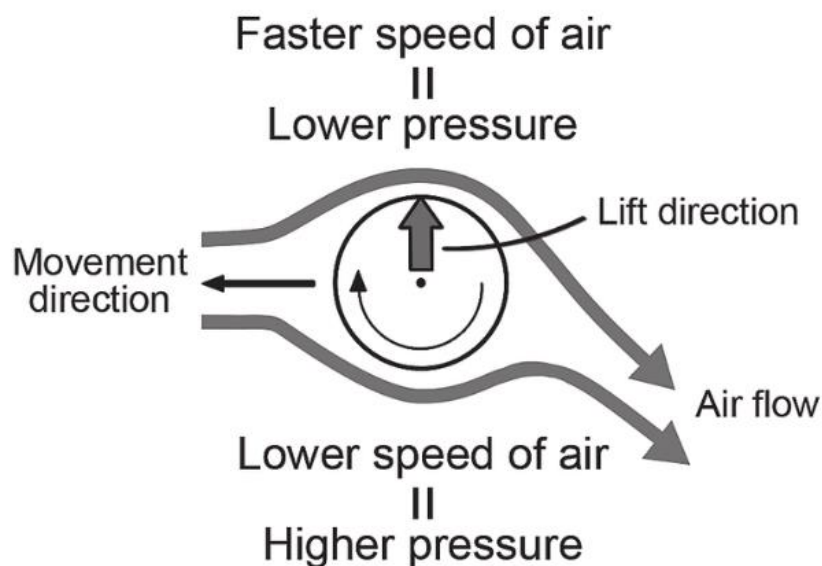


Figure 1: Air Flow around a ball during the flight, (Nagami, Tomoyuki & Higuchi, Takatoshi & Kanosue, Kazuyuki, 2013)

2.1.2 Discs

The disc is perhaps the most established game on the planet that is as yet mainstream today. Throughout the long term, huge endeavors have been made to assess disk the ideal discharge conditions for the greatest reach/range. Multiple studies and extensive surveys were presented on the ideal discharge and range improvement of the discs (Soodak, 2004). The survey conducted by Bartlett in 1992 has shown promising results. His accumulation of almost sixty years of disk writing survey has empowered the enhancement in this field which was applied practically in the later years. Such as a study presented an effectively recreated unique model for ideal plate directions for males and females separately (Hubbard, Cheng; 2007). In this study, they also, presented that the disc range is much sensitive to the way point of the flight instead of roll angle (for the two sexes). In any case, their discoveries didn't consider the reliance on disk discharge speed and twist(spin) because of the absence of exploratory information accessible in literature. This factor might change the disk affectability outcome towards the range. Besides, their work gives considerable comprehension of discus optimization. The aerodynamic forces that act upon the disc are shown in the figure below where CG represents the center of gravity and CP represents the center of pressure.

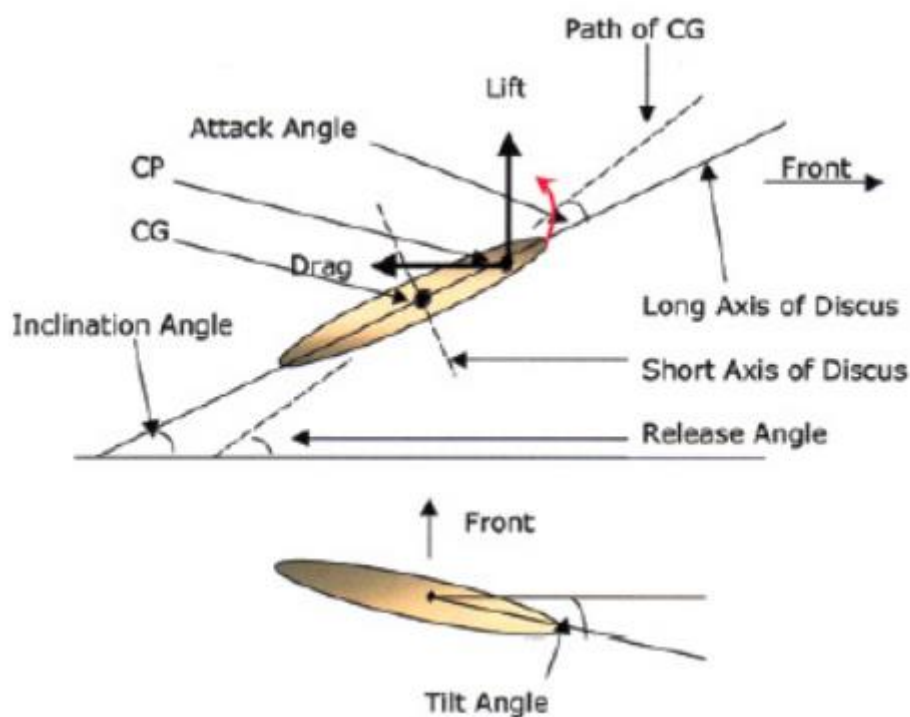


Figure 2: Aerodynamic forces and angles during the disc flight (Andreas V. Maheras, 2016)

2.1.3 Javelin:

Javelin is a field sport that works on the same principle of getting the longest tossing distance in the field. Not at all like disk in which the tossing activity includes a rotational movement, javelin tossing activity includes over-arm toss (Bartlett, 2000). Most exploration did examine the spear and its relationship with the greatest reach is typically centered around the delivery speed and point. A few investigations were completed to reproduce spear trip by utilizing trial information and presented by Hubbard and Alaways in 1989. The outcomes give some significant information boundaries to ideal javelin directions (Hubbard, 1984). As expected, expanding the delivery speed would build the possibility of the spear hurler to accomplish the most extreme tossing distance.

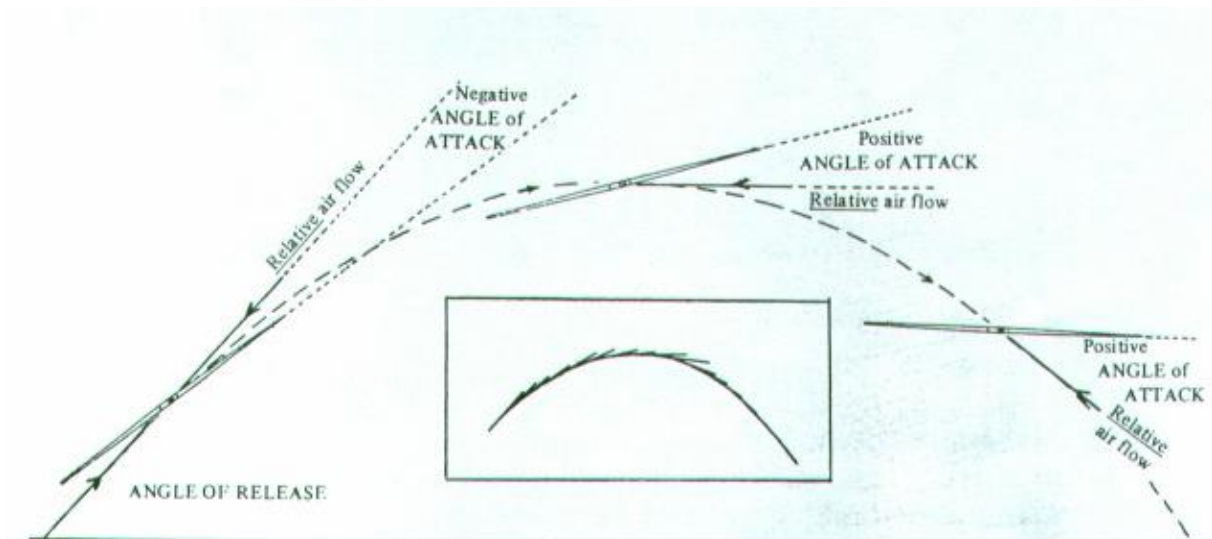


Figure 3: The Javelin In Flight (javelin World)

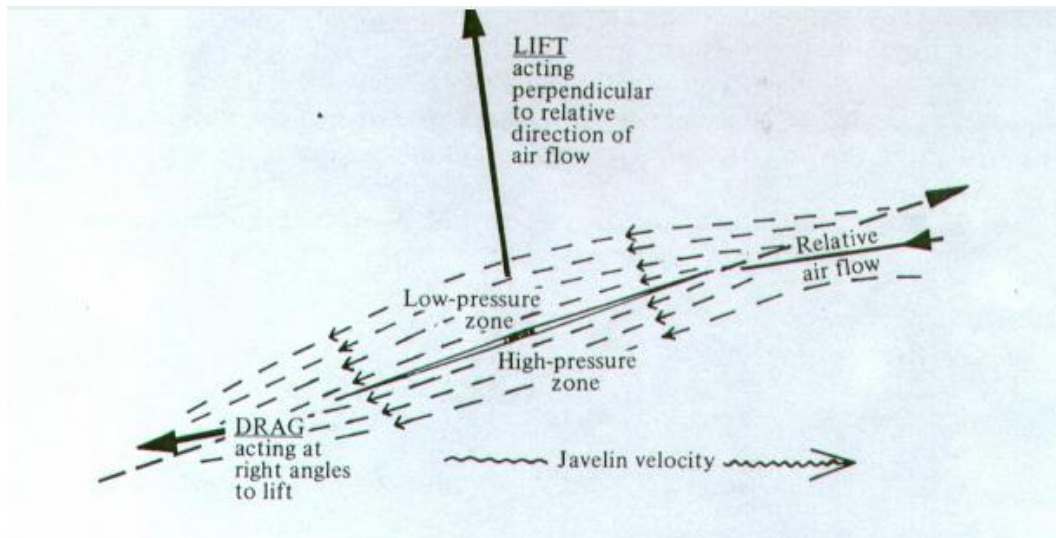


Figure 4: Aerodynamic Forces on Javelin (javelin World)

The Aerodynamic forces on the Javelin structure and its behavior during the flight are shown in the Figures 3 & 4.

2.1.4 Shot Put

Another old support with a comparable intend to plate and spear is known as shot putting, yet the tossing development is restricted to a round base. As opposed to the disk or spear, shot put is moderately hefty. Subsequently, the distance recorded for shot put toss isn't similar to the disk or lance.

The advancement of shotput research centers around the biomechanics viewpoint especially the methods employed during this sport. There are some studies available on the proper execution procedure which is further dependent upon the athlete's skill set and execution procedure as close as possible to perfection (Maheras, 1995; Lichtenberg and Will, 1978).

In the shot put, most investigations were led to decide the ideal delivery point. It has been observed that the launch speed has a much larger effect on the range than the impact of the delivery point. Also, specialists tracked down that the ideal delivery point is typically under 45 degrees presented by Bartoniez in 1995 which was previously predicted by McCoy in 1984.

2.2 Aerodynamics of Circular Planform Wings:

This section provides a descriptive review of the aerodynamics literature for circular planform wings.

2.2.1 Frisbee:

To carry out this research various models have been observed to get the desired results it includes the aerodynamic study proposed by a US navy project on the disc wings which demonstrates the development of a self-suspended design of flare by using an axis-symmetric design of the flying disc with the help of a spin stabilizer (Stilley, 1972; Stilley & Carstens, 1972). Different shapes as the Frisbee, clay pigeon and right circular cylinders were studied in the wind tunnel under several flare configurations. The results obtained from the study of the hollow design of the non-spinning frisbee model demonstrate the values in the form of plots of the angle of attack against the moment coefficients covering pitching, axial normal coefficients. Allowing to capture the general trends. The normal curve for the Frisbee-like model shows a linear behavior below the stall at around 35° AoA and the pitching moment, taken about the semi-chord position, is linear with a positive gradient trimmed just above 10° AoA. However, comparing solid (cavity filling) and hollow horns, the influence of the cavity makes the nose-down pitching moment greatly changed. The effect of rotation on the aerodynamic load is studied on a right cylinder ($t_h \ll c$). In this work, the effect of rotation may be negligible. The proposed technique for measuring the aerodynamic load of the "Magnus Effect" is based on a complex test model supporting structure. The author puts forward the suggestion that their side spur installation method introduces a greater interference effect, especially at the angle of attacks with the higher values to solve the problems related to the onset of the aerodynamic stall which occurs prematurely. They concluded that there is a problem with the accurate measurement of aerodynamic loads due to rotation, and it is recommended to use it as an area for further research. Compared with other conventional and unconventional car bodies, the measured value of aerodynamic damping of a flying disc (hollow) is considered to be very small, and its pitch damping coefficient is about 0.5 for the range of positive angle of attack.

Lazzara et al (Lazzara et al., 1980) conducted experiments on the varying loading conditions focusing on the aerodynamics of the flying disc having a frisbee-like design and provides measured results along with a balanced wind tunnel model to conduct these experiments. It covers the evaluation of various necessary parameters including the aerodynamic forces of drag and lift at the varying values of the spin rates and the flow fields. In this study, the experiments were conducted at a narrow range of attack angles from 0 degrees to 10 degrees. In this study, it is also, concluded that the spinning of the disc generates the lift to a very small extent, although this may be a simple result of experimental accuracies.

Ali (Ali, 1998), in an undergraduate project at the University of Manchester, measured lift, drag, and pitching moment of a spinning Frisbee over the increasing value of the spin rates and the angle of attaching at a specified range is showing a useful starting point for the design of a wind tunnel mounting rig for a spinning disc.

Mitchell (Mitchel, 1999), as part of his Master's thesis at the University of Nevada, conducted experiments on the three configurations of the non-spinning design of the disc wings to measure the reaction forces of lift and drag at the varying range of the flow speeds. The results were plotted for each AoA (-20° to 20°) separately in the form of L/D ratio against Re . The vastly different curves were attributed to the varying camber and contour of each disc wing. These graphs suggest that all three discs were strongly Reynolds number dependent, over the entire range of angles and flow speeds tested. The research findings obtained from the research study of the specified models show results with very different trends such as the aerodynamic loading conditions are independent of the value of the Reynolds number at a more comprehensive range of the values of tested flow fields. The flow behavior visualization by using the tuft and smoke techniques enabled the observation of the upwash before the leading edge, at the downwash after of the trailing edge, and the existence of trailing edge vortices, although the images included in the report are merely clear enough to see their existence and nothing more. The flow over the upper surface was described to be completely attached throughout whereas the lower (concaved) surface was entirely detached and separated. The effect of spin was deemed to not affect the development or location of boundary layer flow structures. Although the above statements regarding flow visualization are perhaps correct for low angles of attack the present research offers discussion and evidence to suggest otherwise. The separation of the bubbles, the cavity of the shear layer again attached to the cavity at a lower value of the attack angle such as 5 degrees, and the flow behaviors shown by the spinning discs is very much different from the non-spinning disc cases are incorporated on the upper surface of the specified flows. Also, the important point to be noted here is that in the spinning disc cases the flow behavior and direction in the separation bubble range are very much affected by the movement of the disc surface at the locality.

Higuchi et al (Higuchi et al., 2000) studied the effects of the fluid flow on a disc which is similar to the golf disc in this present specified research. In this study, the methods of particle image velocimetry (PIV) and the smoke wire flow demonstration are used for the specified

investigation. A laser light sheet was used to illuminate various flow structures including trailing vortices, the separation bubble, and upper & lower (cavity) surface streamwise flow cross-sections, both on spinning and non-spinning discs. If the value of the angle of attack is considered to be of higher value (30 degrees) the shear layers which are separated are forced downwards by a strong pair of trailing vortices, which also, remains consistent during the observation in this study. Vortex strength was calculated from PIV results. When compared to the non-spinning baseline case, the vortex strength remained unchanged for a spinning disc for a lower value of the attack angle (5°) but decreased for a higher value of AoA (15°). A reduction in circulation was stated to cause the loss of vortex strength, attributed to the separation bubble becoming larger with spin. Enhanced lift at low AoA (5°) and reduced lift at higher AoA (15°) are described as being due to the effect of spin, based on observations of the wake. Load measurements from the present research, for an equivalent Reynolds number (10m/s), confirm that the lift enhancement, as a result of the spin, decreases with increased AoA. At no point is the lift reduced, however, although the shape of the golf disc is slightly different from the disc tested in the present study and as such, the two shapes may exhibit contrasting aerodynamic loads. The reduced strength of the two trailing vortices with spin is attributed quite rightly to the change in effective camber on advancing and receding surfaces. This paper also incorporated flow visualization results, proposing a flow topology for a flat disc at incidence. Their wind tunnel model comprised a right circular cylinder with rounded edges, similar to the coin-like cylinders studied by Zdravkovich et al (Zdravkovich et al., 1998). Yasuda (Yasuda, 1999) studied the aerodynamic characteristics of a recreation disc usually used for sports and obtained the values of lift and drag coefficients, analogous to the one tested in the present study, and a flat plate disc also. The wind tunnel results were taken for various flow speeds & spin rates but were consistently lower than the measurements taken in the present study, across the board, for both the cambered disc and the flat plate also. Systematic balance errors or coefficient calculation errors could account for this. Both spin and roughness strips (ridges) were found to not affect the load measurements. Nakamura & Fukamachi (Nakamura & Fukamachi, 1991) observed the flows interacting with the frisbee and obtained results by employing the smoke wire method. The characteristics observed from this study are as follows: If the horizontal plane which is related to the smoke filament becomes aligned with the top surface of the specified disc model displays a wake region that shows symmetric behavior in a non-spinning case. The effects of the spin caused

by the vertical grid of the smoke which flows downstream the disc shows a trailing vortices behavior in the form of pair at the back of the disc shows a wake region with the asymmetric pattern. The asymmetric wake region is created due to the trailing vortices appeared at the back of the disc due to the smoke grid in a vertical direction downstream of the disc. They concluded that the spinning disc strengthened the trailing vortex pair thereby enhancing the downwash. Although an asymmetric downwash is commonly observed in the wake of a spinning disc, the Advance Ratio ($AdvR = 2.26$) was not matched to that which would be typical in flight, i.e. $AdvR < 1$. The present study has shown that the lift increases with high $AdvR (>> 1)$ at low Re numbers, which confirms this conclusion. However, with increased Re number, equivalent to typical free-flight conditions, the $AdvR$ is more weakly dependent upon spin. This suggests that the vortex strength enhancement is dependent upon $AdvR$. However, this was overlooked due to the study being limited to a single test case for a spinning disc.

There are two multiple factors on which the stable frisbee flight is dependent upon but mainly it relies on two physical concepts that includes the gyroscopic Inertia and the Bernoulli's principle (The aerodynamic forces such as lift force). The spinning disc remains stable due to the stability which is provided by the angular momentum and the aerodynamic lift due to Bernoulli's principle.

2.2.1.1 Aerodynamic Forces:

There are two types of the main aerodynamic forces which play their role during the frisbee flight are the lift and drag forces. The lift force which occurred on the frisbee is the aerodynamic force which plays its role in creating the lift during the flight and is caused by the vertical forces acting upon the frisbee body (V. R. Morrison, 2005). This force is very much similar to the aerodynamic lift generated on the airplane wings and is determined by using the Bernoulli's principle. This principle states that the velocity, pressure and the height of the fluid at any random point on the same streamline are interconnected such as the fluid that is moving at a higher speed will have the lower pressure then the fluid moving at a comparatively lower speed. The lift and drag forces acting upon the frisbee are shown in the below figure,

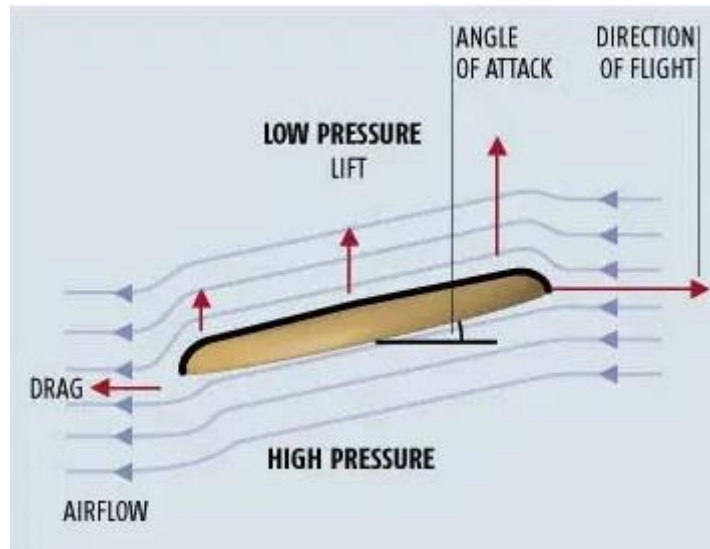


Figure 5: Aerodynamic Forces on the Frisbee (UPREPANDYPHAM15, 2015)

2.2.1.2 Stability of Flying Frisbee:

The other important factor which plays its role in the stable frisbee flight is the rotation of the frisbee during the flight. It is due to this rotational effect that frisbee is able to cover long distances while remaining stable during the flight. This is due to the factor that the aerodynamic lift and drag forces are not directed at the center of the frisbee body such as it has been observed that the lift force which is acting at the front side of the frisbee body shows a slightly higher value than the lift force generated at the back of the frisbee (V. R. Morrison, 2005). As a result of this the torque occurs on the frisbee demonstrated in the figure below where the COP represents the center of pressure and COM represents the center of mass,

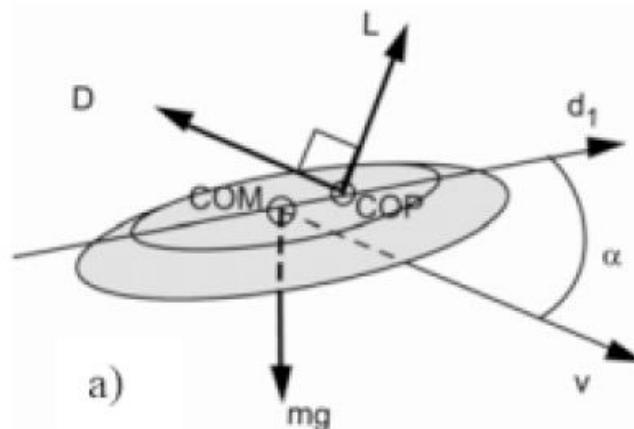


Figure 6: Torque generated due to center of pressure and center of mass (V. R. Morrison, 2005)

2.2.2 Discs:

Independent studies by Ganslen (Ganslen, 1964) and Tutjowitsch (Tutjowitsch, 1976) observed the performance of the aerodynamic forces such as lift and drag at the discs and measured these values field athletics. Ganslen's (Ganslen, 1964) load data (lift and drag) shows variation with velocity i.e. Reynolds number change, especially at high AoA (30° to 50°). His smoke flow visualization (flow speed 18 m/s) depicts the discus flow field both in planform and cross-section at various AoA including the trailing vortices, separation bubble, and deep stall flow structures.

Kentzer & Hromas (Kentzer & Hromas, 1958) conducted research and measured more variables depicting the behavior of the specified model such as the pitching moment along with the other aerodynamic forces. In this study the effects of the spinning disc have also, been observed on varying aerodynamic loads has also measured although the presented spin rate (2.5 revs/sec) is well below that for typical discus throws, 5 to 8 rev/sec (Ganslen, 1964). The effect of spin does not change the lift and drag curves except to prolong the stall (24°) by at least 4° .

Much of the load data in the available reports present measurements that agree only with their general characteristics. The researchers disagree on stall AoA , there are discrepancies in lift curve slope and the form of the drag curve also. It is interesting to see the decrease in drag at stall measured by both Kentzer & Hromas (Kentzer & Hromas, 1958) and Tutjowitsch (Tutjowitsch, 1976) however Ganslen (Ganslen, 1964) does not report any such thing. None of

the above investigators have presented a thorough study of the effect of spin on the aerodynamic loads over a range of typical flight speeds. The only offering being from Kentzer and Hromas (Kentzer & Hromas, 1958) who presented the lift, drag, and pitching moment for one speed and one non-zero spin rate only.

No one to the knowledge of the author has measured the spin-dependent aerodynamic rolling moment, yawing moment, and side force. There is a need for a more definitive aerodynamic study of the discus to corroborate the present experimental work currently available on the subject.

2.2.3 Coin-like Cylinders:

In related work, Zdravkovich et al (Zdravkovich et al, 1998) researched a specified model which he called the 'coin-like cylinders', and observed the effects of aerodynamic forces on it. The thickness of the model is described through the chord ratio $t_h/c \ll 1$, in it the cylinder height is represented by the thickness t_h and the diameter of the cylinder is explained through chord c . In this study, the additional component of the talcum powder paraffin is applied onto the surface of the cylinder in the form of the film to observe the flows over that surface. The patterns over the model surface due to the specified flow display the same kind of behavior which is most similar to the current experimental work which is also named the straight-line reattachment and the separation line of semicircular shape. All of these results were obtained from its plan to observe the model from parallel to the desired free stream. The results obtained from this study gave a great understanding of the fluid-structure interaction over the selected model of a cylinder and created a space to incorporate the flow topology. Unfortunately, the study was limited to 0° angle of attack and as such has limited relevance in the context of the present study.

2.2.4 Analysis on Span Effectiveness Factor:

As a way of evaluating the relevant aerodynamic load data, within the literature, for circular planform wings, a graph of C_D against C_L^2 was plotted in Figure 7.

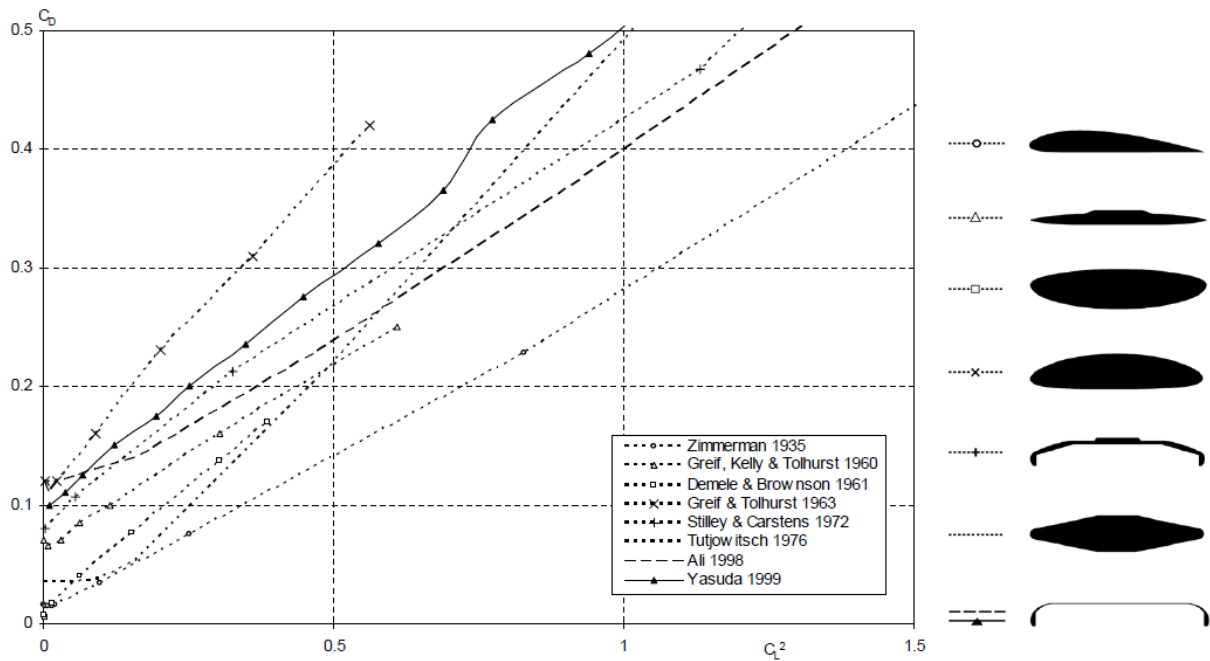


Figure 7. Comparison of aerodynamic load data for circular planform wings, derived from various sources found in the literature, with chordwise cross-sections as seen to the right of the figure (Potts et Crowther 2002).

However, the graph in Figure 7 is considered here as a way of analyzing the Span Effectiveness factor e for circular planforms. The Span Effectiveness or Span Efficiency factor e is a measure of the drag induced by a finite wing, the theoretical maximum being $e = 1$ for the distribution of aerodynamic lift in the form of elliptical shape which also contributes to decreasing the value of the induced drag, Anderson (Anderson, 1991). Also, the curves plotted in Figure 7 are for a variety of different geometries with chordwise cross-sections as seen in the key next to the figure.

To understand the similarities between various circular wing shapes, the gradient of respective curves is compared by means of the span efficiency factor. The gradient of each curve in Figure 7 is given by $(\pi e AR)^{-1}$ and the AR is identical for every wing with circular planform. Therefore the AR is $4/\pi$ and the gradient is given by $0.25 e^{-1}$. Taking the gradient of the experimental curves in Figure 7 we can calculate the span effectiveness e .

The values of e for the circular planform geometries compared in Figure 7 vary between 0.5 and 0.8. The graph shows Frisbee-like wings with approximately the same span effectiveness $e \sim 0.8$, namely Stilley & Carstens (Stilley & Carstens, 1972) and Ali (Ali, 1998), however Zimmermans (Zimmermans, 1935) planar wing also has similar gradient or in other words $e \sim 0.8$. The graph also shows Frisbee-like wings with contrasting gradients, namely Stilley & Carstens (Stilley & Carstens, 1972) and Yasuda (Yasuda, 1999) have span effectiveness $e \sim 0.8$

and 0.6, respectively. However, recall that the measurements Yasuda (Yasuda, 1999) took are expected to have systematic errors, which would account for the lower span efficiency here, $e \sim 0.6$. There are also examples of similar planar wings with approximately the same span effectiveness $e \sim 0.5$, namely Greif & Tolhurst (Greif & Tolhurst, 1963) and Tutjowitsch (Tutjowitsch, 1976).

In general, the curves for Frisbee-like wings have similar magnitudes and similar span effectiveness $e \sim 0.8$. However, circular planar wings with thin crosssection also have similar span effectiveness to the Frisbee-like wings, $e \sim 0.8$. Circular planar wings with thick cross-sections have much lower span effectiveness, $e \sim 0.5$. The Frisbee-like shape, therefore, has large span effectiveness, relative to other circular wings of identical aspect ratio, within the literature. The Frisbee-like shape, therefore, has similarly induced drag to a thin circular wing, such as the Zimmerman (Zimmerman, 1935) Clark Y, but lower induced drag than thick solid wings, such as the discus. This is an indicator of the inherent flow structures created over a circular wing, namely trailing vortices in close proximity which induce a strong central downwash with associated spanwise lift distribution and thus span efficiency factor. However, the fact that thicker circular wings have lower span efficiency suggests that the presence of the cavity on the Frisbee-like shape returns lower induced drag back down to a value similar to planar wings. However, even though they both have a similar span efficiency factor, the spanwise lift distribution for Frisbee-like and planar circular wings could well be different.

2.3 Flight Dynamics of Spin-stabilized Disc-wings:

2.3.1 Frisbee:

Katz (Katz, 1968) developed a simplified mathematical model of a rotating flying disc treating the spin as an independent parameter. Firstly, considering linear aerodynamic moments alone, the derivation of classical stability criteria was given, including steady-state results. A non-linear model was derived by adding a lift, drag, and gravity forces, so that typical flight trajectory solutions could be calculated numerically. From the stability analysis, the increased spin rate was shown to [spin-] stabilize the motion towards a constant precession rate condition. This work is sketchily written and difficult to follow with no formalized conclusions. The flight trajectories are largely two-dimensional and difficult to visualize with scant information.

Lissaman (Lissaman, 1994) considered the dynamics of a spinning oblate spheroid including

mathematical stability analysis. The development of a characteristic dynamic's matrix from the equations of motion and subsequent decomposition into dynamic groups enabled the modes of the dynamic motion to be determined from the roots of the characteristic equation. A formal dynamic analysis approach enabled the interpretation of the dynamic modes with specific reference to the flying sports disc. Numerical results for a Frisbee disc, with launch parameters chosen carefully to match a realistic throw release, were analyzed and compared to Stilley & Carsten's (Stilley & Carstens, 1972) data. The dynamic modes for both discs were found to be quite similar, their behavior supported by actual flight tests (Stilley & Carstens, 1972).

Revisiting disc flight dynamics, Lissaman (Lissaman, 1998) presented the linearized equations of motion and discussed various numerical codes used to solve them. However, problems arose when attempting to integrate the flight equations, it was noted that very small time steps were required to maintain convergence which suggests more computational power was needed. Lissaman (Lissaman, 1999) also described the aerodynamics at zero spin rate & nonzero spin, the gyroscopic dynamics, and both the longitudinal & lateral flight trajectory. Much of the discussion was based on wind tunnel results from the early data collected for the present study. An approximate solution of the longitudinal and lateral trajectories was described but not presented, aerodynamic coefficients were taken from the present research. The rolling moment caused by the spin dependency occurred due to the delay in the separation on the sides retreating from each other and due to the quick separation occurring on the sides advancing to each other which makes the spanwise lift distribution asymmetric. However, the local surface moves across the flow on the leading edge of a spinning disc, directly along the arced separation rather than advancing or retreating. Therefore, it is not possible to treat the fluidic generation of the rolling moment so simplistically, the rolling moment is generated by a unique combination of interacting flow structures over an axisymmetric body with a rotational slip condition. Latterly, Lissaman (Lissaman, 2001; 2003a; 2003b) worked on the projectile motion of the flying discs and while observing their behavior he selected the maximum range for this stated flying disc model compared to the other available studies, mainly spheres.

Hummel & Hubbard (Hummel & Hubbard, 2000; 2001; 2002; 2003; 2004) analyzed both the Frisbee throw and flight, from throw biomechanics through the development of a numerical flight path simulation, even to the extent of identifying aerodynamic coefficients from free-

flight tests. Hubbard & Hummel (Hubbard & Hummel, 2000) has studied and developed a special model with the 5 degrees of freedom simulations and defined the paths or the trajectories for a basic design of frisbee successfully. Hummel (Hummel, 2003) also, experimented with the proposed models along their supposed trajectories as well.

The simulation included a (linearized) dynamic model for obtaining the required parameters or data from the experimental flight tests and identified those by comparison with the theoretical calculations (Hubbard & Hummel, 2002). Free-flight experiments accurately tracked the position of a Frisbee with the help of high-speed or high-quality three-dimensional video cameras. Linear approximations to aerodynamic coefficients were derived from the flight data and compared reasonably well to wind tunnel data from the present study.

While obtaining the desired parameters from the original test flights is quite difficult and as well as challenging at the same time because of multiple varying conditions along with uncertain circumstances. Also, it is quite different from wind tunnel testing as well due to the distributed or the scattered results. In addition to that, the only way to obtain the desired or considerable results is to define the parameters linearly around the already defined flight conditions. It has also been observed that the only information that exists on the derivations of the rate dampening parameters (Hummel & Hubbard, 2000; 2002) is from the experimental tests of the flights, it also provides a piece of very reasonable information for carrying out the theoretical or the simulation work.

The biomechanics of Frisbee throwing (Hubbard & Hummel, 2001) is a very important phenomenon that offers very integral values on the conditions of the launching such as the spin rate, velocity, and the varying distance from the ground (altitude) which not only helps in carrying out practical experiments but also, provides very useful information to carry out the computational studies of the systems and gives leverage to optimize the performance outcomes as deemed necessary.

With maturity, this study has the potential to accurately simulate the Frisbee throw and resulting flight trajectory, with the power to yield the optimal throwing technique for various purposes, such as maximum range. It could also be used to analyze the throwing technique of specific athletes. In the presented work, however, the simulation did not progress much further than the validation and the biomechanics model was not taken far enough to couple the two.

Pozzy (Pozzy, 2001) also, provides a piece of very useful information by conducting

experiments on the relation between the speed at which the disc is thrown and its range by clocking the disc release speed at launch, from a professional field of disc golf players, with a radar gun. The range was plotted against launch speed on a scatter graph and the best fit line was drawn to show the correlation. Although it is no great surprise that the range increases with higher release speeds, this is a useful resource for the comparison of simulated predictions. Lissaman (Lissaman, 2003b) recently considered the 2D flight dynamics to find the upper bounds for maximum range via an optimization procedure. The solutions were plotted alongside field results (Pozy, 2001) and found to have a reasonable agreement. In both cases, the dependence of range on velocity was modeled with a straight line, in spite of the quadratic dependence of the launch speed on the range. Lissaman (Lissaman, 2003b) noted that this was due to energy dissipation by drag at high velocities which reduced the favorable effects of lift. It is helpful to bear in mind that the golf throw data was collected in various locations, wind conditions, and topology. This could explain the cluster of scattered points that represented long-range achieved for moderate launch speed, which was attributed to the throwing technique (Pozy, 2001).

Cotroneo (Cotroneo, 1980) analyzed biomechanics, lift, and the drag parameters of the flight of a disc detected on the basis of the initial thrown conditions or the observations. The study was focused on the comparison of back-hand and sidearm (fore-hand) throwing techniques for maximum distance, including a biomechanics analysis of the athlete subjects with contrasting throw actions yet exceptional range. Minimal wind tunnel test results for a Frisbee without the concentric rings [that forced boundary layer transition] on the upper disc surface, reduced the optimum release of the attack angle and also, improved the aerodynamic performance ratio (lift to drag ratio). The velocity at which the disc is released is a very important parameter because the range that the disc will cover is directly related to its initial speed. Both back-hand and sidearm throwers could achieve approximately the same range. Pozy (Pozy, 2002) experiments also, verified the relation between the initial speed and the distance as it also, experimented with the different techniques of the launching or throwing of the discs and analyzed the videos of the discs by the golf professionals recorded from the high-speed cameras.

Recently, Lorenz (Lorenz, 2004) began to investigate the free-flight dynamics of a Frisbee via measurements from onboard instrumentation. A varied array of real-time data was recorded in flight from pressure sensors, accelerometers, a sensor with infra-red capabilities, and the

magnetometer which is also mounted within space at a Frisbee and uploaded to a computer post-flight. The flight trajectory was recorded using a conventional video recorder, digitized, and converted into physical distance. The body attitude was calculated from data taken with the various sensors and velocity computed from the video record. The aerodynamic force coefficients could then be calculated from the instantaneous accelerations and the pitching moment from the precessional roll rate, which was derived from the attitude record. The aerodynamic loads were compared to the wind tunnel data of the present study and agreed upon. However, only two points were plotted on each graph of lift, drag, and pitching moment and as such were merely only verification that the instrumentation was providing realistic data. The discrepancy available within the experimental free flight data and the data obtained from the wind tunnel sometimes provided the higher values of the pitching moment and the aerodynamic drag coefficient for this present study but still, the obtained results remained in the range of wind tunnel data to profess a successful correlation. The ongoing research by Lorenz, using this onboard instrumentation methodology, is potentially an extremely useful way of gathering aerodynamic data in free-flight or even within the wind tunnel environment. Future work is proposed to determine the effect of spin on the separation and measure the surface pressure distribution on a spinning disc.

Danowsky & Cohanin (Danowsky & Cohanin, 2002) sought to develop a computer model that predicted aerodynamic parameters and use these to simulate free-flight trajectories, which was a similar study to that of Hubbard & Hummel (Hubbard & Hummel, 2000). Instead of deriving parameters from free-flight experiments, they used potential flow theory that was slightly modified to account for the spin.

A wind tunnel balance was constructed from a combination of load cells to give 3dof, set in two positions one which picked up Lift, Drag & Pitching Moment and the other Lift, Side Force & Rolling Moment. A golf disc (Frisbee) was fixed to the balance via a motor-driven axle, at 0° angle of attack, to test at various flow and spin rate combinations. The flexibility of the plastic disc particularly at the center meant that it deformed during high wing loading, observed most dramatically at zero spins but also causing a nose-down orientation for the spinning disc. The solitary angle of an attack test case, deformity of the test model, and the omission of matched advance ratios over the flow rate test range limit the accuracy of the data. Smoke wire flow visualization was used to record the port and starboard side wash angles from the spinning disc.

Potential flow theory was applied to a virtual disc geometry, similar to that tested in the wind tunnel, to predict aerodynamic parameters. The vortex lattice method was applied to the disc, accounting for a spin by the use of a slip boundary condition. The side wash angles were plotted against advance ratio and were deemed to be dependent parameters, however, their plots show two scattered arrays which suggested independence. These angles were required by the computer code to specify the trailing edge. Steady-state solutions were obtained iteratively using a wake evolution methodology from which aerodynamic forces could be computed. Simulated flow visualizations based on the wake solutions show the presence of trailing vortices.

The inputs to the flightpath model were derived from the zero angles of the attack case alone and as such the accuracy of the trajectories is somewhat dubious. Nevertheless, for high spin rates the plotted trajectories modeled the gyroscopic roll stiffness, the disc held its orientation in a much straighter lateral flight path. The effect of the bank angle launch condition was also illustrated.

The accuracy of the results obtained during this research need to be improved further keeping in mind the sheer breadth of the subject matter and the analysis techniques employed. The wind tunnel tests and the potential flow solutions were limited to the zero angles of attack, which restricted the derivation of aerodynamic inputs solely from this single orientation. The application of potential flow and wake evolution is a new approach to the Frisbee.

Tuck & Lazauskas (2004) applied a general lifting surface computer code to the circular planform, in order to compare lift and pitching moment to semi-analytical solutions. Expanded solutions to include axisymmetric discs modeled a simple Frisbee-like profile closely. A combination of these solutions was then used to outline another set of axisymmetric cross-sectional profile solutions that eliminated the pitching moment entirely but as a result, drastically reduced the lift too. Eliminating the pitching moment is a highly desirable property of flying discs as it eliminates precessional roll. It is good to keep in mind, however, that these solutions are theoretical and as such do not model turbulent and separated flow regimes that dominate the flow over a flying disc in the air.

2.3.2 Discs:

The earliest study of discus flight (Taylor, 1932) was initiated by the Intercollegiate Associations of Amateur Athletics of America (ICAAAA) in response to a puzzling question posed by discus throwers who noticed that they could achieve greater distances when

throwing into a headwind. Taylor (Taylor, 1932) investigated this observation using wind tunnel tests and a flight path simulation to offer practical guidelines for intelligent throwing in a prevailing wind. The wind tunnel data and details of the mathematical analysis were not published however, only results of predicted (2DOF) longitudinal flight paths based on a variation in ambient wind velocity. The model predicted the optimum attitude (35° to the horizontal) and angle of attack (0°) given to the discus at launch to achieve maximum range, for still (no wind) conditions. Using the no-wind case as a baseline, Taylor's (Taylor, 1932) calculations suggested that a headwind increased the range whereas a tailwind decreased the range.

As the discus is released for an efficient throw in still air, it is oriented to maximize lift and minimize drag in the climb portion of the flight (Frohlich, 1981). Investigators roughly agree that optimal release angles are around 30° attitude and -10° AoA (Bartlett's Table 1, 1992). As the results for aerodynamic lift show a negative value at the beginning of the flight but (Ganslen, 1964; Frohlich, 1981), the discs make use of the low drag, negative AoA range to minimize deceleration over the climb portion of the flight. The initial upward momentum on release projects the discus away from the ground and it isn't until the discus reaches the zero-lift AoA (0°) that there is any aerodynamic lift contribution. The discus generates lift throughout the middle portion of the flight at the highest elevation, with a higher rate of deceleration due to the increased drag at high AoA. As the discus descends during the latter portion of the flight, the drag approaches a maximum further retarding the speed as the discus flight path approaches vertical back to the ground. A negative AoA at launch is arguably impractical (Samozwetow, 1960) as it limits the speed and stability given to the discus on release. However, Terauds (Terauds, 1978) reported a launch AoA range of -10.5° to -27.5° for elite male discus throwing athletes, which supports the calculated optimum AoA values reported in the literature.

Contrary to the common assumption that the discus attitude is constant throughout the flight, small aerodynamic moments will cause the disc to pitch and roll. Samozwetow (Samozwetow, 1960) reported the roll left wing tip down and subsequent banked left turn towards the end of the discus flight, caused by the (nose up) pitching moment. As the discus rolls the AoA is reduced, Hubbard (Hubbard, 1989) suggested that this may cause a favorable change in pitch attitude gaining an aerodynamic advantage in flight. Tutjowitsch (Tutjowitsch, 1976) claimed the discus bank angle could be ignored given high spin rates. However, Soong's (Soong, 1976)

simulation predicted the range to be spin-dependent (Soong, 1976) for typical and atypical discus throw spin rates, from 4 up to 740 rev/sec. Voigt (Voigt, 1972) also reported an increase in range with increased spin rate, based on flight test observations.

3. Theoretical background:

This chapter introduces the theoretical analysis of the key aspects of disc wing geometry, aerodynamics, and flight dynamics. This includes deriving the geometric parameters of the disc wing related to aerodynamics, a simple aerodynamic model with the aerodynamic characteristics of lift and drag for the desired model of disc wing were estimated based on the finite wing theory and basic drag, and the effect of the pitching moment characteristics on the general pitch and stability. Affect the tailless aircraft, determine the pitch moment design requirements of the successful disc wing and the basic power of the disc wing flight, and determine the non-dimensional roll rate parameter that characterizes the trajectory of the disc wing.

3.1 Numerical Analysis of Disc-wing:

Multiple parameters are available which could be utilized to describe the disc wings but the most important one is its diameter which is identical to a variable 'c' called the 'root chord' and is usually measured from the middle surface of the disc and is described as the characteristic length of a disc wing. The characteristic length also helps to define the reference area of the wing (Equation 1).

$$S = \pi \frac{d^2}{4} \quad (1)$$

By definition, the aspect ratio of a circular planform is given by Equation 2.

$$AR = \frac{b^2}{S} \quad (2)$$

where b is the wing span at the mid-chord station, such that $b = c = d$. Therefore, the circular planform is defined as in Equation 3.

$$AR = \frac{4}{\pi} \sim 1.27 \quad (3)$$

The thickness to chord ratio c is defined using the root chord c . The thickness t_h is taken as a distance that is measured orthogonally from the disc-wing rim tip above the flat central plate. This is really a non-dimensional measure of the amount of maximum camber, used here for ease of comparison between disc-wing shapes within the literature. The boundary conditions

are shown on the disc in the Figure 8,

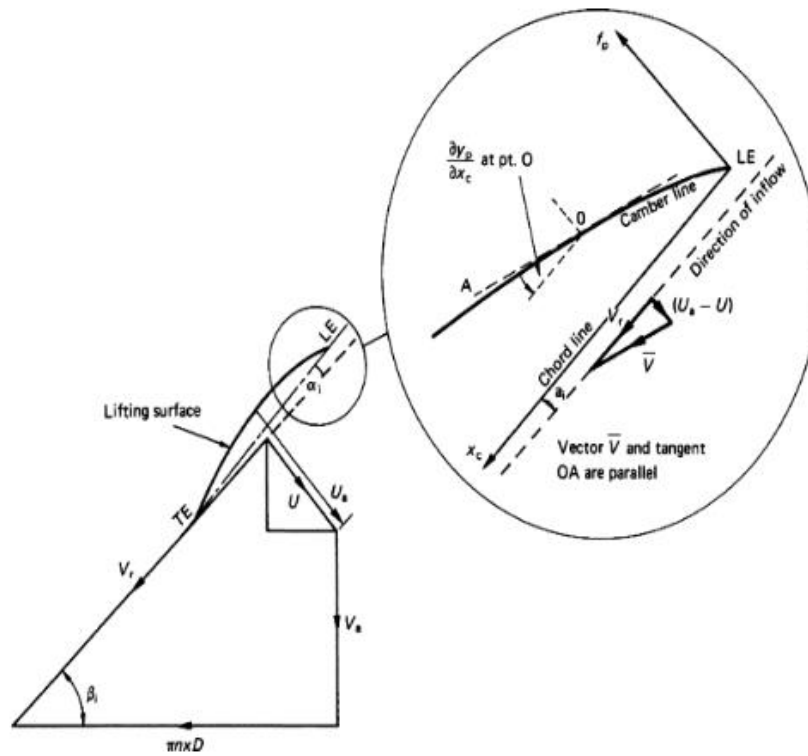


Figure 8: Boundary conditions for aerodynamic calculations (JS Carlton, 2007)

Typically, a Frisbee has the thickness to chord ratio of around (Equation 4):

$$\frac{t_h}{c} \sim 0.15 \quad (4)$$

The mean chord \bar{c} for the disc, planform is given by Equation 5.

$$\bar{c} = \frac{\pi c}{4} \quad (5)$$

The mean aerodynamic chord MAC, which is the chord-weighted chord, is calculated using Equation 6.

$$MAC = \frac{2}{S} \int_0^{\frac{b}{2}} c_y^2 dy \quad (6)$$

where c_y represents the length of the chord available on the relevant span location y and b represents the wing span. Using cylindrical polar coordinates to define the chord at each span station the integral in Equation 6 becomes Equation 7.

$$MAC = -\frac{4b}{\pi} \int_{\frac{\pi}{2}}^0 \sin^3 \theta d\theta \quad (7)$$

Therefore, the mean aerodynamic chord for the circular planform is given by Equation 8.

$$MAC = \frac{8b}{3\pi} \sim 0.85c \quad (8)$$

3.1.1 Aerodynamic coefficients:

The aerodynamics forces are defined by dimensionless coefficients as aerodynamic Drag Force (**Equation 9**), Side Force (**Equation 10**), and Lift Force (**Equation 11**). These coefficients are calculated by dividing the corresponding aerodynamic force by the dynamic pressure q_∞ and the surface planform area S .

$$C_{Drag} = \frac{\text{Drag Force}}{q_\infty S} \quad (9)$$

$$C_{Side} = \frac{\text{Side Force}}{q_\infty S} \quad (10)$$

$$C_{Lift} = \frac{\text{Lift Force}}{q_\infty S} \quad (11)$$

As the aerodynamics forces, the aerodynamic moments such that the aerodynamic Rolling, Pitching, and Yawing moments (Equation 12-14) can be expressed as dimensionless coefficients by dividing them by the dynamic pressure q_∞ , the surface planform area S and the characteristic length c .

$$C_L = \frac{L}{q_\infty S c} \quad (12)$$

$$C_M = \frac{M}{q_\infty S c} \quad (13)$$

$$C_N = \frac{N}{q_\infty S c} \quad (14)$$

The Axial, Side, and Normal forces being the aerodynamic force components along the body-fixed axes x, y, z are defined as Equation 15-17.

$$C_X = \frac{X}{q_\infty S} \quad (15)$$

$$C_Y = \frac{Y}{q_\infty S} \quad (16)$$

$$C_Z = \frac{Z}{q_\infty S} \quad (17)$$

These forces are related to the Lift, Drag, and Side force as in Equation 18-20.

$$X = \text{Lift} \cdot \sin \alpha - \text{Drag} \cdot \cos \alpha \quad (18)$$

$$Y = Side \quad (19)$$

$$C_z = \frac{Z}{q_\infty S} \quad (20)$$

Where α is the geometric angle of attack (AoA). Pressure is made dimensionless using pressure coefficient C_p defined as in Equation 21.

$$C_p = \frac{p_w - p_\infty}{q_\infty} \quad (21)$$

where p_w is the pressure on the disc-wing surface, p_∞ is the total free-stream pressure and q_∞ the dynamic pressure (Equation 22).

$$q_\infty = \frac{1}{2} \rho_\infty V_\infty^2 \quad (22)$$

Where ρ_∞ is the air density and V_∞ the free-stream flow speed.

3.1.2 Aerodynamic Parameters of Low Aspect Ratio Wings:

The aerodynamic characteristics of a disc wing can be determined theoretically with help of the lifting line theory or by the finite wing theory (Anderson 2017). However, it is noted that the available finite wing theory has a limitation of handling the cases which have an aspect ratio value of more than 2, whereas disc-wings have an aspect ratio of 1.27 as shown before. The application of this theory to the disc-wing is intended therefore only as a first approximation, offering an insightful starting point.

As a first approximation, it is reasonable to use the slope of the lift curve for an infinite wing defined as Equation 23.

$$a_0 = 2\pi \quad (23)$$

It can be shown using an analysis of induced velocity (Anderson 2017) that the lift curve slope of a finite span wing is reduced compared to that of an infinite wing with the same cross-section (Equation 24).

$$a = \frac{a_0}{1 + \left(\frac{a_0}{\pi e AR}\right)} \quad (24)$$

Where a_0 is the lift curve slope of the infinite wing, a represents the lift curve slope of the finite wing and e is the span effectiveness factor.

By definition, the aspect ratio of a circular planform is $4/\pi$ as defined before. Defining a_0 as 2π and e as 1 as a first approximation, the substitution of these values into (2.10) yields a theoretical value of the lift curve slope of a disc-wing (Equation 25).

$$a = \frac{2\pi}{1 + \frac{\pi}{2}} \sim 2.44 \quad (25)$$

Due to the positive camber of a disc wing, the theoretical lift curve is given by Equation 26.

$$C_L = a(\alpha - \alpha_o) \quad (26)$$

Where α_o is the zero-lift AoA. From the experiment the value for α_o was taken to be -2° and C_L may be redefined as Equation 27.

$$C_L = 2.44\alpha + 0.085 \quad (27)$$

The aerodynamic drag generated by the disc-wing can be modeled as the sum of profile drag C_{D_o} and induced drag using the familiar drag polar equation (Equation 28).

$$C_D = C_{D_o} + \frac{C_L^2}{\pi e AR} \quad (28)$$

Due to the bluff nature of practical disc-wing cross-sectional shapes, an estimate of the disc profile drag coefficient can be made by modeling the disc as a sphere of the same frontal area as the disc. The profile drag coefficient can then be obtained by scaling according to the ratio of frontal (subscript f) to planform (subscript p) areas (Equation 29).

$$C_{D_o} = C_{D_p} = \frac{S_f}{S} C_{D_f} \quad (29)$$

The frontal area of the disc can be approximated from the disc center-line thickness to chord ratio (Equation 30).

$$S_f = t_h c \quad (30)$$

and the planform area S is given in Equation 1. Then C_{D_o} can be rewritten as Equation 31.

$$C_{D_o} = \frac{4t_h}{\pi c} C_{D_f} \quad (31)$$

The drag coefficient of a sphere in turbulent flow C_{D_f} based on the frontal area is approximately 0.5 and the center line thickness to chord ratio of a typical Frisbee is approximately 0.15 (Equation 2.4). Finally, C_{D_o} becomes as Equation 32.

$$C_{D_o} = 0.0955 \approx 0.1 \quad (32)$$

The induced drag component at a given AoA can be estimated from known geometric parameters and the lift coefficient as shown before. Thus, the drag polar is defined as Equation 33.

$$C_D = 0.1 + 0.25 C_L^2 \quad (33)$$

Finally, the drag curve can be expressed as a function of α as shown by Equation 34.

$$C_D = 0.1 + 1.5(\alpha + 0.035)^2 \quad (34)$$

Theoretical expressions were compared to experimental results by (Potts et Crowther 2002).

3.1.3 Trim & Stability of Tailless Flight Vehicles:

Some requirements need to be met by a vehicle to achieve a recognizably successful flight. First, the vehicle should be able to derive a force to produce an aerodynamic force of the lift which should at least match the weight of the vehicle, and second, the vehicle should be able to achieve and vary aerodynamic balance such that orientation of the vehicle with respect to the free stream can be controlled (Potts et Crowther 2002).

Additionally, if the vehicle requires a sustained flight further conditions should be met as the facility of the vehicle to generate a thrust force at least equal to the drag force. Lastly, for 'passive' flight vehicles without an automatic flight control system or human pilot and the vehicle should be aerodynamically stable such that when disturbed, it returns to its original balanced state.

Most conventional flight vehicles satisfy the first condition by using a primary aerodynamic surface for generating lift (a wing), and conditions 2 and 4 using a secondary aerodynamic surface (horizontal stabilizer). Whilst the provision of a horizontal stabilizer, in the form of a tailplane or fore plane, is often beneficial to the overall design, it is not a necessary condition for balance and stability.

The disc wing is an example of a wider class of tailless flight vehicles including hang gliders and delta-winged aircraft that only utilizes the one aerodynamic surface which has the capability to provide stability, balance and also, generates the desired lift as well.

The forces that are applied in the longitudinal direction and the moments that are applied on the tailless aircraft are shown in Figure 9.

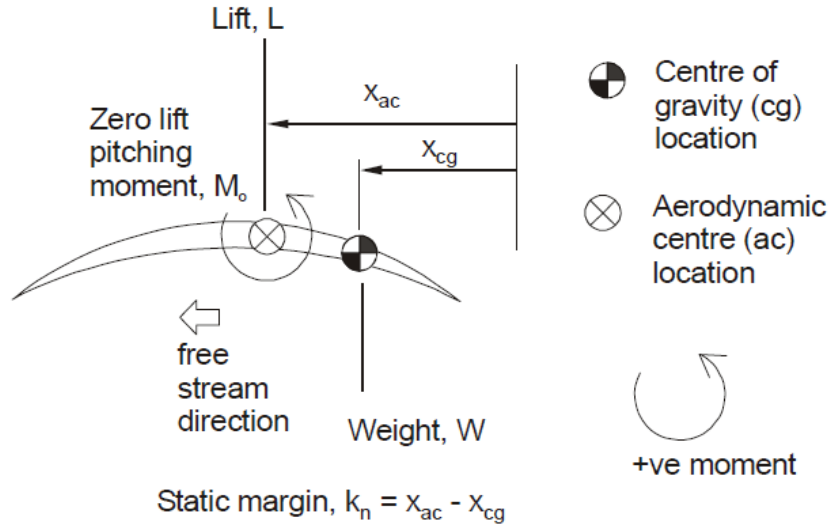


Figure 9. Definition of reference locations for longitudinal forces and moments acting as a tailless flight vehicle (Potts et Crowther 2002).

In keeping with linear airfoil theory (Anderson 2017), the forces and moments are modeled as a lift force, Lift, and zero lift pitching moment, M_o , acting at the aerodynamic center of the section.

For a 2D airfoil section at the reduced speeds and the reduced attack angles (attached, incompressible flow), the zero-lift pitching moment is constant and the location of the center of aerodynamic is situated at a quarterly distance from the chord back from the leading edge. The zero-lift pitching moment is negative for positively cambered sections and positive for negatively cambered sections.

For the moments that are related to the center of gravity of the tailless configuration, the following moment balance equation is obtained (Equation 35).

$$M_{cg} = M_o - Lift(x_{ac} - x_{cg}) \quad (35)$$

Non-dimensional Equation 13 becomes Equation 36.

$$C_{M_{cg}} = C_{M_o} - C_{Lift}k_n \quad (36)$$

Where k_n is the static margin, defined as Equation 37.

$$k_n = \left(\frac{x_{ac} - x_{cg}}{c} \right) \quad (37)$$

The system is balanced, also called trimmed, when $C_{M_{cg}} = 0$. The lift coefficient for trim is therefore given by Equation 38.

$$C_{Lift_{trim}} = \frac{C_{M_o}}{k_n} \quad (38)$$

In order to meet the first condition for the flight above, $C_{Lift_{trim}}$ must be greater than zero. This is achieved if both C_{M_o} and k_n are positive or if both C_{M_o} and k_n are negative. For stability (fourth condition for flight), the change in the moment about the center of gravity with an increase in lift coefficient must be negative (Equation 39).

$$\frac{\partial C_{M_{cg}}}{\partial C_{Lift}} < 0 \quad (39)$$

Finally, is obtained Equation 40.

$$\frac{\partial C_{M_{cg}}}{\partial C_{Lift}} = -k_n \quad (40)$$

thus for stability, k_n must be positive.

It can be concluded that a stable configuration requires a positive C_{M_o} for balance, whereas an unstable configuration requires a negative C_{M_o} for balance. This implies that a stable configuration should have negative camber and an unstable configuration positive camber. Figure 10 compares the pitching moment characteristics with the angle of attack for the four possible permutations of camber and static margin to illustrate the effects of camber and static margin on the stability and trim of a tailless flight vehicle. It is assumed that lift is directly proportional to the angle of attack.

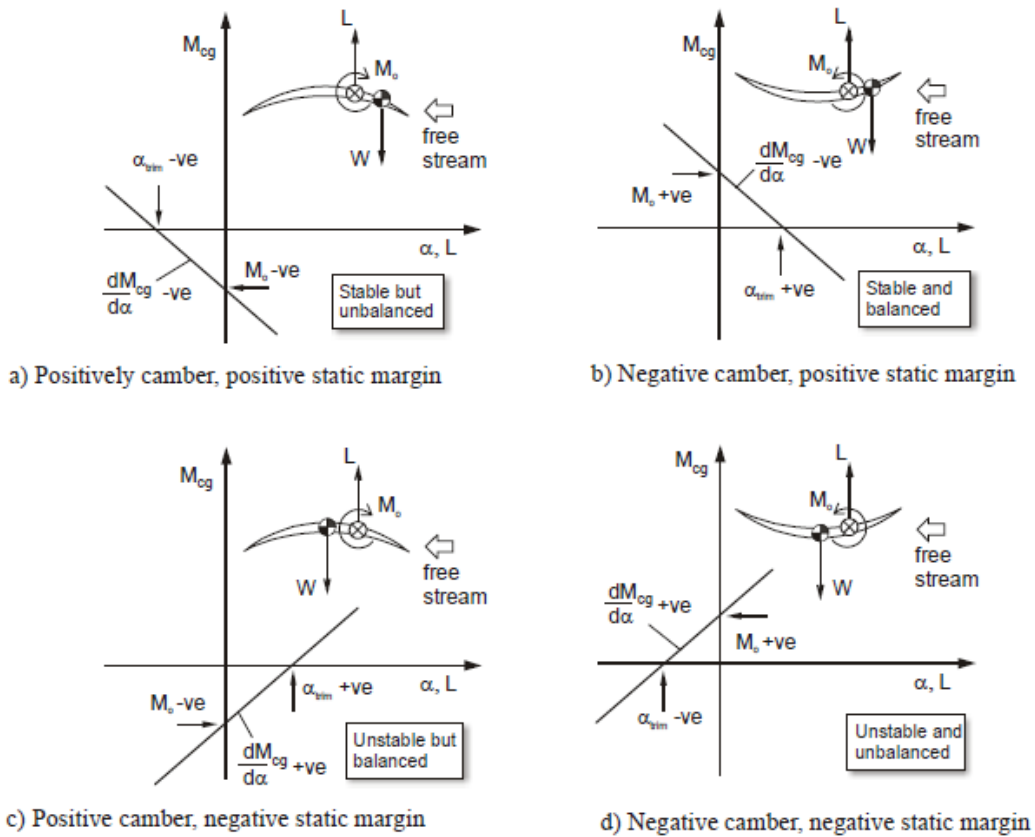


Figure 10. Illustration of longitudinal stability and trim characteristics of a tailless flight vehicle for permutations of camber and static margin (Potts et Crowther 2002).

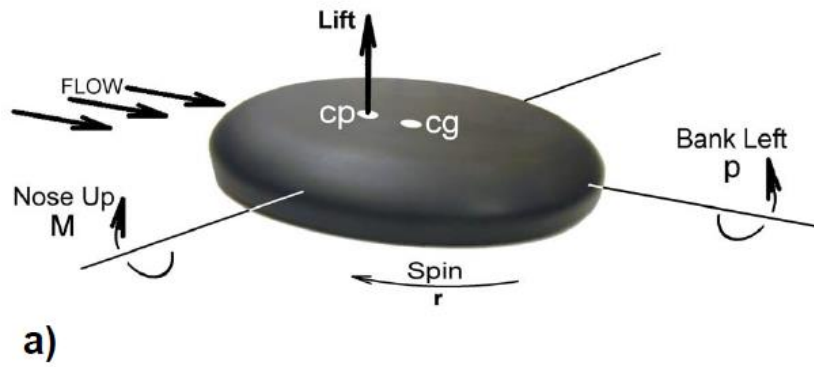
For a stable tailless aircraft C_{M_o} must be positive to provide balance and hence the wing must have negative camber. This configuration is shown in Figure 10b. For a disc wing, the center of gravity must be at the center of the disc, and in practice, the aerodynamic center a point where the value of pitching moment coefficient does not vary with the lift coefficient's value on an airfoil will always be ahead of this point, therefore the static margin will always be negative. Thus, to balance a disc-wing C_{M_o} must also be negative, i.e., the camber must be positive. This configuration is shown in Figure 10c.

A comparison of the aerodynamic center location as a function of angle of attack for both a Frisbee disc and a non-axisymmetric circular planform wing with an airfoil cross-section was made by Zimmerman in 1935 (Zimmerman, 1935). Over the angle of attack range, 0° to 10° the aerodynamic center of the desired Frisbee design is just at a distance equals to the half cord point of the wing disc, giving a static margin of approximately zero and thus neutral pitch stability. For the circular planform wing with an airfoil cross-section, however, the

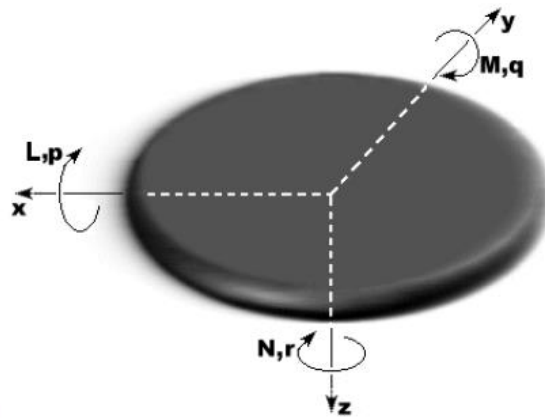
aerodynamic center is at approximately a quarter chord, resulting in a large negative static margin and hence negative stability.

3.1.4 Flight Dynamics of a Spin-stabilized Disc-wing:

The wing disc shows very unique features during the flight and one of these distinctive features is its ability to roll about its direction of motion. This tendency of the disc wing makes its flight different from the flights of the other aircraft and the projectile objects. As an illustration, consider Figure 11a. Also, many other features were observed on the Frisbee type design such as during a normal disc flight at a regular angle of attack if the disc center or C_g is situated at the rear side of the center of pressure (C_p) of the wing can cause the occurrence of pitching moment along the longitudinal axis with the uncut nose-up condition. If the disc continues to rotate then the gyroscopic effect provides the data regarding pitching moment M which could result in a precessional rolling rate, p which is orientation variation of rotational axis in case of the rotating body. With the help of a fixed body axis definition for a conventional body (Figure 11b), if the direction of the rotation of the rotating disc is along with the positive value of yaw r then as a result the pitching moment generated will show a positive value. This could create a pitching moment due to the untrimmed nose-up position. In addition to that, the precessional rolling rate p might appear if the disc starts to rotate and cause the pitching moment M . Also, if a disc is rotating at a direction of positive yaw r by using the conventional body axis which is fixed then a positive pitching moment will generate the roll rate.



a)



b)

Figure 11. (a) Flight dynamics of the proposed Disc-wing. (b) Body fixed axis schematic diagram. The nose would be in positive x-direction in a conventional aircraft (Potts et Crowther 2002).

The aim of this part is to refer to the non-dimensional roll rate parameter based on the disc's physical properties and launch conditions that can be used to predict the approximate flight behavior of the disc. The solve these types of problems first is to set the equations describing the motion of an aircraft with six degrees of freedom (Nelson, 1998). For the calculations we are assuming few conditions such as the horizontal flight path, all the forces will be in equilibrium and the yawing moment is also, considered to be negligible (this assumption is based upon the data obtained from the experimental tests) then the motion of the disc can be obtained from the governing equations obtained from the pitching moment along with rolling moment equations Equation 39-40).

$$L = I_x p - I_{xz} \dot{r} + qr(I_z - I_y) - I_{xz} pq \quad (41)$$

$$M = I_y \dot{q} - rp(I_x - I_z) - I_{xz}(p^2 - r^2) \quad (42)$$

Now for a uniform axisymmetric circular disc (Equation 43).

$$I_x = I_y = \frac{1}{2}I_z \quad \text{and} \quad I_{xz} = 0 \quad (43)$$

This reduces Equation 41-42 to Equation 44-45.

$$L = I_x \dot{p} + \frac{1}{2}qrI_z \quad (44)$$

$$M = I_y \dot{q} + \frac{1}{2}rpI_z \quad (45)$$

Due to the rapid spin of the disc (Hess, 1975), it can be supposed that there will be no angular acceleration during the angular motion if $\dot{p} \ll qr$ and $\dot{q} \ll rp$. Therefore, they can be rewritten as Equation 46-47.

$$q = \frac{2L}{rI_z} \quad (46)$$

$$p = -\frac{2M}{rI_z} \quad (47)$$

The equations that are presented here represents a unique feature of the gyroscopic precession which are available on the loading analysis of the disc wing such as the increase in the pitch value is observed caused by a positive value of the moment of rolling conditions for a spin rate with the positive value and rolling into the left side along with the wind-down condition occurred due to the positive value of the pitching moment. Also, it has been examined that for a symmetric disc the aerodynamic value of rolling moment shows a relatively lower value, and the precessional pitch rate also, shows a very negligible value. But the moment that occurred due to the pitching of the disc can show a relatively larger value which supports a significant roll rate. The tendency of a disc to roll in flight anecdotally is represented as the 'Turnover Effect' (Schuurmans, 1990).

3.1.5 Non-dimensional Roll Time:

It has also, been supposed that a disc wing with a non-dimensional trajectory with the identical initial parameters also, shows the identical behavior if the roll rate is also identical. For the present analysis, the non-dimensional time and non-dimensional distance are given by Equations 48-49.

$$\hat{t} = \frac{t g}{V_\infty} \quad (48)$$

$$l = \frac{l g}{V_\infty^2} \quad (49)$$

while t is dimensional time and l is dimensional length,

The non-dimensional disc roll rate is thus obtained as Equation 50.

$$\hat{p} = \frac{pV}{g} = -\frac{2MV_{\infty}}{rI_z g} \quad (50)$$

The disc pitching moment can be approximated as Equation 51 by assuming that M_o for the disc is zero.

$$M = -k_n C_{Lift} q_{\infty} S c \quad (51)$$

The mass moment of inertia I_z of the disc shows its dependency on the distribution of mass which is along the z-axis, to put the moment of inertia into context, it is useful to consider Equation 52.

$$I_z = m k_{zz}^2 \quad (52)$$

while k_{zz} is the radius of gyration,

Values of k_{zz} for various disc-wing shapes become larger when the weight is removed towards the circumference. Firstly, consider a circular cylinder with negligible height which has a radius of gyration $k_{zz} = (c/2)\sqrt{2} \sim 0.71(c/2)$. Secondly, as the mass is redistributed towards the circumference k_{zz} increases, a typical value for a Frisbee-like disc wing is $k_{zz} = 0.86(c/2)$ (Hubbard & Hummel, 2002). Lastly, for the theoretical case of a flying ring with the total mass distributed evenly at the outside radius $k_{zz} = 1(c/2)$.

In this study, it is proposed that the circular cylinder has a uniform surface along with a negligible height (Equation 53).

$$I_z = \frac{1}{8} m c^2 \quad (53)$$

Here the m represents the overall mass

Finally, the non-dimensional disc roll rate is written as Equation 54.

$$\hat{p} = \frac{16k_n C_{Lift} q_{\infty} S V_{\infty}}{m g r c} \quad (54)$$

Such as $Lift = Weight$, C_{Lift} is defined as Equation 55.

$$C_{Lift} = \frac{mg}{q_{\infty} S} \quad (55)$$

And it can be defined Equation 56.

$$AdvR = \frac{rc}{2V_{\infty}} \quad (56)$$

Equation 54 is simplified as Equation 57.

$$\hat{p} = \frac{8k_n}{AdvR} \quad (57)$$

The non-dimensional disc roll rate (Equation 57) defines that the non-dimensional rate of the roll for a disc shows a proportionality between the advance ratios and the ratio of a static margin if the flight is considered to be the non-acceleration and horizontal. Thus, roll rate is minimized when the aerodynamic center of the disc is closest to the center of the disc (minimum k_n) and when the disc is thrown at a specified trajectory with a higher value of the spin rate relevant to its velocity in the forward direction. Both of these conditions are consistent with the everyday experience of Frisbee throwing.

4. Computational Fluid Dynamics (CFD):

Computational Fluid Dynamics (CFD) is a methodology to solve fluid flow problems numerically. The open-source software OpenFOAM has been used as a numerical tool in the current thesis. The computational analysis for all cases carried out here is divided into three steps described as follows,

- Pre-processing: This step includes the basic setup for solving CFD problems and getting accurate computational results. This step includes the creation of the geometry and mesh and the verification of the latest independence on the results (mesh sensitivity analysis).
- Solution setup: the next step involves defining the necessary solver, number of iterations, and convergence criteria in order to perform the simulation.
- Post-processing: It is the final step that involves analyzing the results. It includes contours of different variables plots of numerical values, (Pressure and velocity contours, flow trajectories, etc.). It also involves the evaluation of results and comparison of simulation results with the experimental or theoretical results if possible (to verify the accuracy of the model).

4.1 Computational Setup:

This process involves Importing the geometry, geometry cleaning, and meshing. These parts are discussed below,

4.1.1 Geometry Cleaning:

This step involves importing the geometry and adding the required features for simulations

such as the fluid domain. It also involves combining the geometry as a whole part and avoiding the small features to reduce the chances of meshing and solution errors. Varying Disc Designs are used in this study to observe the aerodynamic performance of the discs. The 3D models of the discs are shown in figures below,



Figure 12: Aviar Disc Front View



Figure 13: ROC Disc Front View



Figure 14: Wraith Disc Front View

4.1.2 Meshing:

This step involves creating the mesh to carry out efficient simulations. This step is also, included in the pre-processing because it involves performing the mesh independence analysis on the designated model (adjust the number and size of elements to get the independence of the mesh on the results). As the mesh design is directly related to the solution, increasing the mesh efficiency or generating the finer mesh may provide more accurate results. Mesh sensitivity analysis involves obtaining the results at every mesh density while increasing it in order to gain independence.

4.1.3 Solution Setup:

The solution of the governing equations is carried out by two solvers (potentialFoam and simpleFoam) run in parallel as follows:

The potential Foam is a solver with many unique attributes used to solve fluid mechanics-related problems. This solver has the potential to care simple and complex problems related

to the potential in the fluid velocity (i.e., Φ), and the velocity fields to calculate the velocity potential is generated through reconstruction of the flux which also, could be obtained through the volumetric face flux field. Additionally, simpleFoam is a solver with steady-state conditions having the capability to solve the problems related to the flows with high Reynolds number or the incompressible flows and for obtaining the solution the simpleFoam uses the SIMPLE algorithm which is short for the semi-implicit method for the pressure linked equations.

4.1.4 Boundary Conditions:

The fluid in contact with the wall as a solid object (disc) has zero relative velocity which is called a no slip condition (Figure 15). As per the definition of the Reynolds number, having zero velocity leads to zero Reynolds number which means the flow near the wall is more affected by the viscous force therefore the mean velocity is the function of the ρ, μ, τ_w as the shear stress at the wall and y_d as the distance from the wall.

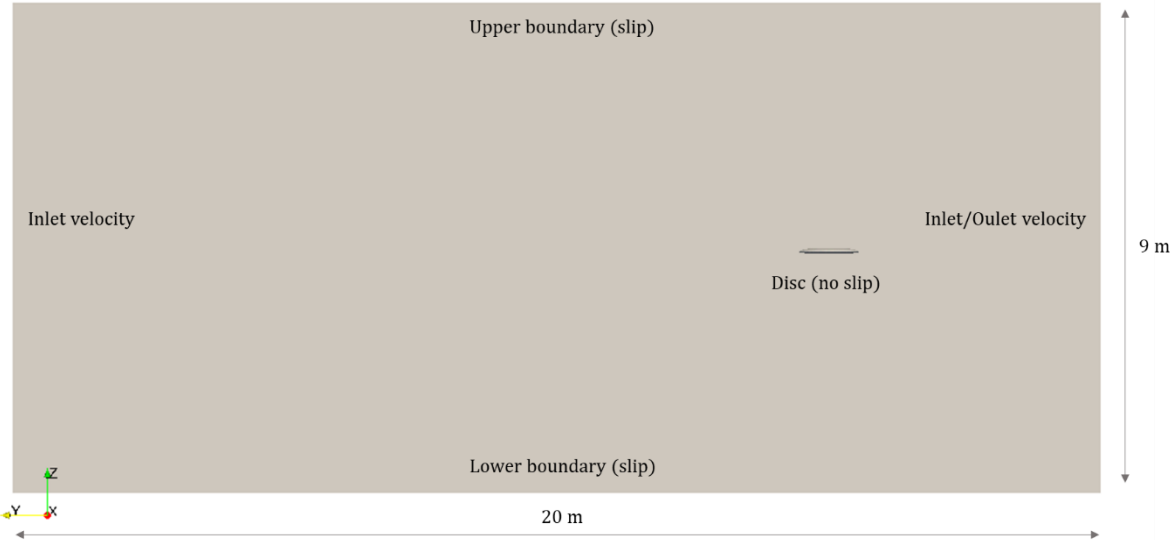


Figure 15: Schematic representation of the numerical domain – Boundary conditions.

As per the definition of the Reynolds number, having zero velocity leads to zero Reynolds number which means the flow near the wall is more affected by the viscous force therefore the mean velocity is the function of the ρ, μ, τ_w as the shear stress at the wall and y_d as the distance from the wall. Inlet velocity is fixed at $V_o = 27.5$ m/s which is also equivalent to the Reynolds number value of 3.78×10^5 .

4.1.5 RANS Model:

The RANS(Reynolds-Averaged Navier-Stokes) model is employed in this study to compute the

results presented in this study. To obtain the results for the flows with the higher value of the Reynolds number the equations governed are used in the form of an average to obtain the required results. Since this model has a unique methodology of joining the advantages of the RANS model with the large-eddy simulations (LES) methodology. In addition to that, the RANS $k - \omega$ is a model which has two extra equations which are employed to demonstrate the added properties of the Turbulent flows. In this model, the first transported variable represents the turbulent kinetic energy with the symbol 'k' and the second transported variable represents the specific dissipation with the symbol 'w'. The variable which shows the specific dissipation is also, used to find the turbulence scale. Another RANS $k - \omega$ SST (Shear-Stress Transport) model is turbulence model with two equations which are used to solve the two transport equations for the kinetic energy k and specific dissipation ω . This advanced formulation joins the good features in both the $k - \omega$ turbulent models formulation enables it to be used for all of the parts inside a boundary layer with the help of the viscous sub layer.

4.1.6 LES Model:

As it has been observed that the Reynolds Averaged Navier Stokes (RANS) is not completely successful in resolving the issues related to complex unsteady flows. Continuing this the major problems related to separated unsteady flows were not completely resolved even with the use of the latest developed turbulence models. That is the reason which urged the researchers to look for an alternative to resolve this issue. So, they paid close attention to the other models such as direct numerical simulations (DNS) along with the large-eddy simulations (LES). Also, when these models are employed, they seem to be using more computational power and making this an expensive investment; here, in this study, the use of a large-eddy simulations model is observed which doesn't seem to be so drastic.

The RANS model has proved its applications in many cases that is why it is employed in most of the issues related to turbulent flows but there is a drawback that holds this model from evaluating the features of quasi-periodic large-scale and turbulent chaotic small scale in the understudy flow field. This problem arises due to the RANS model of using the statistical approach towards the flow models which generates the velocity and pressure fields as a time-averaged function. This issue could cause problems in dealing with flows with complex bodies such as the bluff body. Generally, it has also, been observed that the RANS model is not able to generate the flow characteristics of the unsteady flow reasonably. This could result in the generation of the wrong evaluation of the unsteady phenomenon such as the flow behavior

generated behind the bluff or inclined bodies including vortex shedding etc.

Large-eddy simulations (LES) has a unique approach towards the unsteady flows such as LES uses the Navier stokes governing equations to solve the flow problems, it also, uses the filtering technique instead of the average time technique and it converts the stresses that emerge at high Reynold's numbers into the resolved stresses. LES model also, has some drawbacks such as it uses a very fine grid and uses the time step which is very fine to resolve the fluid flow problems. These characteristics also require high computational power which increases the cost in this sense as well.

A method that is used to simulate the air currents in the atmosphere is suggested by Joseph Smagorinsky (Smagorinsky, 1963) with the name of the LES comparison method. In this method, the interconnected solution is subtracted into two parts with the help of disaggregation. The structural models whose sizes are greater than the normal specified threshold size are designed differently than the smaller models. This method also has the capability to join the conventional method of turbulence modeling with the DNS of turbulence. The eddies simulations are taken into consideration directly while the simulations with a smaller domain are solved with the sub-grid scale (SGS) model of turbulence modeling. In it, Smagorinsky proposed that the higher value of the Reynolds number has the capability to transfer the energy effectively from the larger to smaller scales. This transfer of energy also contributes to the dissipation of energy but any transfer can be estimated. In addition to that, it was also suggested that for an inertial subrange where the energy is transferred larger energy-producing scale to the smaller energy dissipating scales conservatively which is also assumed to be related to the scales which are solved by the computational grid.

The LES method has the feature to resolve the complex large energy scales in direct order while skips the small scale variations in the turbulence.

As the turbulence models show the same behavior even in the applications in varying conditions. This nature of the turbulence model enables the use of universal turbulence models to use in multiple applications. There are some features of the LES model which correlate with the RANS model such as evaluating the unknown constants and terms the LES model also, uses the unique Navier stokes equation. This method of resolving the unknowns is known as the sub-grid scale stresses. The name of this term depicts its behavior to resolve these constants at a level smaller than the grid size. These all features come at the cost of the increased computational power which will be a necessity to resolve the unsteady flows and

the finer grid to compute as many details as possible.

4.1.7 DDES Model:

DDES is the model which is presented to tackle the problems related to the RANS and LES model. The DDES model takes the best out of them such as to solve the flow-related problems near the boundaries of the solids it uses the RANS algorithm of statistical turbulence such as the turbulence model of the Spalart-Allmaras (S-A) (Spalart PR, Allmaras PR; 1994). Also, it takes some other features from the RANS such as it uses the time-averaged fields for the velocity and pressure near the solid boundaries, and does not compute the vortices formation directly. As it is a hybrid model it takes the features from the LES model to compute the flows far from the solid boundaries such as the formation of the higher level of vortices structures and the generation of small-scale turbulent models with the help of the sub-grid-scale model. Also, the LES model is used to resolve the problems related to unsteady flows. These models work simultaneously but there is no specific division between their boundaries. This model is designed in a way to use the RANS model at the solid boundaries where the coarse mesh could also, give good computational results and the LES model at the region of unsteady flows or the area away from the boundary but for the LES to work properly finer mesh is required which certainly requires the more computational power as well. For the RANS model the finer mesh may not be a necessity it could give good results even with the use of low grid resolutions (Spalart PR, Wasistho B, Nikitin NV; 2000). Because of this amalgamation of both the models the DDES model has shown good results and could be used at varying numbers of applications even to resolve the problems related to the high Reynold's numbers. But the main area for the DDES model is the kind of flows where the RANS model does not show accurate results such as the unsteady flows along with the large separated regions. This model has also, shown some drawbacks discussed by Nikitin et al (Nikitin NV, 2000). Such as this model has shown values that were very much different from their classical values in the case of the channel flows but the computation shows the stable behavior even at the higher value of Reynold's number and with the coarse grid sizes. The researchers predicted that the divergence from the classical values could happen due to the less fine grid generation or due to the non-adjustment of the turbulence model (Spalart Allmaras model which was originally modeled for the RANS model only) (Spalart PR, Allmaras SR; 1994). This behavior of the DES model is studied and predicted that this model should work with the RANS model only while using the

unseparated flows fields (Travin A, Shur M; 1999).

Both the RANS and LES models have shown good benefits in resolving the multiple issues related to turbulent flow fields. As the LES model in which a very sensitive and finer grid generation is required on the entire flow, the field makes it very expensive in the sense of computational power. But it could be made feasible and less expensive if less fine mesh could be employed near the boundaries. The RANS model comes in handy to resolve this problem and is used alongside the LES model and called the hybrid RANS-LES model. The detached eddy simulations (DES) model is a hybrid form of RANS & LES models where it uses the RANS algorithm at the boundary and the LES model for the flow field away from the boundaries. That is the reason this model becomes popular in many applications as it provides good accuracy at a very less computational power than the LES model.

Computational fluid dynamics technique has many applications in various fields but for Industrial applications, the hybrid RANS/LES models have shown promising results where both the models are used at their specific regions LES away from the boundary and RANS alongside the solid boundaries. Detached eddy simulation is also, considered in the hybrid models category. The method is proposed in 1997 by Spalart et al. and after that, it has been employed in various applications and has also, undergone various revisions as well. Menter and Kuntz (2002) also, worked on the same model and proposed that while the switching of RANS to the Eddy simulations the resolved turbulent model was unable to create balance with the reduction in eddy viscosity. That could be the reason for the occurrence of artificial Grid Induced Separation (GIS). This effect is called the MSD (Modeled Stress Depletion). Also, while moving towards the end point the bending function of the $k-\omega$ model is employed as the barrier to stop the model from moving towards the eddy simulations in the areas closer to the solid boundaries. Due to this Spalart et al. (2006) introduced a new generic formulation that can be used with any RANS model and termed as the Delayed DES or DDES. This method is further improved depending upon the applications of use and In this study, it has been used to obtain effective solutions and is presented in this study as well.

4.2 Modeling Approaches:

4.2.1 DDES and RANS:

For the numerical formulation of these models, a general incompressible fluid model is taken along with the general fluid properties which shows the constant values. The conservation of

the mass and the conservation of momentum equations were used along with the Navier Stokes equation. Both the LES and RANS equations are modeled in a hybrid form such as an updated derivation of Navier stokes equation is used with the filtered width Δ to create a difference between the higher and lower Reynold number flows in case of LES and the same constants were used to formulate the RANS model by creating a time-averaged formulation to support the RANS model. Then the hybrid form can be presented in the same form which is dimensionless,

$$\frac{\partial \bar{u}_i}{\partial x_i} = 0 \quad (58)$$

$$\frac{\partial \bar{u}_i}{\partial t} + \frac{\partial (\bar{u}_i \bar{u}_j)}{\partial x_j} = -\frac{\partial \bar{p}}{\partial x_i} - \frac{1}{Re} \frac{\partial \tau_{ij}^{mol}}{\partial x_j} - \frac{\partial \tau_{ij}^{turb}}{\partial x_j} \quad (59)$$

$$\tau_{ij}^{mol} = -2\nu \bar{S}_{ij} \quad \text{where} \quad \bar{S}_{ij} = \frac{1}{2} \left(\frac{\partial \bar{u}_i}{\partial x_j} + \frac{\partial \bar{u}_j}{\partial x_i} \right) \quad (60)$$

where u_i , p and $\nu = \mu (\rho = 1)$ are used as the constants to represent the velocity, pressure the viscosity of the flow respectively. Also, both the models use the overbar ($\bar{\cdot}$) to represent the values such as in LES it is used to represent the resolved values and in the RANS model, it is employed to show the components which are taken in time-averaged form. Re represent Reynold's numbers. Whereas the value τ_{ij}^{mol} is used to show the transport of molecular momentum shown in Equation (60). There are some terms in this unique formulation which has been employed by both the models such as the constant τ_{ij}^{turb} is employed in the RANS model to represent the stress tensor due to the Reynolds numbers over the entire flow field which is taken on the average scale and it is also used to transfer the momentum due to the high Reynold number flows. In the LES model, it is used to represent the sub-grid-scale stress tensor for the areas of the resolved turbulent flows and the unresolved areas of the small-scale regions. This constant has an important integration in both the models and has to be adjusted carefully. The numerical modeling for the RANS and the DDES model is discussed but for LES only a brief description is provided but it is discussed in detail in other available studies (Breuer M, Rodi W, 1996; Breuer 1998).

As the DDES is a unique model to use the divided flow domain for computation. This method is very useful to employ the different techniques in the same model such as the RANS approach for the near-wall boundaries and the Navier stokes equation in the LES model which has been filtered for its computation. The Spalart Allmaras model is used in both the techniques as the turbulence model to solve the fluid flows (Spalart PR, Allmaras SR, 1994). This is a model which uses the eddy viscosity ν_T along with the strain rate tensor $\overline{S_{ij}}$ to compute the stress constant τ_{ij}^{turb} and it uses the approximation of Boussinesq for this formulation (Equation 60). The formulation is briefly described as,

$$\tau_{ij}^{turb,a} = \tau_{ij}^{turb} - \delta_{ij}\tau_{kk}^{turb}/3 = -2\nu_T\overline{S_{ij}} \quad (61)$$

where $\tau_{ij}^{turb,a}$, τ_{ij}^{turb} , δ_{ij} are the constants used in Equation 61 to represent the stress tensor and Kronecker delta respectively. The new value of the pressure is also, computed as $P = \bar{p} - \delta_{ij}\tau_{kk}^{turb}/3$ where the same stress tensor is used to compute its value.

ν_T which represents the eddy viscosity is computed by using the separate formulation. The formulation also uses the turbulence model of the Spalart Allamars to compute the value of eddy viscosity presented as $\tilde{\nu}$ in the following equation,

$$\frac{\partial \tilde{\nu}}{\partial t} + u_i \frac{\partial \tilde{\nu}}{\partial x_i} = c_{b1}\tilde{S}_\nu\tilde{\nu} + \frac{1}{\sigma}\{\nabla \cdot [(\nu + \tilde{\nu})\nabla \tilde{\nu}] + c_{b2}(\nabla \tilde{\nu})^2\} - c_{wl}f_w \left[\frac{\tilde{\nu}}{d}\right]^2 \quad (62)$$

This equation is usually seen as the two parts the left and the right part as both of them show some unique separate features. Such as the left part depicts the variations that occurred in the variable $\tilde{\nu}$ while the other side represents multiple terms including diffusion, destruction, and production terms. Also, the constant \tilde{S}_ν and $|\omega|$ represents the scalar dimensionless quantity in the first term (production term) and the vorticity magnitude respectively. The formulation for such terms is expressed as follows,

$$\nu_T = \tilde{\nu}f_{v1}, \tilde{S}_\nu \equiv S_\nu + \frac{\tilde{\nu}}{k^2 d^2}f_{v2}, S_\nu = |\omega|, x \equiv \frac{\tilde{\nu}}{\nu} \quad (63)$$

$$f_{v1} = \frac{x^3}{x^3 + c_{v1}^3}, f_{v2} = 1 - \frac{x}{1 + xf_{v1}}, f_w = g \left[\frac{1 + c_{w3}^6}{g^6 + c_{w3}^6} \right] \quad (64)$$

$$g = r + c_{w2}(r^6 - r), r \equiv \frac{\tilde{\nu}}{\tilde{S}_\nu k^2 d^2} \quad (65)$$

The other constant terms are expressed as $k=0:41$, $\sigma=2/3$, $c_{b1}=0:1355$, $c_{b2}=0:622$, $c_{v1}=7:1$, $c_{w1}=c_{b1}/k^2+(1+c_{b2})/\sigma$, $c_{w2}=0:3$ and $c_{w3}=2$. The technique proposed by the Smagorinsky (Smagorinsky J., 1963) is proved to be useful while using the same Spalart Allmaras model but with the same modification of adding the variable \tilde{d} which is taken as the proportional value to the filtered width of Δ with the wall distance d in the Equations (62), (63), and (65). The resulting equation is shown below,

$$\tilde{d} = \min(d, C_{DES} \cdot \Delta) \quad \text{with} \quad \Delta \equiv \max(\Delta_x, \Delta_y, \Delta_z) \quad (66)$$

Then this formulation becomes the uniform model of the detached eddy simulations model. The value of the $C_{DES}=0:65$ is the value that is preferred but it is a variable term and can be adjusted for the structured meshes. Such as if the fine grid could be achieved which can tackle the large vortices in the region away from the solid boundaries, then Equation (62) will be employed as the SGS model. This condition will be checked by the value of the $d > \Delta$. While, if the large-eddy simulations (LES) model is applied which requires the finer grid throughout the fluid domain then this approach is not preferred to be used in the regions with higher Reynold's number values. That is why the RANS model is used for $d < \Delta$ and \tilde{d} is to be computed in a regular manner from ($\tilde{d} = d$). As both, models possess different spatial features and if LES is employed directly to resolve the unsteady flow domains it would require a very high computational power due to its complexity. That is why the combined RANS and LES model is used to save the computational power as well.

4.2.2 LES:

The Large-eddy simulations model has also faced problems related to the closure such as in the RANS model. That is why it has been observed that the turbulence model can be formed to cover all the aspects of the fluid flows. That is the reason a rather simple formulation is generated based upon Smagorinsky's model (Smagorinsky J., 1963) which is presented here in Equation 67. This is obtained with the help of the Boussinesq's approximation where the sub-

grid length l along with the strain rate constant $\overline{S_{ij}}$ is used to evaluate the turbulent viscosity ν_T ,

$$\nu_T = l^2 |\overline{S_{ij}}| \quad \text{with} \quad l = C_s \Delta \left[1 - \exp\left(\frac{-y^+}{A^+}\right)^3 \right]^{0.5} \quad (67)$$

$$\Delta = (\Delta_x \cdot \Delta_y \cdot \Delta_z)^{1/3}, y^+ = \frac{y u_\tau}{\nu}, u_\tau = \sqrt{\frac{\tau_w}{\rho}} \quad \text{and} \quad A^+ = 25$$

C_s is a famous constant called the Smagorinsky constant. This constant shows the property of being used as a constant value over the full domain or it can also be computed as a function of space and time which was predicted in a research study (Germano M, 1991) and many other researchers worked on the improvement of the function (Lilly DK., 1992). There were many variations such as in equation 67 the damping function is used to observe the decrease in the value of the sub-grid length. In this study, the constant value of $C_s=0.1$ is used which is taken from Smagorinsky's model. In addition to that, the use of other models can have an impact depending upon the value of Reynold's numbers (Breuer M., 1998).

5. Numerical Results:

5.1 Mesh Sensitivity

Five density meshes were prosed to study the mesh dependency of the results:

Mesh 0: equivalent to 1061452 cells;

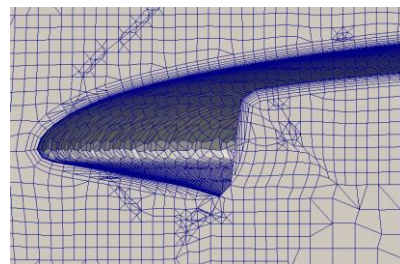
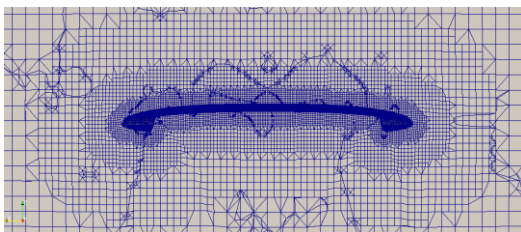
Mesh 1: equivalent to 3001629 cells;

Mesh 2: equivalent to 6609951 cells;

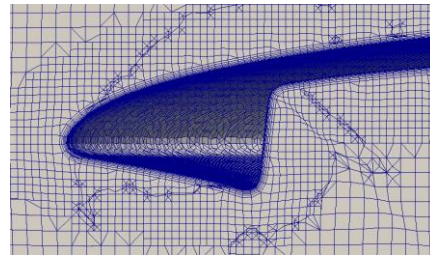
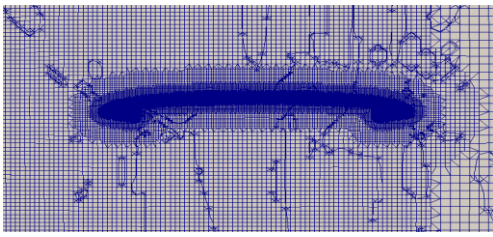
Mesh 3: equivalent to 11893763 cells;

Mesh 4: equivalent to 16556777 cells.

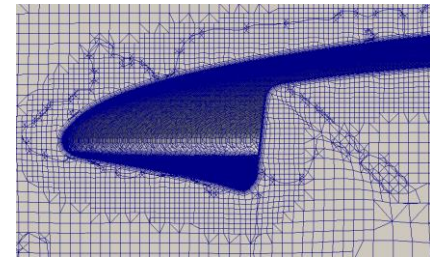
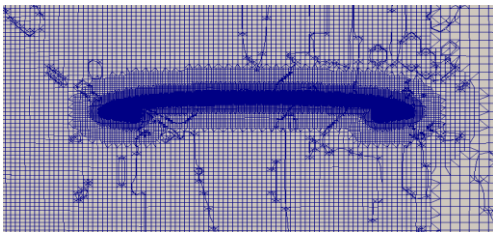
The resulting meshes from the different mesh densities are displayed in Figure 16.



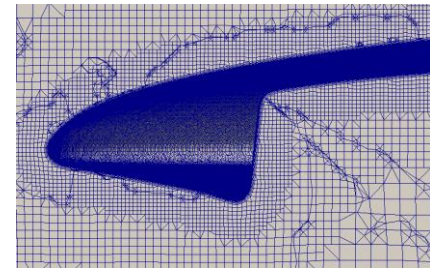
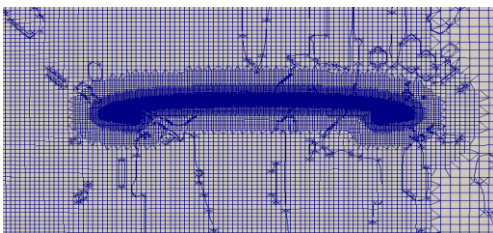
(a) Mesh 0



(b) Mesh 1



(c) Mesh 2

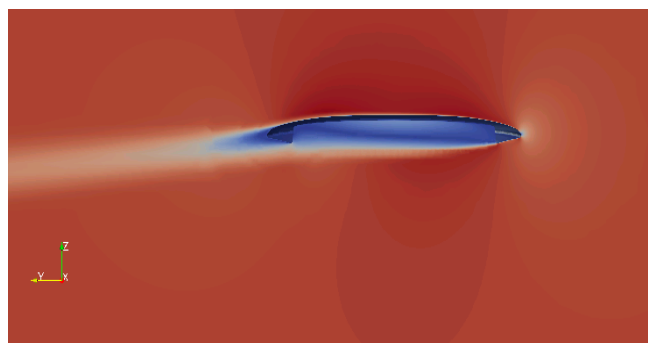
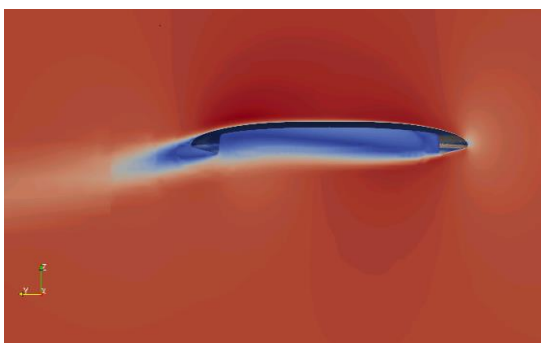


(d) Mesh 3

Figure 16: Geometry meshes resulting from the different mesh densities.

The steady-state RANS simulations ran for 2000 iterations. All simulations converged as the residuals were reduced by several orders and C_d , C_L , and C_M were typically stable to the third decimal place.

The results show that mesh does not have a great impact on the velocity contour.



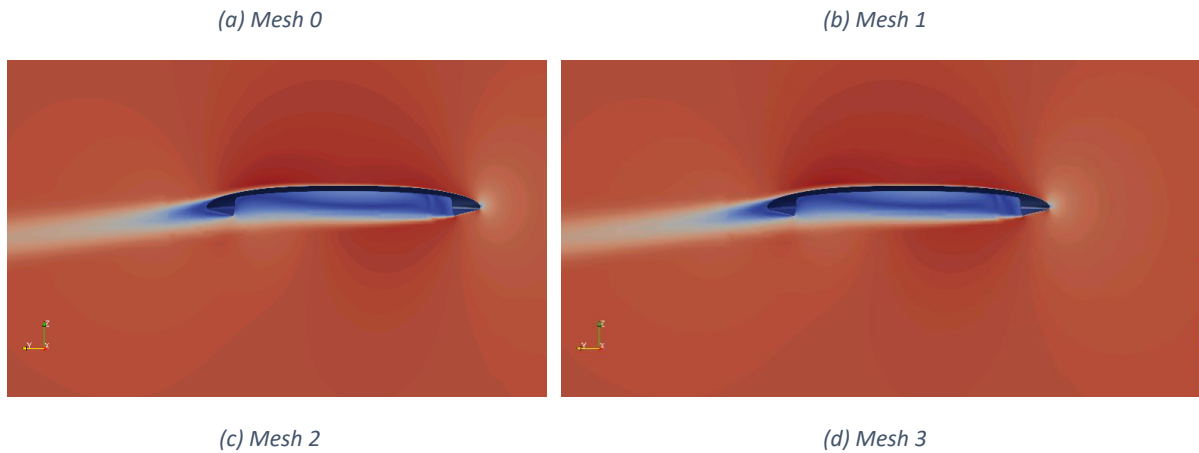


Figure 17: Velocity contour for the different mesh densities.

To evaluate mesh quality, the correlation y^+ is used. The correction which has been employed helps to determine the mesh distance on the cells available along the wall which is compared with the behavior of the fluid and it further helps to locate the center of a first cell with respect to the thickness of the wall. Also, it helps to find the accuracy of the simulations as well because if the center of the very first cell after the boundary layer is in the viscous layer, then the mesh is considered to be accurate. Therefore, it is usually considered that a y^+ smaller than 4 and ideally a y^+ smaller than 1 on all the surfaces. Also, the value of the y^+ (first cell distance) should be in accordance with the type of turbulence model used because it varies with the turbulence model types such as it should be between 30 to the 60 for the k epsilon model and it should be less than 1 for the k omega SST RAS model.

Using the function `simpleFoam -post-process -func yPlus`, the resulting close layers to the disc (y^+) were obtained for all mesh densities proposed earlier and resumed in the below table,

Table 1: Results of y^+ , C_d , C_L , and C_M for all mesh densities.

Mesh	y^+ (min)	y^+ (max)	y^+ (average)	C_d	C_L	C_M
0	6,29E-02	1,02E+02	3,31E+00	4,86E-02	1,30E-01	-2,94E-02
1	2,00E-02	4,68E+00	1,39E+00	4,80E-02	1,29E-02	-2,93E-02
2	2,69E-02	3,51E+00	1,12E+00	4,62E-02	1,23E-01	-2,83E-02
3	1,52E-02	3,40E+01	1,05E+00	4,54E-02	1,23E-01	-2,70E-02
4	1,31E-02	3,10E+01	9,82E-01	4,54E-02	1,23E-01	-2,70E-02

It is showed that mesh density has a great influence on the resulting coefficients (C_d , C_L and C_M) for coarser meshes. Finer meshes may have a better resolution compared to coarser ones.

Independency of the mesh size is found in Mesh 3 and Mesh 4 where aerodynamic coefficients were not sensitive to mesh density. However, in order to optimize simulation time, Mesh 3 (11893763 cells) is retained for all further studies.

5.2 Model Validation:

A first, a mesh sensitivity analysis is done to get the desired quality for mesh and to get the required mesh independence using the geometry displayed in Figure 18. Then, the results from the proposed numerical model were compared to experimental work conducted by Potts (Potts et Crowther 2002) to validate the accuracy of the tool.



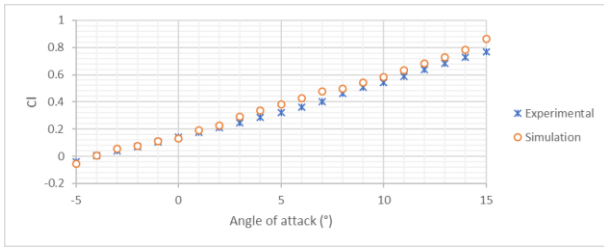
(a) Frontal view.



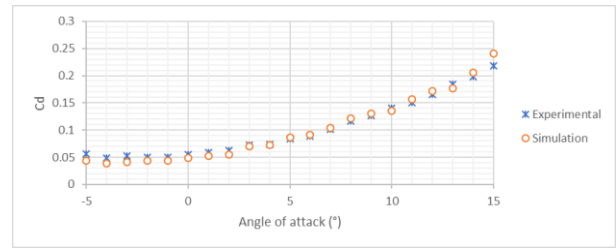
(a) Cross-section.

Figure 18: Disc Geometry – Wraith

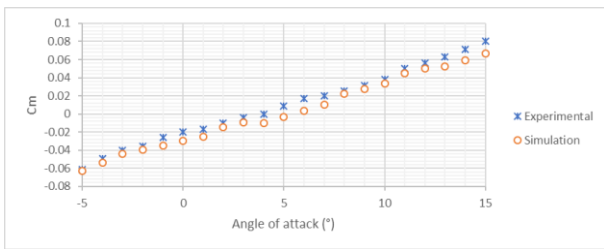
As mentioned earlier, the results from the proposed numerical model were compared to experimental work conducted by Potts (Potts et Crowther 2002) to validate the accuracy of the tool. Values of C_d , C_L and C_M were evaluated for different AoA from -5° to 15° (Figure 19).



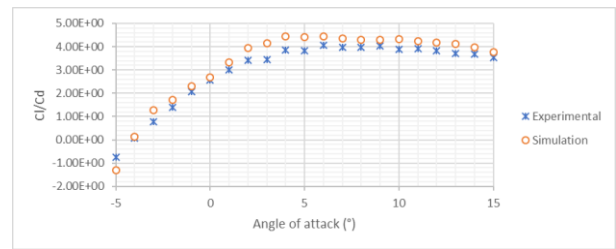
(a) C_d as a function of the AoA.



(b) C_L as a function of the AoA



(c) C_M as a function of the AoA



(d) C_L/C_d as a function of the AoA

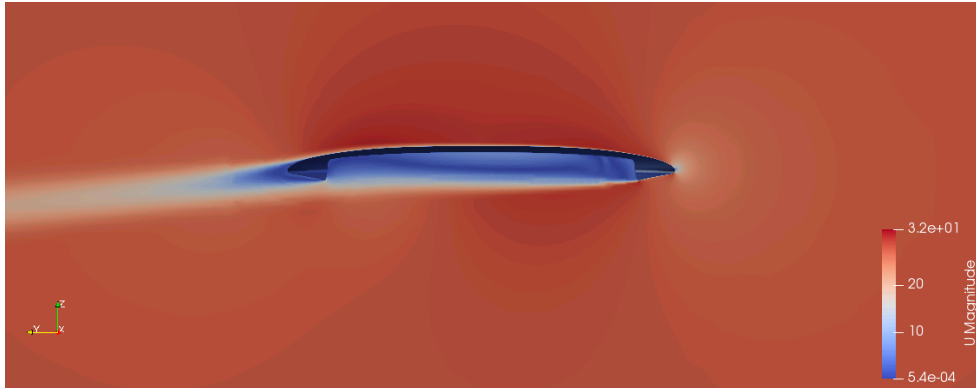
Figure 19. Experimental validation – Numerical vs Experimental values.

Prediction of aerodynamic coefficients compared to experimental data are qualitatively similar for all AoA, however, there is some deviation comparing to the experimental data. From the results, it can be concluded that (Figure 19):

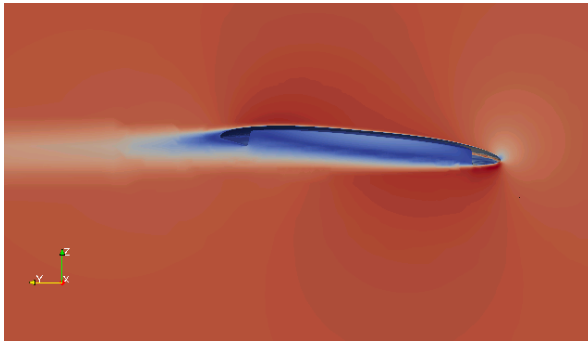
- As it can be observed that the geometrical findings align with the values of the experimental measures (< 15% of relative difference) even though there are some differences when the attack angle is 15° (~ 70% of relative difference).
- As expected, numerical estimations are closer to the experimental results at lower AoA where separation and reattachment are less predominant.
- These differences can be explained on one hand by the uncertainties in the measures and on the other hand by numerical modeling assumptions, i.e. CAD production (3D scan), they may generate some geometry imperfections.
- However, despite the differences, it can be concluded that the proposed CFD model is capable to compute disc aerodynamics with good accuracy.

5.3 Flow Topology:

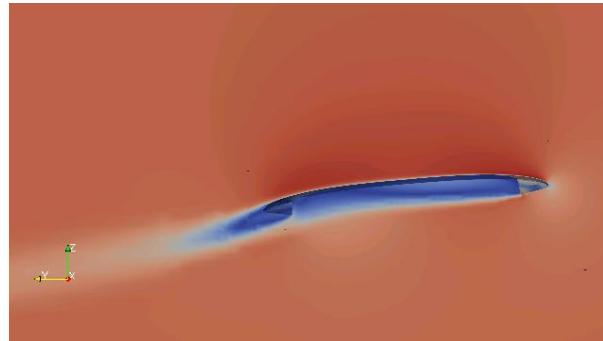
The AoA may have a great impact on the velocity contour (Figure 20),



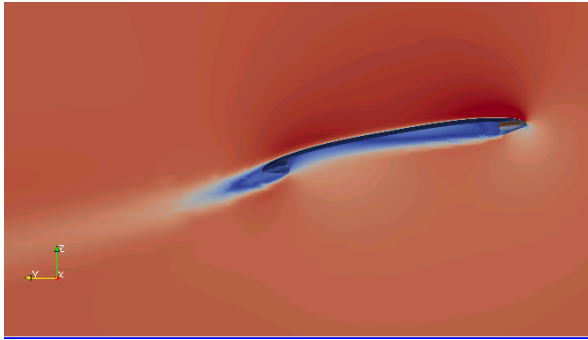
(a) AoA = 0°



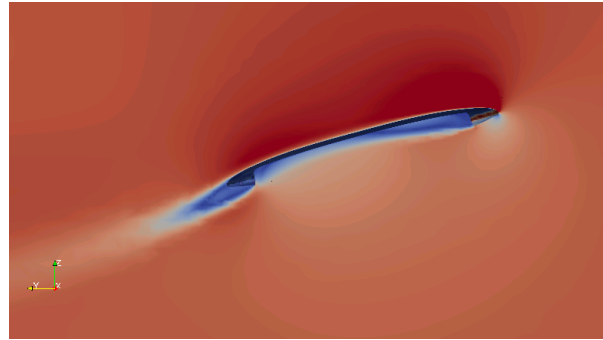
(b) AoA = -5°



(c) AoA = 5°



(d) AoA = 10°

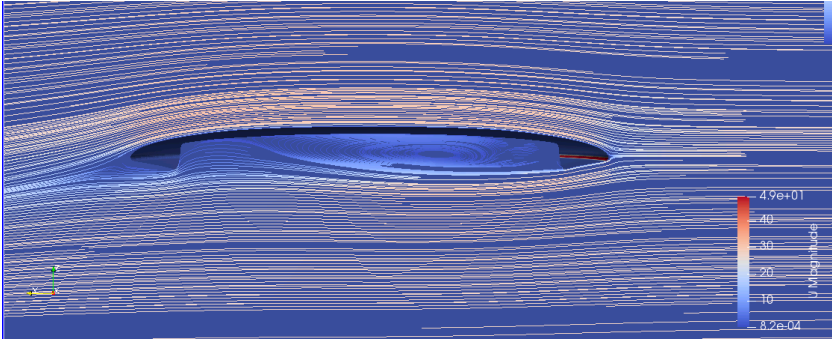


(e) AoA = 15°

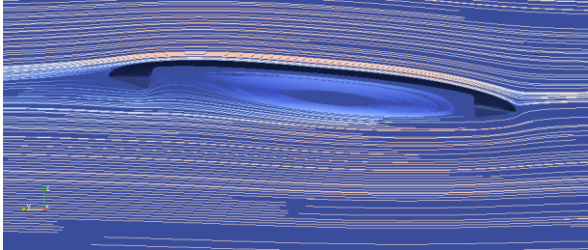
Figure 20. Velocity contour for different AoA.

Figure 20 shows the flow visualization over a non-rotating disc (Wraith) for different AoA. With flow from right to left, first of all, note the upwash ahead of the leading edge, then the boundary layer separates off the upper surface reattaching shortly thereafter creating a recirculating bubble. Further downstream the reattached boundary layer separates from the

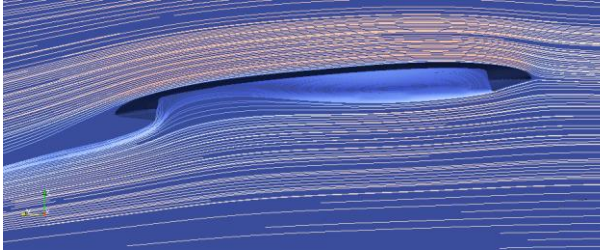
upper surface on the trailing edge, this separated shear layer contributes to the wake which has a downwash angle slightly greater than the AoA. Also, it can be observed that due to the cavity in the body the shear layer shows some separation from the front lip is reattached to the inner side of the trailing edge, and the reverse flow occurs under the shear layer toward the front edge. The fluid flowing in the front edge of the cavity (reverse flow) is restricted by the stagnant air pockets in the leeward wind on the front edge and cannot flow further forward. This stagnant air at the leading edge is represented by a weakly moving arrow. The linear stagnation line in the paint pattern on the surface of the cavity marks the boundary between the reverse flow and stagnant air in the cavity. This boundary is shown as a dividing line in the topology map. The falling of the vortices in the wake region is obtained due to the separated boundary layer at the trailing edge,



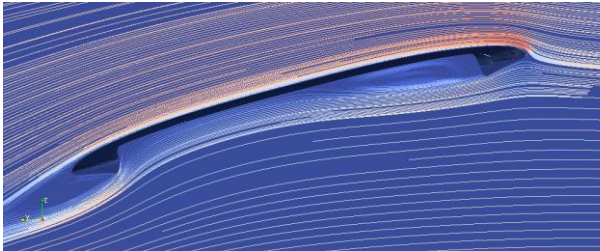
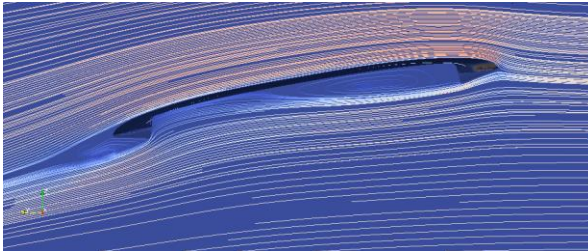
(a) AoA = 0°



(b) AoA = -5°



(c) AoA = 5°



(d) $AoA = 10^\circ$

(e) $AoA = 15^\circ$

Figure 21. Velocity streamline plots for different AoA.

The two-dimensional central flow cross-sections for a range of AoA are shown in Figure 21, flow from right to left. At 0° AoA the separation bubble is small, the shear layer beneath the disc covers the entire cavity. The reversed flow above the cavity shear layer occurs centrally for almost the entire length of the cavity. The leading-edge rim forces the central reversed flow to split, deflected towards the wingtips. This deflection provided the rotation to generate two stagnation points on either side of the mid-span, these spiral nodes were visualized in the surface paint patterns. Separation occurs on the trailing edge which has the ability to influence the wake region of the bluff body.

With increased AoA the separation bubble on the upper surface becomes enlarged, reattachment occurs further downstream. Also, the shear layer separating off the leading-edge lip attaches further upstream, and the wake downwash angle increases. At 10° AoA the separation bubble enlarges slightly (Figure 21c and Figure 21d), the shear layer beneath the disc still covers the entire cavity. The reversed flow above the cavity shear layer occurs centrally for only half the length of the cavity, as the dead air pocket grows larger.

At 15° AoA the upper surface separation bubble enlarges further (Figure 21e), as the reattachment line moves further downstream. The cavity shear layer now reattaches at the half chord position, a recirculating bubble is enclosed beneath the shear layer, downstream from the dead air pocket. Within the cavity, the reattached boundary layer remains attached throughout the inside of the trailing edge rim, separating off the lip.

The three-dimensional flow topology at 10° AoA is shown in Figure 22 and depicts the structure of the separation bubble and trailing vortices, flow from right to left.

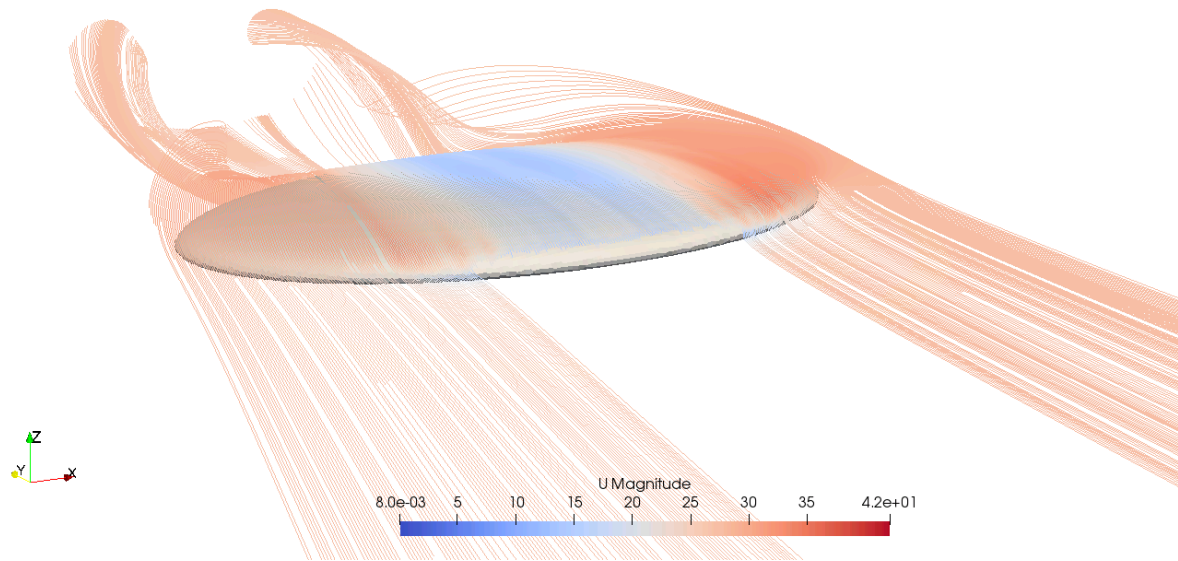


Figure 22. Streamlines – Counter-rotating vortex.

The separation bubble forms a crescent-like shape, the arced separation and reattachment lines are clearly marked. The arrows show the direction of the separated shear layer flow. Three cross-sectional slices through the structure show the recirculation/roll-up of fluid within the bubble. The vortex rotation is in the conventional sense for a typical wing section at positive AoA, the vortex trailing from the port wing-tip has clockwise rotation (when viewed from downstream) whereas the starboard trailing vortex rotates counterclockwise. Note the entrainment of fluid into the vortices from the upper surface boundary layer and also from within the cavity.

It is shown the downwash generated in the wake of the disc. The strong central downwash and the form of the trailing vortices become apparent with increased AoA from 0° through 10° . The wake cross-section at one chord length downstream of the disc trailing edge. Unsteady bluff body wake at 0° AoA. The structure of the trailing vortices has begun to develop at 5° AoA, the turbulence generated by the bluff body still visible. Note the close vicinity of the trailing vortex pair due to the low aspect ratio, as the AoA increases the central downwash develops and stronger rotation is given to the trailing vortices. At 10° AoA, the vortex structures are more clearly defined. The comparison of these two methods of illumination enables the reader to better understand how the wake cross-sections relate to the disc-wing model.

The bluff body wake, downwash, and trailing vortex structures downstream of a non-spinning disc wing are shown in Figure 23, for an AoA of 10°.

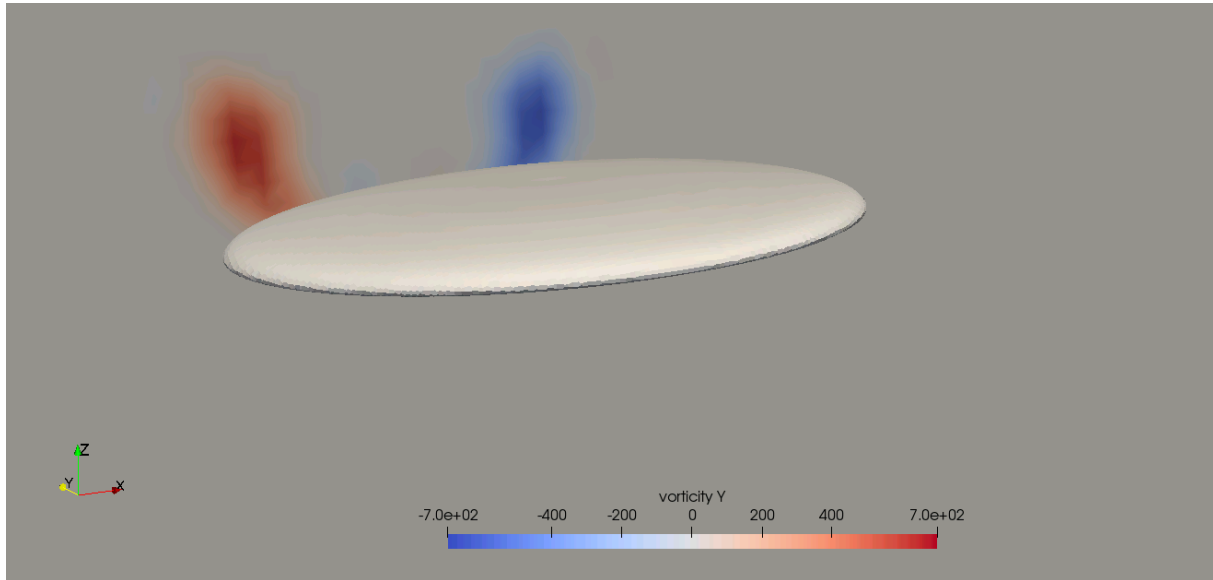


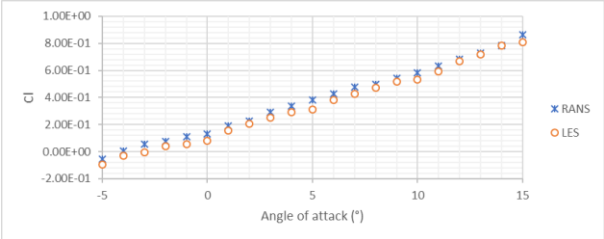
Figure 23. Vorticity - Counter-rotating vortex.

The bluff body wake, downwash, and trailing vortex structures extending downstream from a non-spinning disc wing are shown in Figure 23. Note the symmetry in the wake. The trailing vortices become more clearly defined with increased AoA. It can seem a transitional stage of trailing vortex development, the bluff body wake is still evident but the trailing vortices begin to take shape. The trailing vortex pair is established at 10° AoA. The inboard edge of the trailing vortices is clearly defined symmetrically. The strong central downwash exists between these two lines with the trailing vortices on either side. Cross-sectional slices through the wake at a range of positions downstream of a non-spinning disc-wing at 10° AoA showed in Figure 23 illustrates turbulence at the trailing edge and the curvature on either side of the disc indicates central downwash.

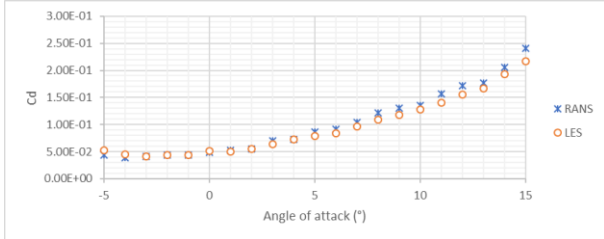
5.4 RANS/LES Comparison:

A method that is used to simulate the air currents in the atmosphere is suggested by Joseph Smagorinsky (Smagorinsky, 1963) with the name of the LES comparison method. In this method, the interconnected solution is subtracted into two parts with the help of disaggregation. The structural models whose sizes are greater than the normal specified threshold size are designed differently than the smaller models. This method also has the

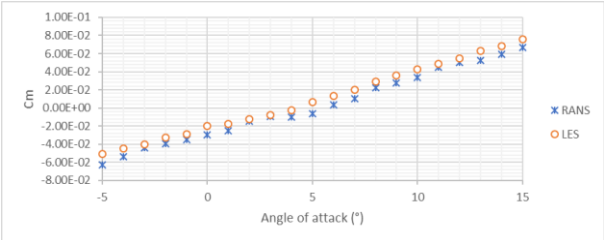
capability to join the conventional method of turbulence modeling with the DNS of turbulence. The eddies simulations are taken into consideration directly while the simulations with a smaller domain are solved with the sub-grid scale (SGS) model of turbulence modeling. In it, Smagorinsky proposed that the higher value of the Reynolds number has the capability to transfer the energy effectively from the larger to smaller scales. This transfer of energy also contributes to the dissipation of energy but any transfer can be estimated. In addition to that, it was also suggested that for an inertial subrange where the energy is transferred larger energy-producing scale to the smaller energy dissipating scales conservatively which is also assumed to be related to the scales which are solved by the computational grid. To better understand the differences between RANS and LES, transient Large Eddy Simulation (LES) using the Smagorinsky approach are also conducted and the results are compared to the steady-state RANS (Figure 24).



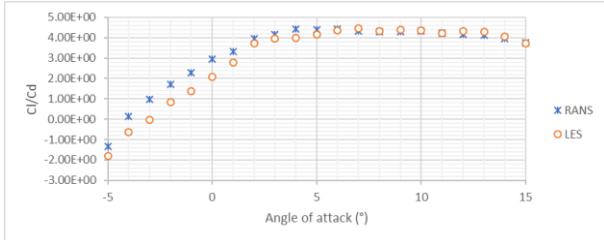
(a) C_d as a function of the AoA.



(b) C_L as a function of the AoA



(c) C_M as a function of the AoA

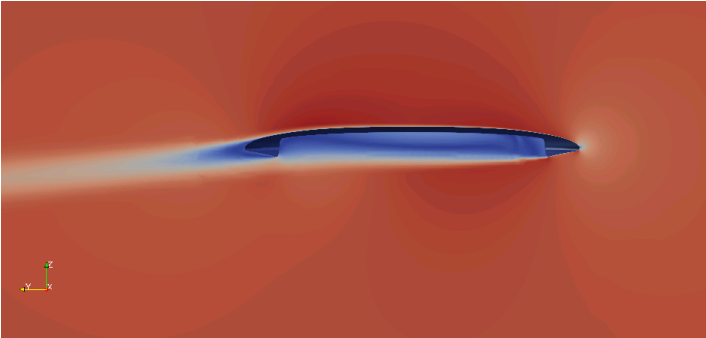


(d) C_L/C_d as a function of the AoA

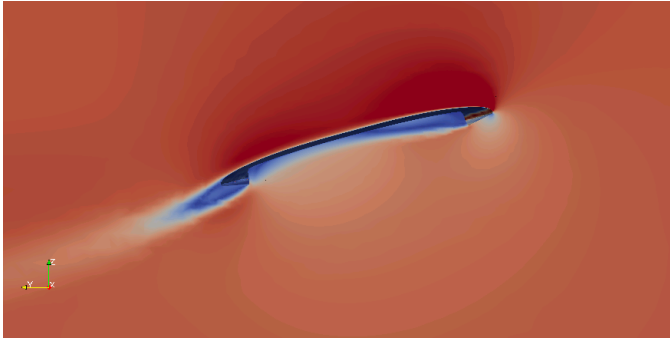
Figure 24. RANS and LES comparison.

However, comparing both models, there are quantitatively similar within a relative difference of around 25% (Figure 24). Also, the RANS model only has the capability to resolve the mean value of the velocity field which is averaged because this method is based upon the averaging of the time technique. The field of the velocity is also, averaged over a period of time which

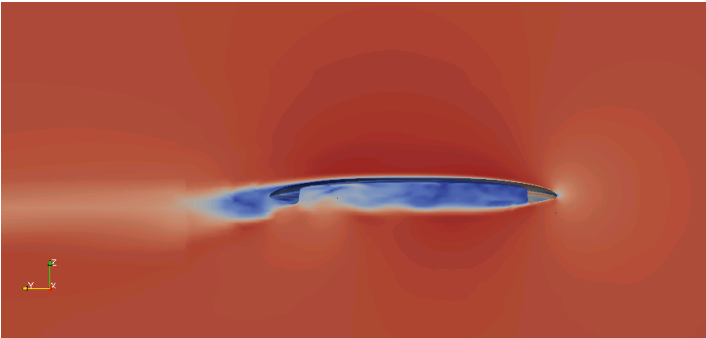
shows a considerably higher value than the constant of time with the variations in velocity. In addition to that, the time dependency of a constant mean velocity with a constant value can be monitored. On the other hand, the LES model is dependent on the filtering of the values rather than taking the average of them. LES may present a better description of the turbulent than RANS.



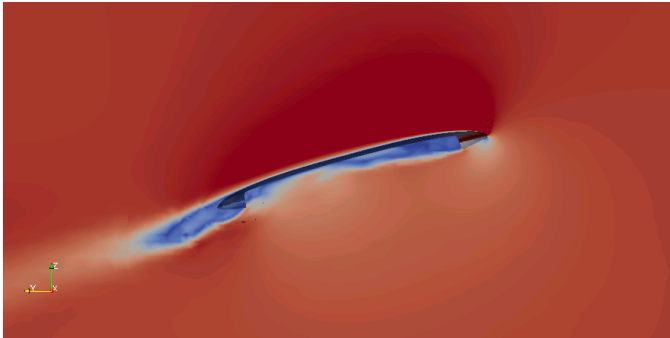
(a) RANS - AoA = 0°.



(b) RANS - AoA = 15°.



(c) LES - AoA = 0°.



(d) LES - AoA = 0°.

Figure 25. Velocity contour - RANS and LES comparison.

The local filtering of the values is carried out in the LES model which will make the unsteady equation but the RANS model generates the steady equation which is caused by the statistical averaging of this method (Figure 25). As it seems, LES is better at capturing a small length scale than RANS.

5.5 Other disc Geometries:

There are three major classifications of the golf discs which are dependent upon their varying values of the flight parameters. These are ‘driver’, ‘midrange’, and ‘putter’ discs (Figure 26).

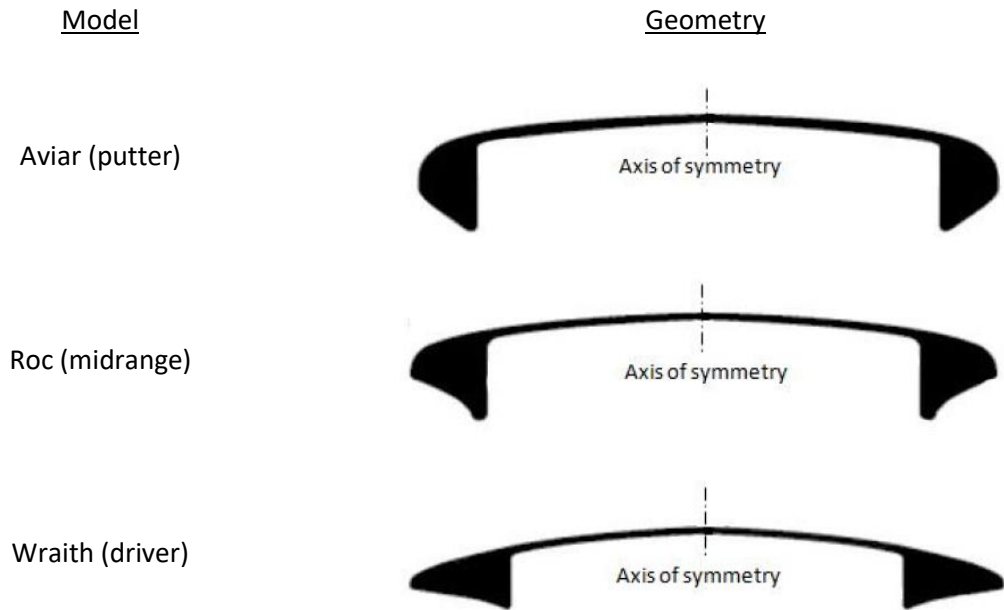


Figure 26: Different disc geometries.

The disc's names are decided in a way to represent the flight range of that disc as well and the range is considered horizontally for these characteristics which also represents the range of discs a word which is used especially in this thesis again and again. The classification of the disc is as follows: A disc with a range of 75m is called the driver disc, a disc with a range less than 50m is called the putter disc, a disc with an intermediate-range between 75m and 50m is called as the mid-range discs. The different ranges and parameters of these discs are dependent upon their geometrical structures which may vary in cambers, curvatures, depth to diameter ratios, etc.

5.5.1 Putter disc:

The putter geometry is illustrated in Figure 27.



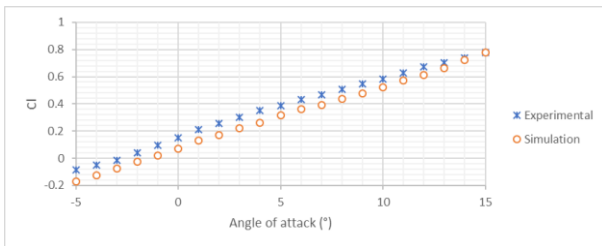
(a) Frontal view.



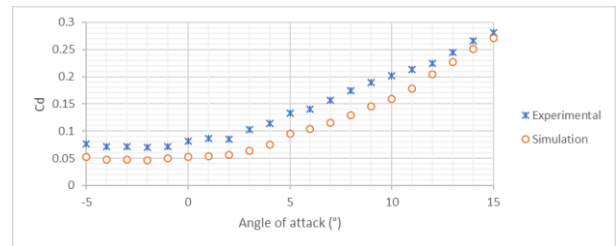
(b) Cross-section.

Figure 27. Disc geometry – Aviar.

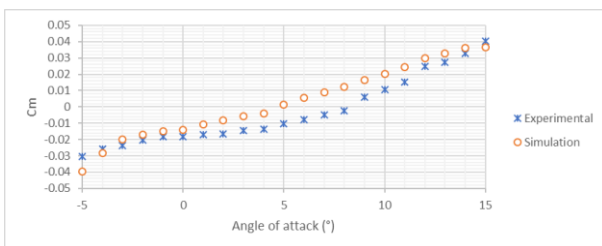
The results from the proposed numerical model using mentioned above geometry were compared to experimental work conducted by Potts (Potts et Crowther 2002) to validate the accuracy of the tool. Values of C_d , C_L and C_M were evaluated for different AoA from -5° to 15° (Figure 28).



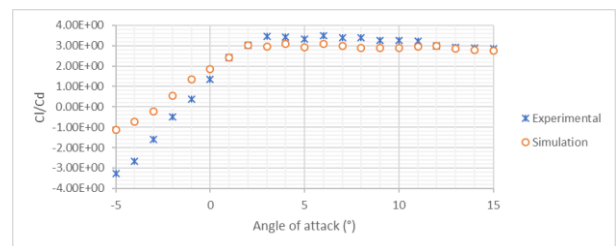
(a) C_d as a function of the AoA.



(b) C_L as a function of the AoA



(c) C_M as a function of the AoA

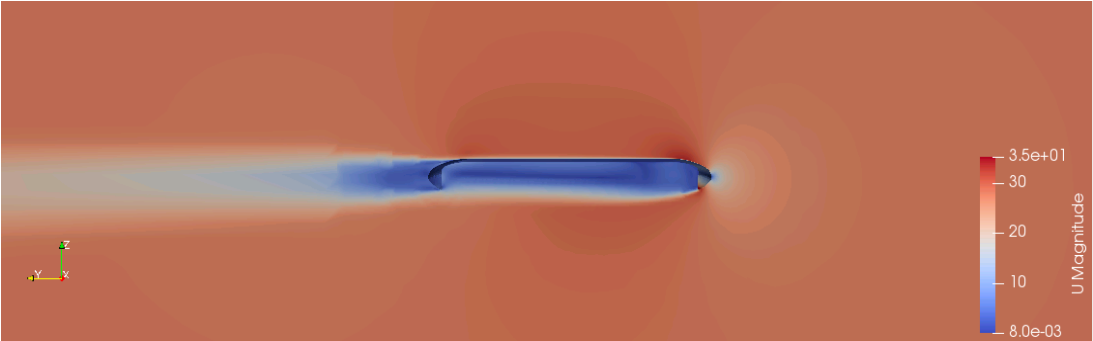


(d) C_L/C_d as a function of the AoA

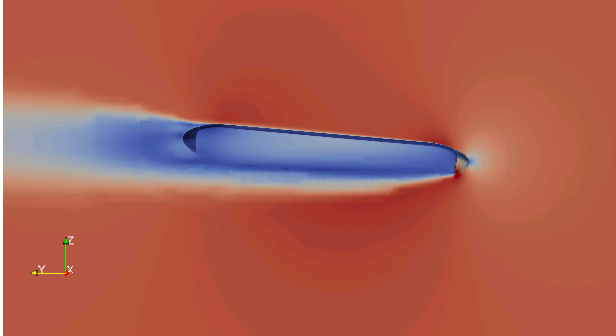
Figure 28. Experimental validation – Numerical vs Experimental values.

The results are qualitatively similar (same behavior), however, there are some deviations comparing to the experimental data. These deviations are around 25% of the relative difference and go up to around 90% when AoA is 15° . As mentioned before, these differences

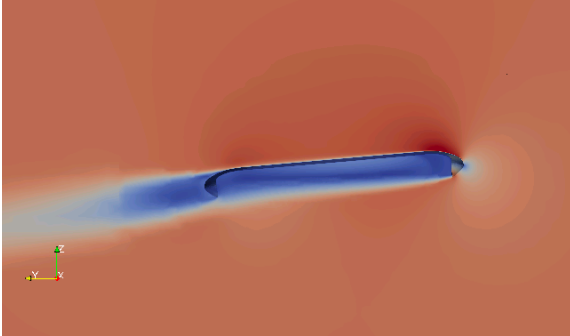
can be explained on one hand by the uncertainties in the measures and on the other hand by numerical modeling assumptions, i.e. CAD production (3D scan), the may generate some geometry imperfections.



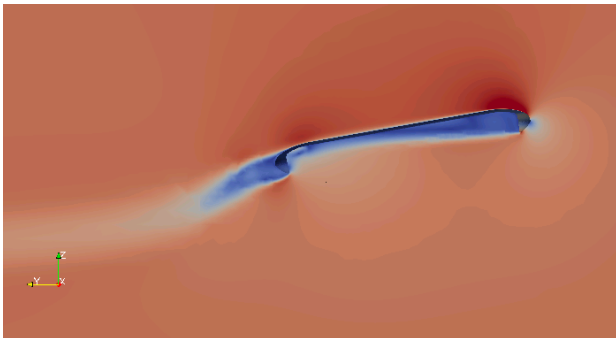
(a) AoA = 0°



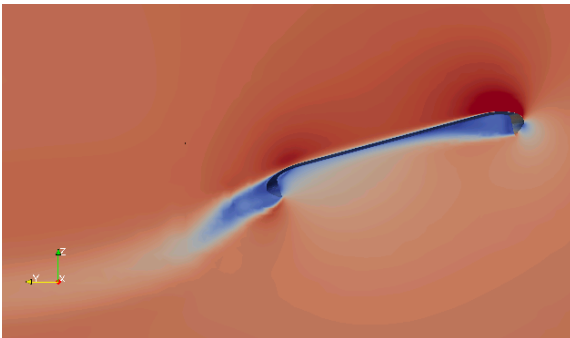
(b) AoA = -5°



(c) AoA = 5°



(d) AoA = 10°

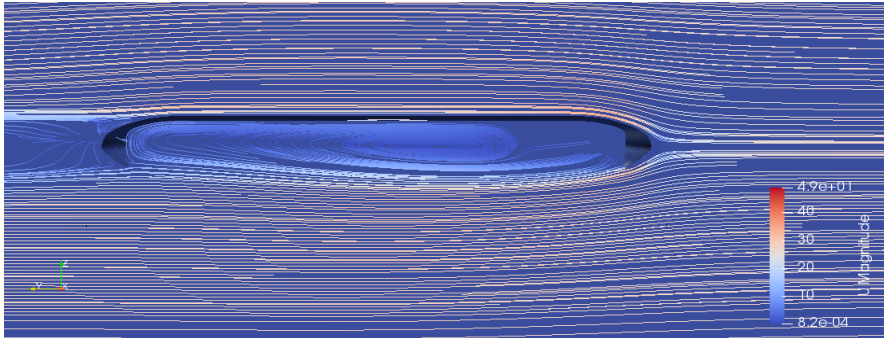


(e) AoA = 15°

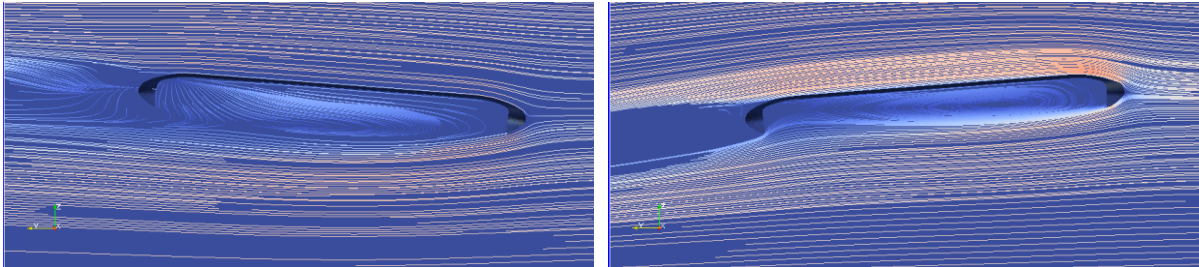
Figure 29. Velocity contour for different AoA.

Figure 29 shows the flow visualization over a non-rotating disc (Putter) for different AoA. With flow from right to left, first of all, note the upwash ahead of the leading edge, then the

boundary layer separates off the upper surface reattaching shortly thereafter creating a recirculating bubble. Further downstream the reattached boundary layer separates from the upper surface on the trailing edge, this separated shear layer contributes to the wake which has a downwash angle slightly greater than the AoA. In the cavity, the shear layer separated from the front lip is reattached to the inner side of the trailing edge, and the reverse flow occurs under the shear layer toward the front edge. The fluid flowing in the front edge of the cavity (reverse flow) is restricted by the stagnant air pockets in the leeward wind on the front edge and cannot flow further forward. This stagnant air at the leading edge is represented by a weakly moving arrow. The linear stagnation line in the paint pattern on the surface of the cavity marks the boundary between the reverse flow and stagnant air in the cavity. This boundary is shown as a dividing line in the topology map.



(a) AoA = 0°



(b) AoA = -5°

(c) AoA = 5°

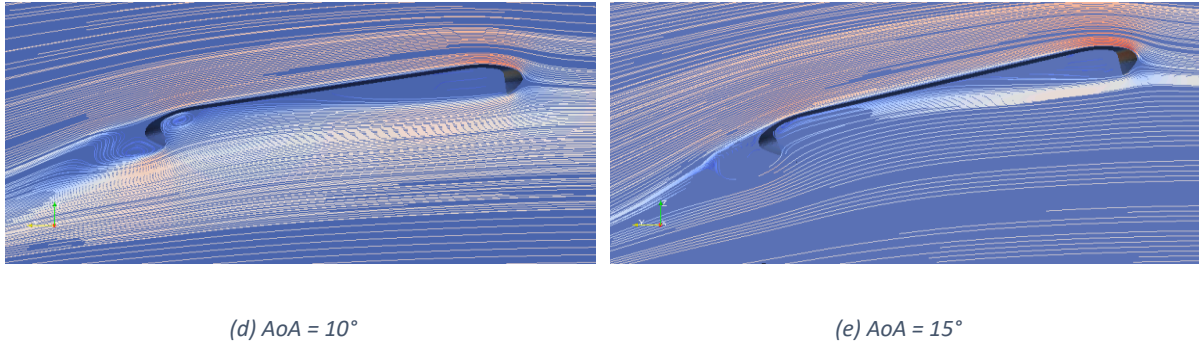


Figure 30. Velocity streamline plots for different AoA.

The two-dimensional central flow cross-sections for a range of AoA are shown in Figure 30, flow from right to left. At the angle of the attack of the 0° the separation bubble is small, the shear layer beneath the disc covers the entire cavity. The reversed flow above the cavity shear layer occurs centrally for almost the entire length of the cavity. The leading-edge rim forces the central reversed flow to split, deflected towards the wingtips. This deflection provided the rotation to generate two stagnation points on either side of the mid-span, these spiral nodes were visualized in the surface paint patterns. Separation occurs on the trailing edge; the separated shear layers influence the structure of the bluff body wake.

With increased AoA the separation bubble on the upper surface becomes enlarged, reattachment occurs further downstream. Also, the shear layer separating off the leading-edge lip attaches further upstream, and the wake downwash angle increases. At 10° AoA the separation bubble enlarges slightly (Figure 30c and Figure 30d), the shear layer beneath the disc still covers the entire cavity. The reversed flow above the cavity shear layer occurs centrally for only half the length of the cavity, as the dead air pocket grows larger.

At 15° AoA the upper surface separation bubble enlarges further (Figure 30e), as the reattachment line moves further downstream. The cavity shear layer now reattaches at the half chord position, a recirculating bubble is enclosed beneath the shear layer, downstream from the dead air pocket. Within the cavity, the reattached boundary layer remains attached throughout the inside of the trailing edge rim, separating off the lip.

The three-dimensional flow topology at 10° AoA is shown in Figure 31 and depicts the structure of the separation bubble and trailing vortices, flow from right to left.

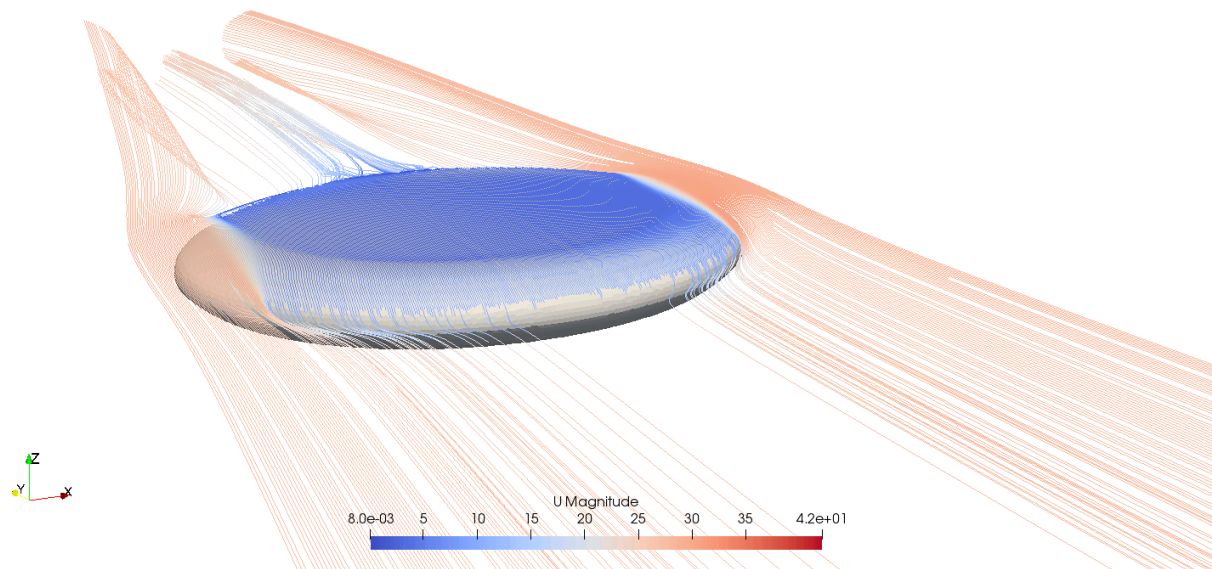


Figure 31. Streamlines – Counter-rotating vortex.

The separation bubble forms a crescent-like shape, the arced separation and reattachment lines are marked. The arrows show the direction of the separated shear layer flow. Three cross-sectional slices through the structure show the recirculation/roll-up of fluid within the bubble. The rotation of vortices is in the conventional sense for a typical wing section at positive AoA, the vortex trailing from the port wing-tip has clockwise rotation (when viewed from downstream) whereas the starboard trailing vortex rotates counterclockwise. Note the entrainment of fluid into the vortices from the upper surface boundary layer and also from within the cavity.

It is shown the downwash generated in the wake of the disc. The strong central downwash and the form of the trailing vortices become apparent with increased AoA from 0° through 10° . Unsteady bluff body wake at 0° AoA. The structure of the trailing vortices has begun to develop at 5° AoA, the turbulence generated by the bluff body still visible. Note the close vicinity of the trailing vortex pair due to the low aspect ratio, as the AoA increases the central downwash develops and stronger rotation is given to the trailing vortices. At 10° AoA, the vortex structures are more clearly defined. The comparison of these two methods of illumination enables the reader to better understand how the wake cross-sections relate to the disc-wing model.

The bluff body wake, downwash, and trailing vortex structures downstream of a non-spinning disc wing are shown in Figure 32, for an AoA of 10° .

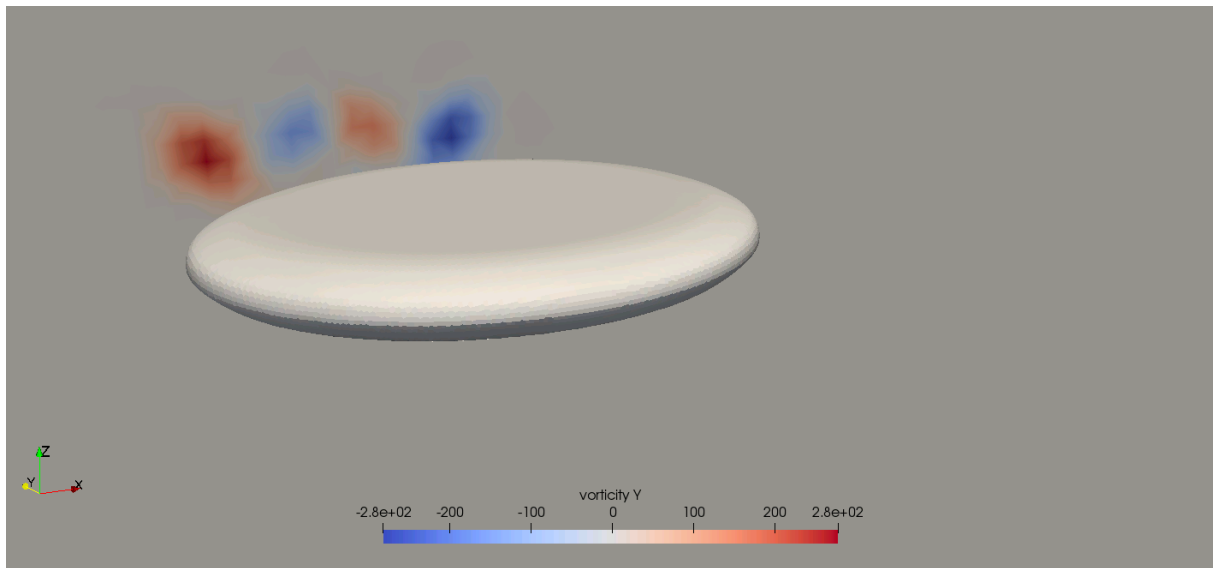


Figure 32. Vorticity - Counter-rotating vortex.

The bluff body wake, downwash, and trailing vortex structures extending downstream from a non-spinning disc wing are shown in Figure 32. Note the symmetry in the wake. The trailing vortices become more clearly defined with increased AoA. It can seem a transitional stage of trailing vortex development, the bluff body wake is still evident but the trailing vortices begin to take shape. The trailing vortex pair is established at 10° AoA. The inboard edge of the trailing vortices is clearly defined symmetrically. The strong central downwash exists between these two lines with the trailing vortices on either side. Cross-sectional slices through the wake at a range of positions downstream of a non-spinning disc-wing at 10° AoA has shown in Figure 32 illustrates turbulence at the trailing edge and the curvature on either side of the disc indicates central downwash.

5.5.2 Midrange disc:

The midrange geometry is illustrated in Figure 33.



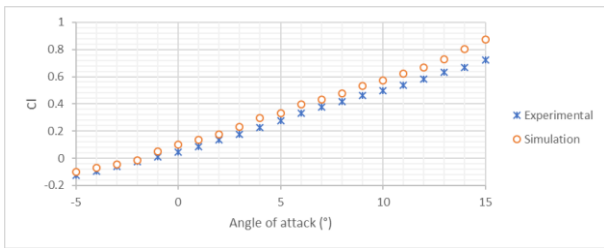
(b) Frontal view.



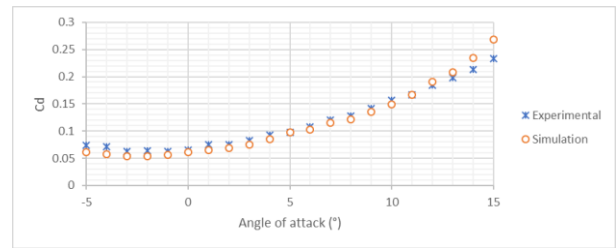
(b) Cross-section.

Figure 33. Disc geometry – Roc.

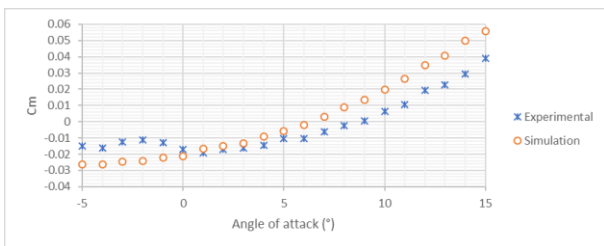
The results from the proposed numerical model using mentioned above geometry were compared to experimental work conducted by Potts (Potts et Crowther 2002) to validate the accuracy of the tool. Values of C_d , C_L and C_M were evaluated for different AoA from -5° to 15° (Figure 34).



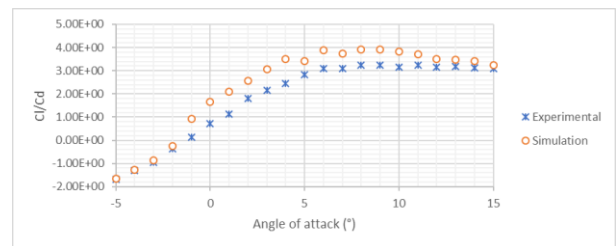
(a) C_d as a function of the AoA.



(b) C_L as a function of the AoA



(c) C_M as a function of the AoA

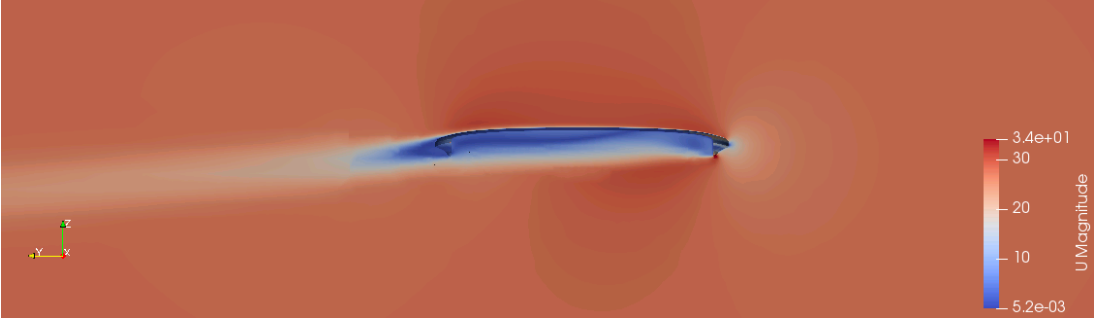


(d) C_L/C_d as a function of the AoA

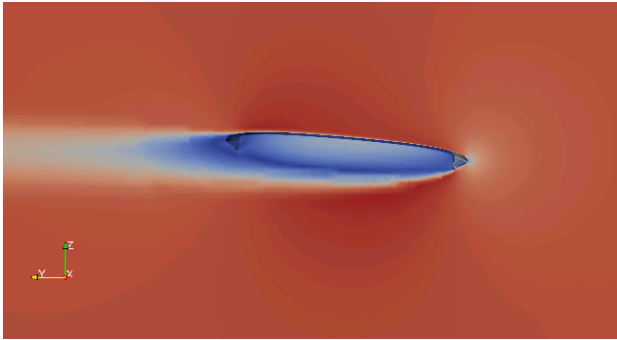
Figure 34. Experimental validation – Numerical vs Experimental values.

The results are qualitatively similar (same behavior), however, there is some deviation comparing to the experimental data. These deviations are around 25% of the relative

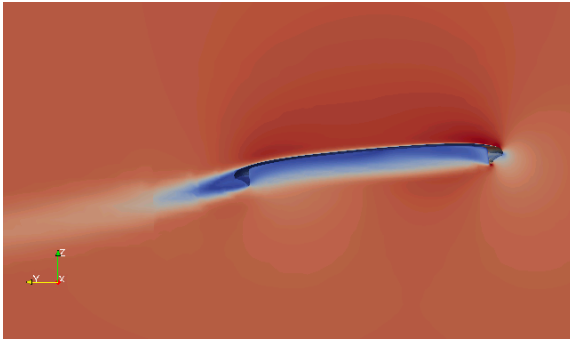
difference and go up to around 76% when AoA is 15°. As mentioned before, these differences can be explained on one hand by the uncertainties in the measures and on the other hand by numerical modeling assumptions, i.e. CAD production (3D scan), the may generate some geometry imperfections.



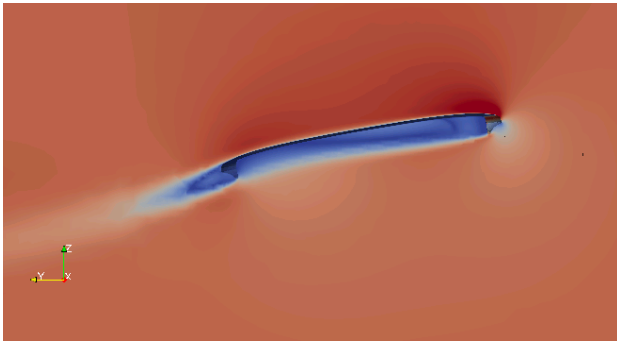
(a) AoA = 0°



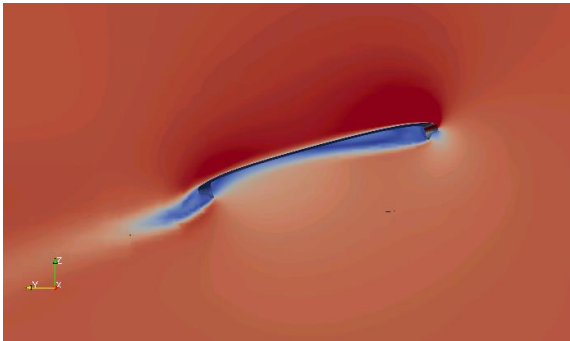
(b) AoA = -5°



(c) AoA = 5°



(d) AoA = 10°

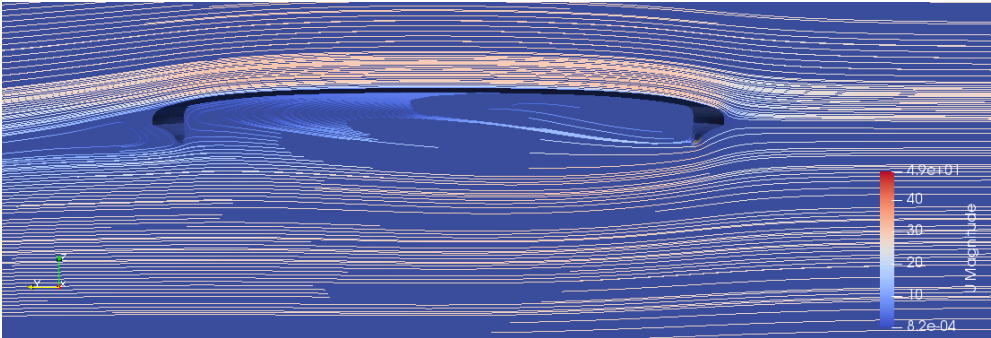


(e) AoA = 15°

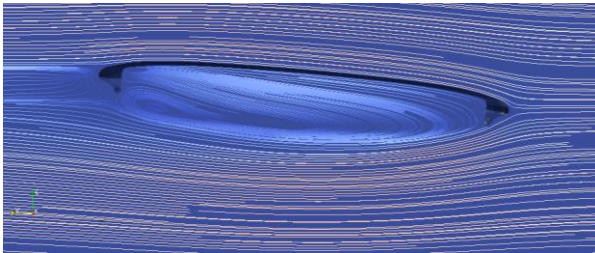
Figure 35. Velocity contour for different AoA.

Figure 35 shows the flow visualization over a non-rotating disc (Midrange) for different AoA. With flow from right to left, first of all, note the upwash ahead of the leading edge, then the

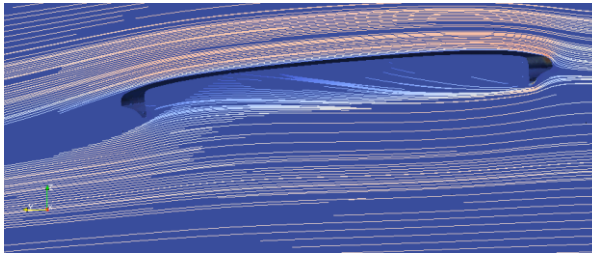
boundary layer separates off the upper surface reattaching shortly thereafter creating a recirculating bubble. Further downstream the reattached boundary layer separates from the upper surface on the trailing edge, this separated shear layer contributes to the wake which has a downwash angle slightly greater than the AoA. In the cavity, the shear layer separated from the front lip is reattached to the inner side of the trailing edge, and the reverse flow occurs under the shear layer toward the front edge. The fluid flowing in the front edge of the cavity (reverse flow) is restricted by the stagnant air pockets in the leeward wind on the front edge and cannot flow further forward. This stagnant air at the leading edge is represented by a weakly moving arrow. The linear stagnation line in the paint pattern on the surface of the cavity marks the boundary between the reverse flow and stagnant air in the cavity. This boundary is shown as a dividing line in the topology map.



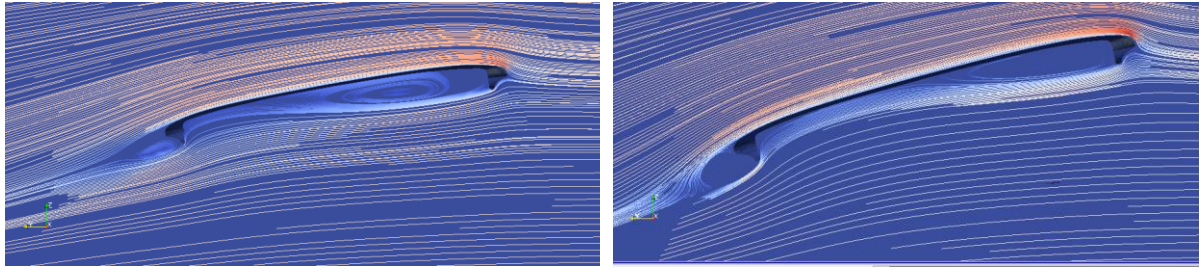
(a) AoA = 0°



(b) AoA = -5°



(c) AoA = 5°



(d) AoA = 10°

(e) AoA = 15°

Figure 36. Velocity stream-line plots for different AoA.

The two-dimensional central flow cross-sections for a range of AoA are shown in Figure 36, flow from right to left. The separation bubbles at the angle of attack of the 0° is small, the shear layer beneath the disc covers the entire cavity. The reversed flow above the cavity shear layer occurs centrally for almost the entire length of the cavity. The leading-edge rim forces the central reversed flow to split, deflected towards the wingtips. This deflection provided the rotation to generate two stagnation points on either side of the mid-span, these spiral nodes were visualized in the surface paint patterns. Separation occurs on the trailing edge; the separated shear layers influence the structure of the bluff body wake.

With increased AoA the separation bubble on the upper surface becomes enlarged, reattachment occurs further downstream. Also, the shear layer separating off the leading-edge lip attaches further upstream, and the wake downwash angle increases. At 10° AoA the separation bubble enlarges slightly (Figure 36c and Figure 36d), the shear layer beneath the disc still covers the entire cavity. The reversed flow above the cavity shear layer occurs centrally for only half the length of the cavity, as the dead air pocket grows larger.

At 15° AoA the upper surface separation bubble enlarges further (Figure 36e), as the reattachment line moves further downstream. The cavity shear layer now reattaches at the half chord position, a recirculating bubble is enclosed beneath the shear layer, downstream from the dead air pocket. Within the cavity, the reattached boundary layer remains attached throughout the inside of the trailing edge rim, separating off the lip.

The three-dimensional flow topology at 10° AoA is shown in Figure 37 and depicts the structure of the separation bubble and trailing vortices, flow from right to left.

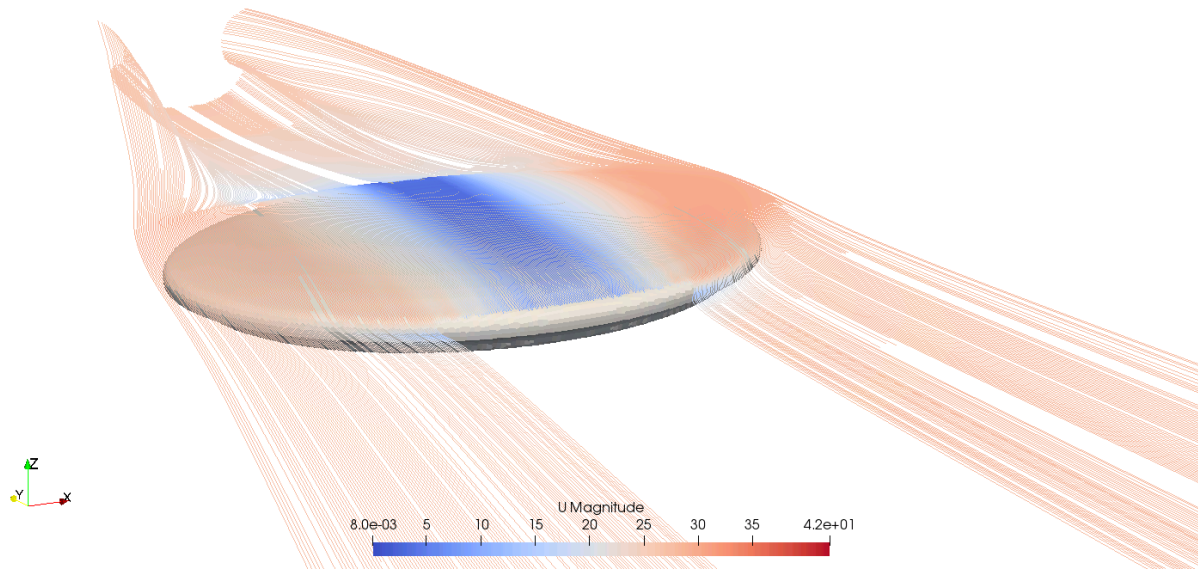


Figure 37. Streamlines – Counter-rotating vortex.

The separation bubble forms a crescent-like shape, the arced separation and reattachment lines are clearly marked. The arrows show the direction of the separated shear layer flow. Three cross-sectional slices through the structure show the recirculation/roll-up of fluid within the bubble. The rotation of the vortices is in the conventional sense for a typical wing section at positive AoA, the vortex trailing from the port wing-tip has clockwise rotation (when viewed from downstream) whereas the starboard trailing vortex rotates counterclockwise. Note the entrainment of fluid into the vortices from the upper surface boundary layer and also from within the cavity.

It is shown the downwash generated in the wake of the disc. The strong central downwash and the form of the trailing vortices become apparent with increased AoA from 0° through 10° . The wake cross-section at one chord length downstream of the disc trailing edge. Unsteady bluff body wake at 0° AoA. The structure of the trailing vortices has begun to develop at 5° AoA, the turbulence generated by the bluff body still visible. Note the close vicinity of the trailing vortex pair due to the low aspect ratio, as the AoA increases the central downwash develops and stronger rotation is given to the trailing vortices. At 10° AoA, the vortex structures are more clearly defined. The comparison of these two methods of illumination enables the reader to better understand how the wake cross-sections relate to the disc-wing model.

The bluff body wake, downwash, and trailing vortex structures downstream of a non-spinning

disc wing are shown in Figure 38, for an AoA of 10° .

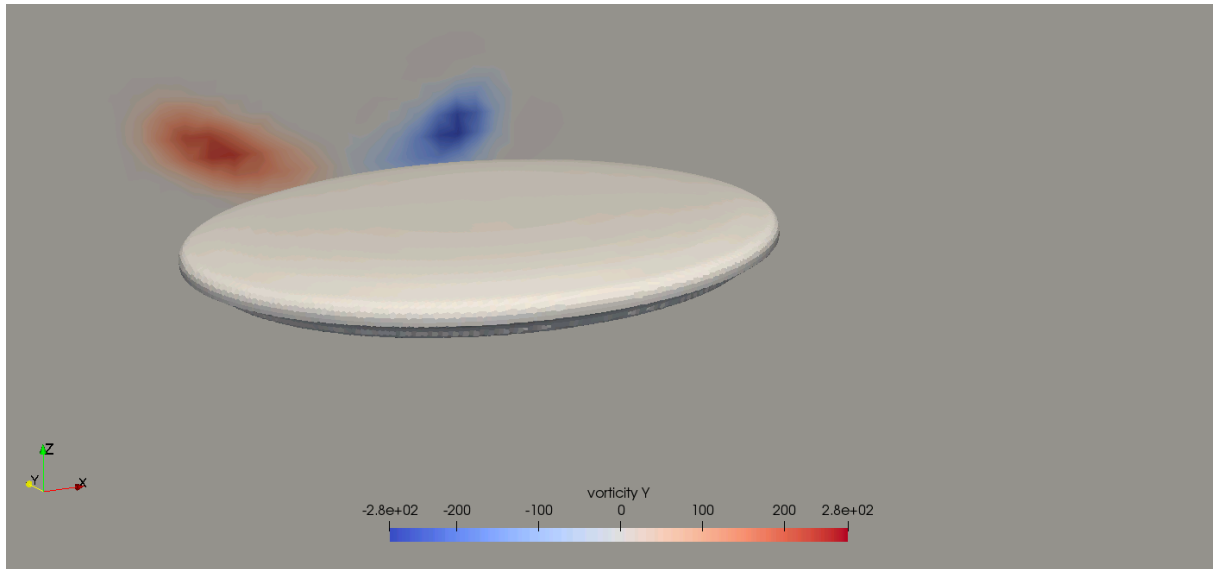


Figure 38. Vorticity - Counter-rotating vortex.

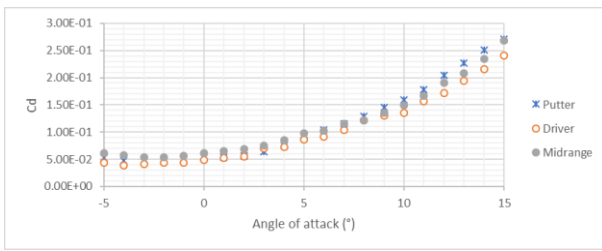
The bluff body wake, downwash, and trailing vortex structures extending downstream from a non-spinning disc wing are shown in Figure 38. Note the symmetry in the wake. The trailing vortices become more clearly defined with increased AoA. It can seem a transitional stage of trailing vortex development, the bluff body wake is still evident but the trailing vortices begin to take shape. The trailing vortex pair is established at 10° AoA. The inboard edge of the trailing vortices is clearly defined symmetrically. The strong central downwash exists between these two lines with the trailing vortices on either side. Cross-sectional slices through the wake at a range of positions downstream of a non-spinning disc-wing at 10° AoA has shown in Figure 38 illustrates turbulence at the trailing edge and the curvature on either side of the disc indicates central downwash.

5.5.3 Comparison of putter, midrange and driver discs:

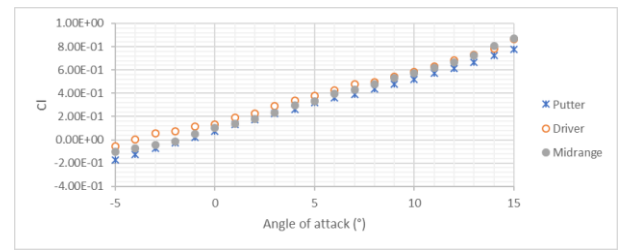
Three commercially available golf discs were evaluated. These discs were simulated to verify the effectiveness of the CFD methods and tuning for actual commercially available golf discs. The simulations for the three designs were evaluated using the same CFD method and set turbulence model.

The geometry of a disc impacting the drag and lift forces along with the aerodynamic moments may determine its unique flight characteristics. These characteristics, on the other hand, play a secondary role in the moment of inertia associated mostly with its mass. However, these

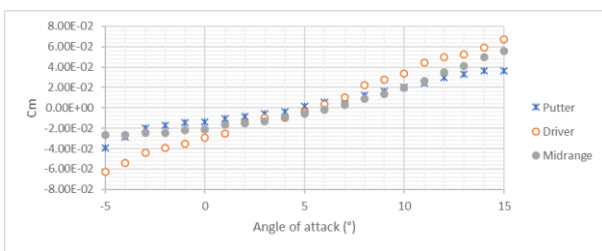
combined effects could cause the deviation in the overall aerodynamic performance of the disc which consequently will have an impact on the flight performance as well (Figure 39).



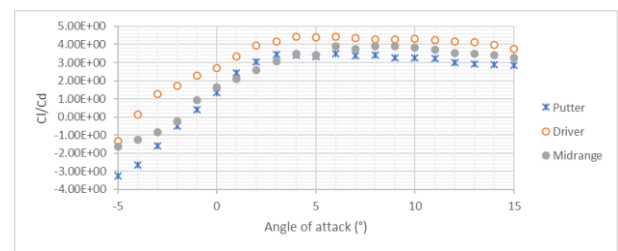
(a) C_d as a function of the AoA.



(b) C_L as a function of the AoA



(c) C_M as a function of the AoA



(d) C_L/C_d as a function of the AoA

Figure 39. Experimental validation – Numerical vs Experimental values.

The geometrical features have a very direct impact on the overall aerodynamic performance as mentioned before (Figure 39a). This has happened due to the interaction of flow with the area available at the front to a bigger level. As the aerodynamic lift value does not have a significant change by geometry configuration, then the parameters which are dependent on the aerodynamic lift will remain the same in all the discs such as the induced drag. Putter discs having the larger thickness-to-diameter ratio and other geometric parameters, may have an area with a higher value than the other discs and thus a greater drag coefficient but it may reduce the ability of the putter disc to roll along the path of the flight. The value of the drag may also be affected by its specific geometrical parameters such as the rim edge curvature of the disc.

Results show a typical shape of linear lift coefficient evolution for all geometries, consistent with previous studies (Figure 39b). Lift coefficient curves are similar for all attack angles (mostly positive angles). However, the putter disc shows lower lift coefficient values all the long. Driver disc presents a slight increment at lower angles of attack.

The angle of attack will also have its effect on the pitching moment as they have a direct

relation between them which is also linked with the center of the aerodynamics relevant to the center of gravity (Etkin and Reid, 1996) (Figure 39c). Positive pitching moments signify that the discs do not have a stable behavior in pitch (attack angles $> 5^\circ$). As supposed by adding a geometric feature could vary the general characteristics of the discs such as the pitching moments value may decrease due to the addition of the cavity as a geometric feature.

The C_L/C_d is the plot which helps very much to understand the aerodynamics of an aircraft such as to help find the performance and the efficiency such as the greater value of the lift to drag coefficient ratio (C_L/C_d) usually indicates better performance (Figure 39d). The value of C_L/C_d is dependent on various factors but here it is varying with the value of the angle of attaching until it reaches its maximum or plateau and becomes constant onwards. The maximum C_L/C_d for all the discs is found around 5° . Evaluating disc performance using the C_L/C_d curves clearly satisfy the superiority of the driver disc. But due to the uncertainty in the nature of the free-flying discs, their aerodynamic performance is not dependent on decreasing or minimizing the value of drag and increasing or maximizing the value of the lift. It can also, be observed from the results that the pitching moment is also, one of the integral parameters which could influence the aerodynamic performance of the discs significantly. It can also be converted into the disc spins translated from the rolling rates. Also, the minimum the value of C_M the better the performance of the discs as it helps to minimize the rolling motion of the discs.

The outcomes of the aerodynamic analysis of multiple discs show relatively consistent behavior which is expected from these based upon their standard performance during flight tests. Such as the putter disc always shows a higher value of the aerodynamic drag coefficient than the driver disc while testing them on the general flight angles.

In addition to that, it has also, been observed from the computational fluid dynamics analysis of the flying discs that the geometry of the disc is very important while studying its flight behavior such as by introducing the cavity feature affects its aerodynamic characteristics and performance greatly. The aerodynamic performance of a simple frisbee disc is quite similar to that of the putter disc: their analysis shows a relatively straight path with a bit shorter range than the long-range models, such as the discs (driver discs) introduced to cover the long-range distances. The discs having longer range configurations shows the distinctive geometrical features which enable them to cover higher distance and generate less drag such as the aerodynamic shape, its relatively smaller area at the front side due to the application of the

smaller ratio of thickness-to-diameter. The increased tendency of the discs came with an expense of its deviation from its intended flight path which means that a player throwing a driver disc should have the higher throwing skills to achieve the same accuracy of a path as achieved in the putter discs. Finally, the disc designs having the mid-range also show the intermediate performance between the driver and putter discs.

5.5.4 RANS/DDES comparison:

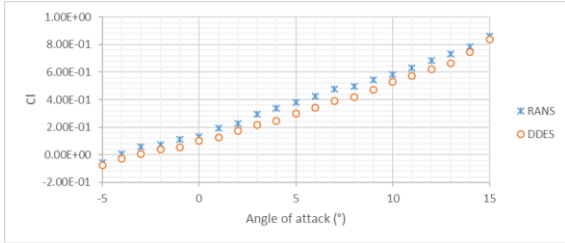
The highly turbulent flows such as the Large-eddy simulations (LES) show quite good behavior in reference to their estimated measurements from the thesis but it may not be adapted since high ratio cells near the geometry ($+y$). Unfortunately, LES may imply higher cost due to its complex computational studies especially in the cases of the flows from moderate to the very high values of the Reynolds numbers which are employed mostly during the aerodynamic studies. In Reynolds Average Navier-Stokes (RANS) simulation all the turbulence is modeled making it possible to use coarser spatial resolutions than for LES, and thus demanding lower computational effort.

Additionally, this kind of simulation is highly time-dependent and unsteady and may cause difficulties to estimate the values and observe the structure of the flows accurately while employing the RANS method. While using the RANS method the prediction of aerodynamic characteristics (prediction of drag, lift & moment) is possible but these estimations rely very much on the relevant case which makes it untrustworthy to evaluate the aerodynamic performance and the development of the aerodynamic model.

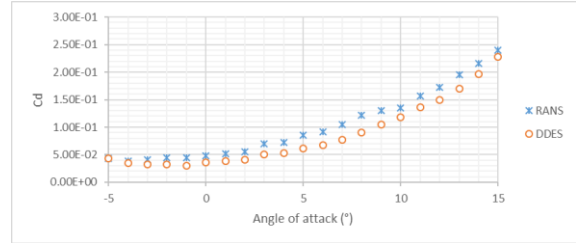
To resolve the issue of the cost related to the large-eddy simulations (LES) method and the lower value of the accuracy of the RANS model a model has been proposed which has good features from both models. The introduced model is called the hybrid RANS-LES model which negates the negative features of both the combining models. The method which is used normally is the Detached Eddy Simulations (DES) model where both the models are used in a hybrid form such as the LES model is used elsewhere other than the near-wall boundary and the RANS model is used only to capture the near-wall flows. It also benefits to achieve the coarser spatial resolution Compared to the LES and RANS method which also, helps to successfully solve the Turbulence. This method also supports achieving better mesh quality by achieving the lower mesh sizes and temporal solutions which are required compared to the LES method.

Therefore, to better understand the limitations of the steady-state solution of an inherently

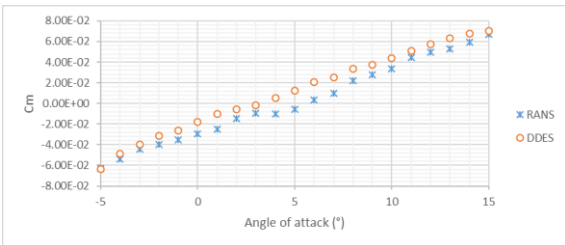
unsteady phenomenon, transient Delayed Detached Eddy Simulations (DES) using kOmegaSSTDES is also performed and the results are compared to the steady-state RANS and experimental data for the three geometries (Figure 40):



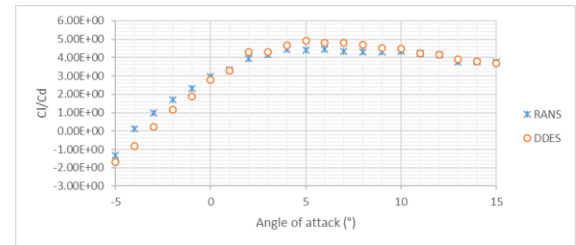
(a) C_d as a function of the AoA.



(b) C_L as a function of the AoA

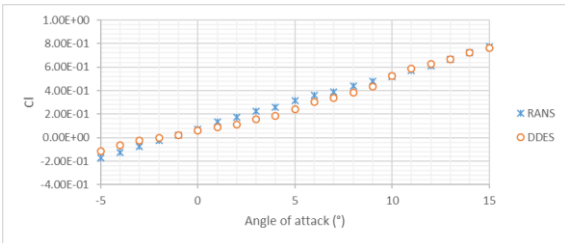


(c) C_M as a function of the AoA

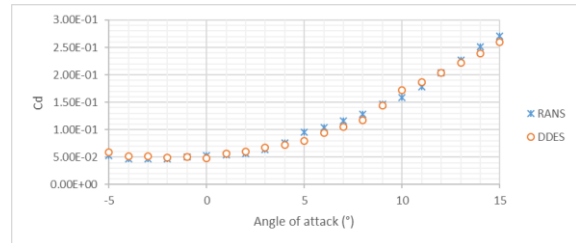


(d) C_L/C_d as a function of the AoA

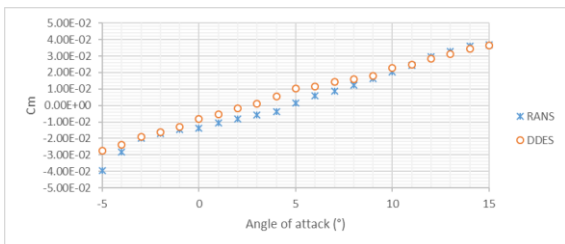
RANS/DDES comparison – Wraith disc.



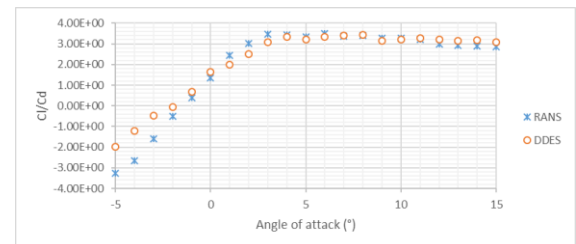
(e) C_d as a function of the AoA.



(f) C_L as a function of the AoA

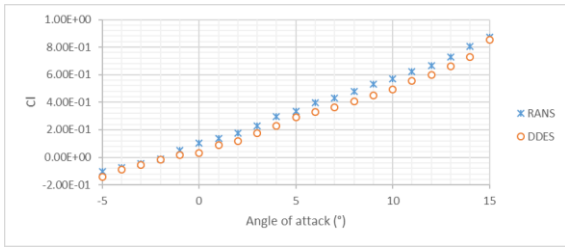


(g) C_M as a function of the AoA

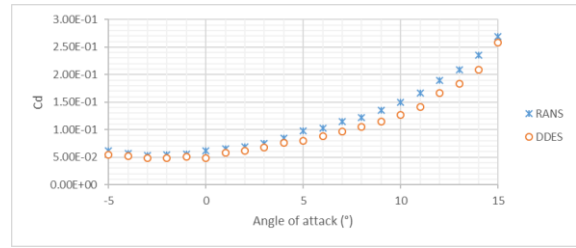


(h) C_L/C_d as a function of the AoA

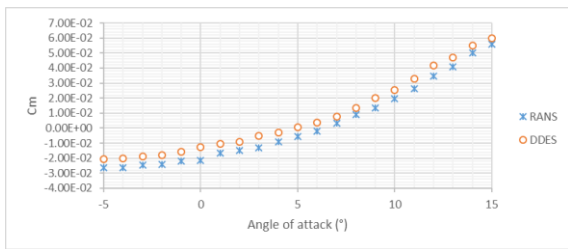
RANS/DDES comparison – Aviar disc.



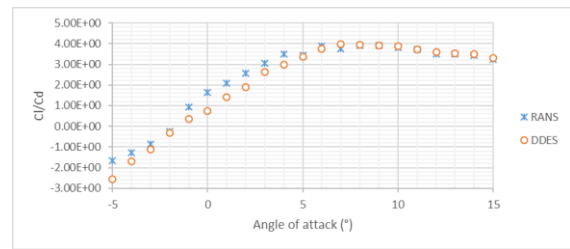
(i) C_d as a function of the AoA.



(j) C_L as a function of the AoA



(k) C_M as a function of the AoA

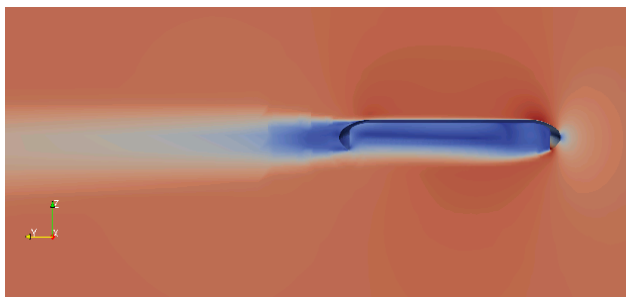


(l) C_L/C_d as a function of the AoA

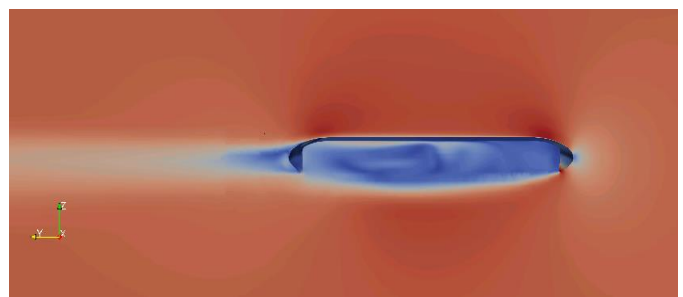
RANS/DDES comparison – Roc disc.

Figure 40: RANS/DDES comparison – Different geometry discs.

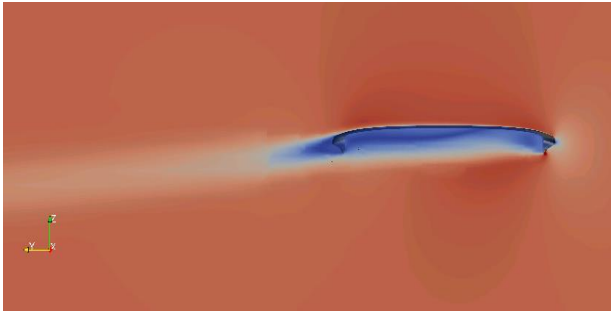
Similar values are found for both RANS and DDES models of turbulence. The results are qualitatively similar, however, there is some deviation comparing to the experimental data. These deviations are not greater than 84% for a RANS model (C_d Roc midrange) and 63% for a DDES model (C_M Aviar putter). However, in the other cases, this difference is around 30% showing a good agreement between both turbulence models and the experimental data. As mentioned before, the RANS model is based on statistical averaging which leads to the steady equation while DDES, combined LES and RANS approach, is based on local filtering, generating an unsteady flow as shown in (Figure 41).



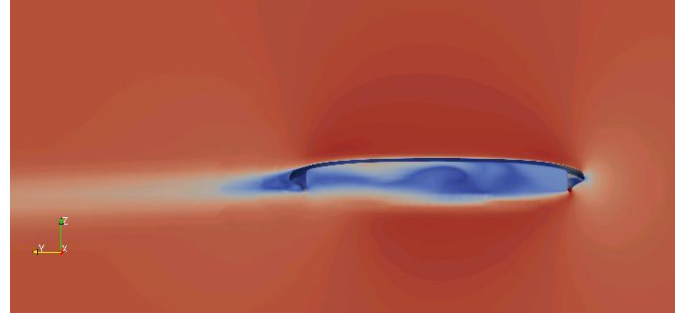
(a) Aviar RANS.



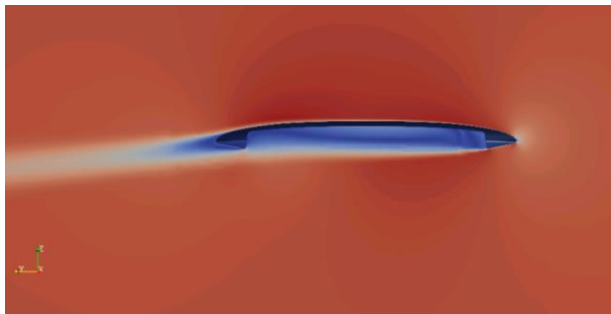
(b) Aviar (DDES).



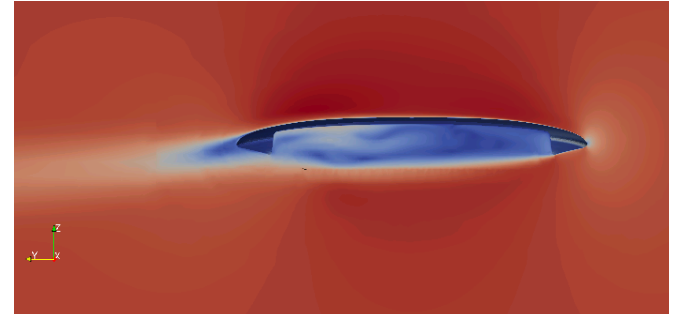
(c) Midrange (RANS).



(d) Midrange (DDES).



(f) Wraith (RANS).



(g) Wraith (DDES).

Figure 41: Velocity contour - RANS and DDES comparison – $AoA = 0^\circ$.

From the plots (Figure 41), it seems the recirculation region is larger for the DDES simulations, but still, the drag becomes lower. As it seems, DDES is better at capturing a small length scale than RANS as explained before (Figure 41). Indeed, Also, the RANS regions are strongly shielded by using the DDES model which makes the RANS regions less sensitive towards the grid-induced separation (GIS). The DES provides various improvements such as it could provide strong shielding during the refinement of mesh to the RANS region and also, provides surety for the fast transition of the RANS to LES regions. The most important thing in it is to reduce the user dependency and the possibilities to GIS, because there is not much awareness is needed for the mesh switching effects of the RANS to LES. But the initial lack of the resolved results could be improved if the transition speed between both the models (RANS & LES) could be improved.

It has been observed that the RANS model is not able to cater to the issues related to unsteady flows. Even it shows the deviated results with the high turbulence models that is why the RANS model shows the wrong results about the unsteady behavior of the flows including the vortex shedding etc. While the LES model works well for unsteady flows as it uses the Navier Stokes

governing equations to compute the flow field. It uses the spatial filtering technique with the help of the Navier Stokes equation instead of using the time-averaged functions to resolve the stresses related to the turbulent flows.

6. Conclusion

The current thesis performed an analysis on flying disc aerodynamics using Computational Fluids Dynamics (CFD). This research study also illustrates that the computational fluid dynamics technique could be employed to examine the variations in lift and drag coefficients along with other aerodynamic parameters as well. The results were compared to experimental work conducted by Pott (Potts et Crowther 2002) for the validation of the model. From this comparison, simulations were close to experimental data showing the capacity of the numerical tool to perform aerodynamics modeling of flying discs with good accuracy. Flow topology tendencies were the same found in experimental work and based on the presented results. This comparison has shown that both models present similar estimations. However, LES, based on local filtering, may generate a more unsteady flow than RANS. It has been a known fact that the time-averaged-based formulation of the RANS model is not capable of tackling the problems related to unsteady fluid flows. That is the reason many researchers worked to develop a model to resolve the problems related to unsteady flows. This diverted the researcher's attention towards the direct numerical simulation (DNS) model and the large-eddy simulations (LES) model. These techniques have been proved to be expensive in the computational sense as the LES model requires a fine grid with the resolved conditions over the entire fluid domain. This LES model if joined with the RANS model has shown many applications if joined with other models to reduce the required computational power.

The simulations were performed for three different disc geometries as Putter, Midrange, and Aviar and compared. All cases were compared to experimental work from Pott (Potts et Crowther 2002). Simulations show similar behavior comparing to experimental data. Some deviations may appear, associated mainly with defaults of the geometry (CAD files). However, these deviations remain low since values from the simulation have the same order of magnitude as experimental ones. All the flow topologies from the geometries show similar behavior as expected.

The aerodynamic characteristics were also, examined during the computational study of the flying discs. The simulation results obtained from the computational fluid dynamics (CFD)

analysis and the selected experimental results by Potts et Crowther demonstrated the flight behavior of the flying discs along with the fluid behavior at the surrounding of the disc during the flight. These results revealed the key characteristics which contribute to the performance of the disc during the flight. These parameters include the pitching moment coefficients and the lift to drag ratio coefficients. It is suggested that the lift to drag ratio should be maximized depending upon the range & launch speed and the coefficient of pitching moment should be minimized to lower the effects of the rolling. In addition to that trim point also, plays its role in the stability of the flying discs.

Also, a comparison between RANS and DDES turbulence models is proved to be very useful. As, the results are qualitatively similar, however, there are some deviations comparing to the experimental data. As for the RANS/LES comparison, DDES, combined LES and RANS approach, based on local filtering, generating an unsteady flow in comparison to RANS approach. The RANS model shows very much deviation from the expected results in case of the separated unsteady flows. While on the other hand the detached eddy simulations model has shown good results in the unsteady separated flow cases even with the same grid generation as that of the RANS model. Standard RAS kOmegaSST model provides outcomes that are closely similar to the experimental results and provides a very good illustration of the flow structures over the surface of the discs, however, for better representation of the turbulence a DDES kOmegaSSTDDES model may be combined.

This validated model could provide a platform for future researchers to understand the aerodynamics of the discs. Furthermore, it could support them to not only examine the current results closely but also, to further work focusing on the broader range of AoA, variations due to the geometrical amendments, and the effect of the spinning of the discs. Increase the variation range to greater of AoA to investigate its influence on disc aerodynamic performances and flow patterns comparing to low AoA. Additionally, simulations for the higher Reynolds numbers should be performed. Investigation into other transitional models can also help create a better plot that covers the full range of the flow regime.

7. References

- [1.] "Aerodynamic effects on discus flight: American Journal of Physics: Vol 49, No 12". s. d. Accessed May 11, 2021.
- [2.] Aerodynamic characteristics of several airfoils of low aspect ratio in Search Works

- catalog". s. d. Accessed May 7, 2021..
- [3.] Anderson, John David. 2017. Fundamentals of Aerodynamics. Sixth edition. McGraw-Hill Series in Aeronautical and Aerospace Engineering. New York, NY: McGraw-Hill Education.
- [4.] "Anderson-Fundamentals_of_Aerodynamics.pdf". s. d. Accessed May 14, 2021.
- [5.] Breuer M, Rodi W. Large-eddy simulation of complex turbulent flows of practical interest. In Flow Simulation with High-Performance Computers II, vol. 52. Hirschel EH (ed.), Notes on Numerical Fluid Mechanics, Viewer: Braunschweig, 1996; 258–274.
- [6.] Breuer M. Large-eddy simulation of the sub-critical flow past a circular cylinder: numerical and modeling aspects. International Journal for Numerical Methods in Fluids 1998; 28:1281–1302.
- [7.] Bartoniez, K (2000) Javelin Throwing: An Approach to Performance Development, : Sport: Performance Enhancement and Injury Prevention, pp. 401-434.
- [8.] Bauer, Steven X. S., et Steven X. S. Bauer (1998) An Aerodynamic Assessment of Micro-Drag Generators (MDGs), : 16 th AIAA Applied Aerodynamic Conference.
- [9.] Bousman, William G. (2003) Aerodynamic Characteristics of SC1095 and SC1094 R8 Airfoils, : VA: Defense Technical Information Center.
- [10.] Bartlett, R. M (2000) Principles of throwing, Sport: Performance Enhancement and Injury Prevention pp. 365-380.
- [11.] Cobleigh, Brent R. (1998) Development of the X-33 Aerodynamic Uncertainty Model.
- [12.] Crowther, William, et Jonny Potts (2007) Simulation of a spinstabilised sports disc, : Sports Engineering 10 (janvier): 3-21.
- [13.] Dinu, D. (2021). (rep.). Does using a lighter disc in training affect your technique? INS. <https://notyss.com/savoirsport/fiche.jsp?idFiche=533>. s. d. Accessed May29.
- [14.] De Mestre, N.J., Hubbard, M. and Scott, J. (1998) Optimizing the shot put,: Fourth Conference on Mathematics and Computers in Sport, pp. 249-257.
- [15.] Fail, R., J. A. Lawford, R. C. W. Eyre, R. J. A. Lawford, et R. C. W. Eyre (1957) Low-Speed Experiments on the Wake of Flat Plates normal to an Air Characteristics Stream.
- [16.] "Frisbee Aerodynamic - Boat Design Net". s. d. Accessed May 15, 2021.

- [17.] “Frisbee Aerodynamics - Research Paper | AOE 4064 - Docsity”.
<https://www.docsity.com/en/frisbee-aerodynamics-research-paper-aoe-4064/6781231/>. s. d. Accessed May 27, 2021.
- [18.] Grasmeyer, Joel M., Matthew T. Keennon, et Aerovironment Inc. (2001) Development of the Black Widow Micro Air Vehicle, : 39th AIAA Aerospace Sciences Meeting and Exhibit.
- [19.] Hall, Jeremiah, and Kamran Mohseni (2015) Micro Aerial Vehicles, : Encyclopedia of Microfluidics and Nanofluidics.
- [20.] Hubbard, M. and Cheng, K.B. (2007) Optimal Discus Trajectories, : Journal of Biomechanics, 40, pp. 3650-3659.
- [21.] Hildebrand, F. (2001) Modelling of discus flight, San Francisco., pp. 371- 374.: XIX International Symposium on Biomechanics in Sports.
- [22.] <https://www.yumpu.com/en/document/view/42563210/frisbee-aerodynamic-boat-design-net.> /. s. d. Accessed June 05, 2021.
- [23.] <https://www.docsity.com/en/frisbee-aerodynamics-research-paper-aoe-4064/6781231/>. s. d. Accessed May 24, 2021.
- [24.] Hubbard, M., et Stefan Hummel. 2000. « Simulation of Frisbee Flight ». 2000. /paper/Simulation-of-Frisbee-Flight-Hubbard Hummel/8ffd1b6917c0a846ee78c9fee61fdfa4603b1439. s. d. Accessed June 04, 2021
- [25.] <https://sites.google.com/site/dgresources2/Home/aerodynamics/aero-resources?tmpl=%2Fsystem%2Fapp%2Ftemplates%2Fprint%2F&showPrintDialog=1>.
- [26.] Hubbard, M., (2000) The Flight of Sports Projectiles, : Sport: Performance Enhancement and Injury Prevention.
- [27.] Hubbard, M., (2002) Optimal discus release conditions including pitching moment induced roll, : World Congress of Biomechanics.
- [28.] Hubbard, M., (1989) The Throwing Events in Track and Field, : Biomechanics of Sport, pp. 213-38.
- [29.] Hubbard, M., 1984.Optimal Javelin Trajectories. Journal of Biomechanics, 17 (10), pp. 777-787.
- [30.] Hubbard, M. and Always, L.W. (1989) Rapid and accurate estimation of release conditions in the javelin throw, Journal of Biomechanics.
- [31.] Kamaruddin N., Potts J., Crowther W. (2018) Aerodynamic performance of

flying discs, Aircraft Engineering and Aerospace Technology

- [32.] Lukes, R.A., Hart, J.H., J. Potts, Haake, S.J. (2014) A CFD analysis of flow around a disc, Centre for Sports Engineering Research, Sheffield Hallam University, Sheffield, S1 1WB, UK: The 2014 conference of the International Sports Engineering Association.
- [33.] <https://www.nasa.gov/centers/langley/news/factsheets/windtunnels.html.s>.
d. Accessed May 17, 2021
- [34.] John David (2017) Aerodynamic effects on discus flight, : American Journal of Physics: Vol 49, No 12.
- [35.] Mitchell, Timothy Lewis. s. d. "The Aerodynamic Response of Airborne Discs".
<https://doi.org/10.25669/I2K6-KKMI>. s. d. Accessed May 17, 2021
- [36.]
- [37.] Nakamura, Y., et N. Fukamachi. 1991. « Visualization of the flow past a frisbee ». Fluid Dynamics Research 7 (janvier): 31-35.
- [38.] Brian Dunbar "NASA - Wind Tunnels at NASA Langley Research Center". s. d.
Accessed 07, 2021.
- [39.] Nagami, Tomoyuki & Higuchi, Takatoshi & Kanosue, Kazuyuki. (2013). How baseball spin influences the performance of a pitcher. The Journal of Physical Fitness and Sports Medicine. 2. 63-68. 10.7600/jpfsm.2.63.
- [40.] Olsson, Vernon D. Barger; M. 1973. Classical Mechanics: A Modern Perspective.
N Second printing edition. McGraw Hill Higher Education.
- [41.] "(PDF) John D. Anderson Jr. Fundamentals of Aerodynamics McGraw Hill Science Engineering Math | shyam lad - Academia.edu". s. d. Accessed May 7, 2021.
https://www.academia.edu/28609195/John_D_Anderson_Jr_Fundamentals_of_Aerodynamics_McGraw_Hill_Science_Engineering_Math. s. d. Accessed May 23, 2021
- [42.] Potts, Jonathan, et William Crowther. 2001. « Flight Control of a Spin Stabilised Axi-Symmetric Disc-Wing ». In 39th Aerospace Sciences Meeting and Exhibit. Reno,NV,U.S.A.: American Institute of Aeronautics and Astronautics.
<https://doi.org/10.2514/6.2001-253>. s. d. Accessed May 21, 2021.
- [43.] Potts, Jonathan R, et William J Crowther. s. d. « DISC-WING AERODYNAMICS », 2.
- [44.] Potts, Jonny, et William Crowther. 2002. « Frisbee(TM) Aerodynamics ». In .
<https://doi.org/10.2514/6.2002-3150>. s. d. Accessed May 18, 2021

- [45.] Saltzman, Edwin J, K Charles Wang, et Kenneth W Iliff. 2002. « Aerodynamic Assessment of Flight-Determined Subsonic Lift and Drag Characteristics of Seven Lifting-Body and Wing-Body Reentry Vehicle Configurations », 159.
- [46.] Schuurmans, Mace. s. d. "Flight of the Frisbee". New Scientist. <https://www.newscientist.com/article/mg12717274-800-flight-of-the-frisbee/>. Sedaghat, Dr Ahmad. s. d. « FACULTY CURRICULUM VITAE ». Renewable Energy, 21. s. d. Accessed June 02, 2021.
- [47.] Society of Automotive Engineers. (1996). (rep.). Closed-test-section wind tunnel blockage corrections for road vehicles. Warrendale, PA : Society of Automotive Engineers. <https://www.worldcat.org/title/closed-test-section-wind-tunnel-blockage-corrections-for-road-vehicles/oclc/34673674>. s. d. Accessed May 16, 2021
- [48.] Seo, Kazuya, Koji Shimoyama, Ken Ohta, Yuji Ohgi, et Yuji Kimura. 2012. « Aerodynamic Behavior of a Discus ». Procedia Engineering, ENGINEERING OF SPORT CONFERENCE 2012, 34 (janvier): 92-97.
- [49.] Setoguchi, Nao, and Masahiro Kanazaki. s. d. "Low-Speed and High Angle of Attack Aerodynamic Characteristics of Supersonic Business Jet with Forward Swept Wing". In AIAA Scitech 2020 Forum. American Institute of Aeronautics and Astronautics. Accessed May 7, 2021. <https://doi.org/10.2514/6.2020-0534>. s. d. Accessed May 26, 2021
- [50.] Shur M, Spalart PR, Strelets M, Travin A. Detached-eddy simulation of an airfoil at high angle of attack, Fourth International Symposium on Engineering Turbulence Modelling and Measurements, Corsica, France, 24– 26 May 1999. Engineering Turbulence Modelling and Experiments, vol. 4, Rodi W, Laurence D (eds). Elsevier: Amsterdam, 1999; 669–678.
- [51.] Smagorinsky J. General circulation experiments with the primitive equations, I, the basic experiment. Monthly Weather Review 1963; 91:99–165.
- [52.] Spalart PR, Jou W-H, Strelets M, Allmaras SR. Comments on the feasibility of LES for wings, and on a hybrid RANS=LES approach, First AFOSR International Conference on DNS=LES, Ruston, LA, 4–8 August 1997. In Advances in DNS=LES, Liu C, Liu Z (eds). Greyden Press: Columbus, OH, 1997.
- [53.] Spalart PR. Trends in turbulence treatments. AIAA Paper 2000-2306, FLUIDS 2000, Computational Fluid Dynamics Symposium: Denver, Colorado, USA, 19–22 June

2000.

- [54.] Spalart, P. R., Jou, W. H., Strelets, M. K., and Allmaras, S. R. (Aug 1997). Comments on the feasibility of LES for wings, and on a hybrid RANS/LES approach. In Proceedings of first AFOSR international conference on DNS/LES, pages 4–8, Ruston, Louisiana. Greyden Press.
- [55.] Spalart, P. R., Deck, S., Shur, M. L., Squires, K. D., Strelets, M. K., and Travin, A. K. (2006). A new version of detached-eddy simulation, resistant to ambiguous grid densities. *Theoretical and Computational Fluid Dynamics*, 20:181–195.
- [56.] Soong, T.-C. 1976. « The Dynamics of Discus Throw ». *Journal of Applied Mechanics* 43 (4): 531-36.
- [57.] Soodak, H., 2004. Geometric top theory of football, discus, javelin. In: Hubbard, M., Mehta, R.D., Pallis, J.M. (Eds.) *Engineering of Sport 5: Proceedings of the 5th International Conference on the Engineering of Sport*, Davis, CA, vol. 1. September. ISEA, Sheffield, UK. , pp. 365-371.
- [58.] Stilley, G D. s. d. « Aerodynamic Analysis of the Self-Suspended Flare », 220, 1971.
- [59.] “Technical Literature Digest | ARS Journal”.
<https://arc.aiaa.org/doi/abs/10.2514/8.5052?journalCode=arsj>. s. d. Accessed May 09, 2021.
- [60.] “The aerodynamic response of airborne discs” by Timothy Lewis Mitchell”.
<https://digitalscholarship.unlv.edu/rtds/1043/>. s. d. Accessed May 05, 2021
- [61.] “The AVRO VZ-9 experimental aircraft - Lessons learned | Aircraft Design and Operations Meetings” s. d. Accessed June 01, 2021
- [62.] Vernon D Barger, Martin G Olsson (1973) *Classical mechanics: a modern perspective*, New York NY) by McGraw-Hill.
- [63.] Wallace, H. D. (1993). (rep.). *The Lift-Fan Powered-Lift Aircraft Concept: Lessons Learned*. Moffett Field, California, USA: NASA Contractor Report 177616.
- [64.] Zimmerman C. H. (1935) *Aerodynamic characteristics of several airfoils of low aspect ratio*, Washington, [D.C.]: National Advisory Committee for Aeronautics."